Radio Science Bulletin

ISSN 1024-4530

INTERNATIONAL
UNION OF
RADIO SCIENCE

UNION
RADIO-SCIENTIFIQUE
INTERNATIONALE

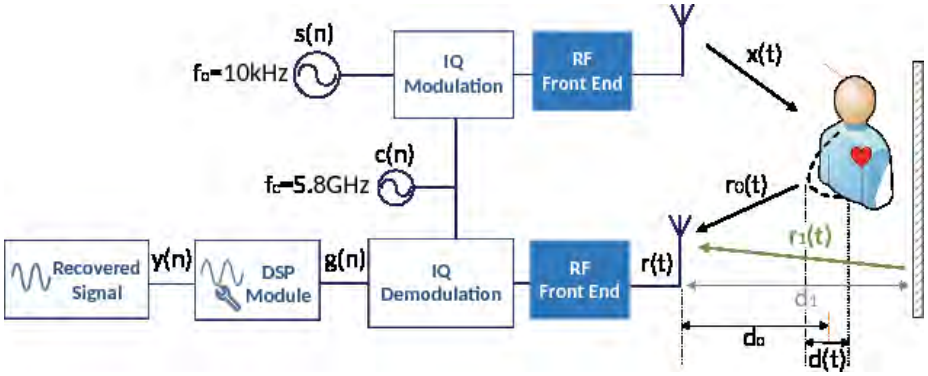

Vol. 2018, No. 364
March 2018

URSI, c/o Ghent University (INTEC)
St.-Pietersnieuwstraat 41, B-9000 Gent (Belgium)

Contents

Cover Picture: A block diagram of the Bio-Radar system. See the paper by Carolina Gouveia, Daniel Malafaia, José N. Vieira, and Pedro Pinho, pp. 30-38.

The International Union of Radio Science (URSI) is a foundation Union (1919) of the International Council of Scientific Unions as direct and immediate successor of the Commission Internationale de Télégraphie Sans Fil which dates from 1914.

Radio Science Bulletin Staff

Editor

W. R. Stone
Stoneware Limited
840 Armada Terrace
San Diego, CA 92106, USA
Tel: +1-619 222 1915, Fax: +1-619 222 1606
E-mail: r.stone@ieee.org

Editor-in-Chief

P. Van Daele
URSI Secretariat
Ghent University - INTEC
Technologiepark - Zwijnaarde 15
B-9052 Gent
BELGIUM
Tel: +32 9-264 33 20, Fax: +32 9-264 42 88
E-mail: Pet.VanDaele@UGent.be

Production Editor

I. Lievens
URSI Secretariat / Ghent University - INTEC
Technologiepark - Zwijnaarde 15
B-9052 Gent, BELGIUM
Tel: +32 9-264.33.20, Fax: +32 9-264.42.88
E-mail: ingeursi@ugent.be, info@ursi.org

Senior Associate Editors

A. Pellinen-Wannberg
Department of Physics
Umea University
BOX 812
SE-90187 Umea, SWEDEN
Tel: +46 90 786 74 92, Fax: +46 90 786 66 76
E-mail: asta.pellinen-wannberg@umu.se

O. Santolik
Institute of Atmospheric Physics
Academy of Sciences of the Czech Republic
Bocni II
1401, 141 31 Prague 4, CZECH REPUBLIC
Tel: +420 267 103 083, Fax +420 272 762 528
E-mail os@ufa.cas.cz, santolik@gmail.com

Associate Editors, Commissions

Commission A

Nuno Borges Carvalho
Instituto de Telecomunicaçoes
Universidade de Aveiro, Campus Universitario
3810-193 Aveiro, Portugal
Tel: +351 234377900, Fax: +351 234377901
E-mail: nbcarvalho@ua.pt

Pedro Miguel Cruz
Rua Sao Sebastiao
n34 Hab 33
4520-250 Santa Maria da Feira, Aveiro, PORTUGAL
Tel: +351 225898410
E-mail: pedro.cruz@controlar.pt

Tian Hong Loh
National Physical Laboratory
Hampton Road
Teddington TW11 0LW, United Kingdom
Tel: +44 020 8943 6508
E-mail: tian.loh@npl.co.uk

Nosherwan Shoaib
School of Electrical Engineering and Computer Science (SEECS)
National University of Sciences and Technology (NUST)
NUST Campus H-12, Islamabad, Pakistan
Tel: 051 90852561
E-mail: nosherwan.shoaib@seccs.edu.pk

Commission B

Andrea Michel
Department of Information Engineering
Università di Pisa
Pisa, Italy
E-mail: andrea.michel@iet.unipi.it

John Volakis
College of Engineering and Computing
Florida International University
10555 W. Flagler Street, EC2477
Miami, FL 33174, USA
Tel: +1 305 348 2807
E-mail: jvolakis@fiu.edu

Commission C

Yves Louet
CS 47601, SUPELEC
Avenue de Boulaie
F-35576 Cesson-Sévigné, France
Tel: +33 2 99 84 45 34, Fax: +33 2 99 84 45 99
E-mail: yves.louet@supelec.fr

Commission D

Naoki Shinohara
RISH
Kyoto University
Uji 611-0011, Japan
Tel: +81 774 38 3807 Fax: +81 774 31 8463
E-mail: shino@rish.kyoto-u.ac.jp

Commission E

Virginie Deniau
IFSTTAR
20. rue Elisée Reclus BP 70317
F-59666 Villeneuve d'Ascq Cedex, France
Tel: +33 03 20438991
E-mail: virginie.deniau@ifsttar.fr

Commission F

Haonan Chen
Earth System Research lab, Physical Sciences Division
NOAA
325 Broadway, Boulder, CO 80305, USA
Tel: +1 303 497 4616
E-mail: haonan.chen@noaa.gov

Tullio Tanzi
Télécom ParisTech - LabSoC, c/o EURECOM
Campus SophiaTech Les Templiers
450 route des Chappes 06410 Biot, FRANCE
Tel: +33 0 4 93008411, Fax: 33 0 493008200
E-mail: tullio.tanzi@telecom-paristech.fr

Commission G

Giorgiana De Franceschi
Dept. Arenonomy, Istituto Nazionale di Geofi sica e Vulcanology
Via di Vigna, Murata 605
00 143 Roma, Italy
Tel: +39 06 51860307, Fax: +39 06 51860397
E-mail: giorgiana.defranceschi@ingv.it

Commission H

Jyrki Manninen
Sodankylä Geophysical Observatory
Tähteläntie 62
FIN-99600 Sodanskylä, Finland
Tel: +358 400 151503, Fax +358 16 610248
E-mail: Jyrki.Manninen@oulo.fi

Commission J

Jacob W. Baars
Max Planck Institute for Radio Astronomy
Auf dem Hügel 69
53121 Bonn, Germany
Tel: +49 228 525303
E-mail: jacobbaars@arcor.de

Commission K

Kensuke Sasaki
Applied EM Research Institute
NICT
Koganei, Tokyo, Japan
E-mail: k_sasaki@nict.go.jp

Associate Editors, Columns

Book Reviews

G. Trichopoulos
Electrical, Computer & Energy Engineering ISTB4 555D
Arizona State University
781 E Terrace Road, Tempe, AZ, 85287 USA
Tel: +1 (614) 364-2090
E-mail: gtrichop@asu.edu

Historical Papers

J. D. Mathews
Communications and Space Sciences Lab (CSSL)
The Pennsylvania State University
323A, EE East
University Park, PA 16802-2707, USA
Tel: +1(814) 777-5875, Fax: +1 814 863 8457
E-mail: JDMathews@psu.edu

Et Cetera

T. Akgül
Dept. of Electronics and Communications Engineering
Telecommunications Division
Istanbul Technical University
80626 Maslak Istanbul, TURKEY
Tel: +90 212 285 3605, Fax: +90 212 285 3565
E-mail: tayfunakgul@itu.edu.tr.

Women in Radio Science

A. Pellinen-Wannberg
Department of Physics and Swedish Institute of Space Physics
Umeå University
S-90187 Umeå, Sweden
Tel: +46 90 786 7492
E-mail: asta.pellinen-wannberg@umu.se

Ethically Speaking

R. L. Haupt
Colorado School of Mines
Brown Building 249
1510 Illinois Street, Golden, CO 80401 USA
Tel: +1 (303) 273 3721
E-mail: rhaupt@mines.edu

A. J. Shockley
E-mail: aj4317@gmail.com

Solution Box

Ö. Ergül
Department of Electrical and Electronics Engineering
Middle East Technical University
TR-06800, Ankara, Turkey
E-mail: ozgur.ergul@eee.metu.edu.tr

Telecommunications Health & Safety

J. C. Lin
University of Illinois at Chicago
851 South Morgan Street, M/C 154
Chicago, IL 60607-7053 USA
Tel: +1 312 413 1052, Fax: +1 312 996 6465
E-mail: lin@uic.edu

Historical Column

G. Pelosi
Department of Information Engineering
University of Florence
Via di S. Marta, 3, 50139 Florence, Italy
E-mail: giuseppe.pelosi@unifi.it

Early Career Representative Column

S. J. Wijnholds
Netherlands Institute for Radio Astronomy
Oude Hoogeveensedijk 4
7991 PD Dwingeloo, The Netherlands
E-mail: wijnholds@astron.nl

Education Column

Madhu Chandra
Microwave Engineering and Electromagnetic Theory
Technische Universität Chemnitz
Reichenhainerstrasse 70
09126 Germany
E-mail: madhu.chandra@etit.tu-chemnitz.de

URSI Officers and Secretariat

Current Officers triennium 2017-2020

President

M. Ando
Senior Executive Director
National Institute of Technology
701-2, Higashi Asakawa, Hachioji,
Tokyo 193-0834, Japan
Tel:+81-42-662-3123,
Fax: +81-42-662-3131
E-mail: ando@kosen-k.go.jp,
mando@antenna.ee.titech.ac.jp

Vice President

O. Santolik
Institute of Atmospheric Physics
Electrical Eng. Dept
Academy of Sciences of the Czech Republic
Bocni II, 1401
141 31 Prague 4, CZECH REPUBLIC
Tel: +420 267 103 083
Fax: 420 272 762 528
E-mail: os@ufa.cas.cz, santolik@gmail.com

Past President

P. S. Cannon
Gisbert Kapp Building
University of Birmingham
Edgbaston , Birmingham, B15 2TT,
UNITED KINGDOM
Tel: +44 (0) 7990 564772
Fax: +44 (0)121 414 4323
E-mail: p.cannon@bham.ac.uk

Vice President

A. Sihvola
Electronic Science Department
Aalto University
School of Electrical Engineering
PO Box 13000
FI-00076 AALTO
FINLAND
Tel: +358 50 5871286
E-mail: Ari.Sihvola@aalto.fi

Secretary General

P. Van Daele
URSI Secretariat
Ghent University - INTEC
Technologiepark - Zwijnaarde 15
B-9052 Gent
BELGIUM
Tel: +32 9-264 33 20
Fax: +32 9-264 42 88
E-mail: Pet.VanDaele@UGent.be

Vice President

P. L. E. Uslenghi
Dept. of ECE (MC 154)
University of Illinois at Chicago 851
S. Morgan Street
Chicago, IL 60607-7053
USA
Tel: +1 312 996-6059
Fax: +1 312 996 8664
E-mail: uslenghi@uic.edu

Vice President

W. Baan
Astron
Asserweg 45
9411 LP Beilen
THE NETHERLANDS
Tel: +31 521-595 773/100
Fax: +31 521-595 101
E-mail: baan@astron.nl

URSI Secretariat

Secretary General

P. Van Daele
URSI Secretariat
Ghent University - INTEC
Technologiepark - Zwijnaarde 15
B-9052 Gent
BELGIUM
Tel: +32 9-264 33 20
Fax: +32 9-264 42 88
E-mail: Pet.VanDaele@UGent.be

Assistant Secretary General AP-RASC

K. Kobayashi
Dept. of Electr and Commun. Eng,
Chuo University
1-13-27 Kasuga, Bunkyo-ku
Tokyo, 112-8551, JAPAN
Tel: +81 3 3817 1846/69
Fax: +81 3 3817 1847
E-mail: kazuya@tamacc.chuo-u.ac.jp

Assistant Secretary General

Stefan J. Wijnholds
Netherlands Institute for
Radio Astronomy
Oude Hoogeveensedijk 4
7991 PD Dwingeloo
The Netherlands
E-mail: wijnholds@astron.nl

Executive Secretary

I. Heleu
URSI Secretariat
Ghent University - INTEC
Technologiepark - Zwijnaarde 15
B-9052 Gent
BELGIUM
Tel. +32 9-264.33.20
Fax +32 9-264.42.88
E-mail info@ursi.org

Assistant Secretary General Publications & GASS

W. R. Stone
840 Armada Terrace
San Diego, CA 92106
USA
Tel: +1-619 222 1915
Fax: +1-619 222 1606
E-mail: r.stone@ieee.org

Administrative Secretary

I. Lievens
URSI Secretariat
Ghent University - INTEC
Technologiepark - Zwijnaarde 15
B-9052 Gent
BELGIUM
Tel: +32 9-264.33.20
Fax: +32 9-264.42.88
E-mail: ingeursi@ugent.be

Editor's Comments

W. Ross Stone
Stoneware Limited
840 Armada Terrace
San Diego, CA 92106, USA
Tel: +1-619 222 1915, Fax: +1-619 222 1606
E-mail: r.stone@ieee.org

Special Section on Student Paper Award Contest From 11th Portuguese Committee of URSI Congress

Featured in this issue of the *Radio Science Bulletin* are papers from the Best Student Paper Award contest held as part of the 11th Congress of the Portuguese National Committee of URSI. The guest editors for this special section, Pedro Miguel Cruz, António Topa, and Tiago Morgado, have provided a separate introduction that explains the contest and the winners.

Network conflicts have a significant effect on the performance of LTE (Long-Term Evolution) cell-phone networks. The detection of two such conflicts, physical-cell identity (PCI) conflicts and root-sequence index (RSI) collisions, is the topic of the paper by R. Veríssimo, P. Vieira, A. Rodrigues, and M. P. Queluz. The paper reports on a test of two hypotheses regarding how well these two distinct LTE network problems could be detected through supervised techniques with near-real-time performance. Real LTE data were used. The results obtained provide useful guidance for optimizing the performance of such networks. The paper is also very valuable for the insight it provides into the way such conflicts affect LTE networks.

The purpose of the paper by Alexandra Mourato, David Duarte, Iola Pinto, and Pedro Vieira is to present energy consumption models for cellular base stations for several different technologies currently in use: GSM, UMTS, and LTE. The models were developed based on measurements from six base stations. A portion of the data was used for developing each model, and the rest was used for model validation. The average error for each model was shown to be low, and there was a high correlation between predicted and measured power for each model. Activation of a power-consumption optimization feature was studied and tested for one of the technologies. A 10% energy savings was observed without degradation in performance.

The Bio-Radar system uses a CW Doppler radar system to remotely detect and measure a person's breathing. It is used for medical sensing as well as search-and-rescue purposes. The paper by Carolina Gouveia, Daniel Malafaia, José Vieira, and Pedro Pinho describes this system, focusing on the acquisition and recovery of the respiratory information. A signal model for the system is presented, and the algorithm for extracting the breathing signal is described. The design of and experiments conducted with a prototype system using two different types of antennas are described. The experiments demonstrated that using a narrow-beam antenna produced the best results, yielding good agreement with respiratory measurements made using a band around the individual's chest.

There is a renewed interest in wireless power transfer, particularly in connection with the Internet of Things. RF-dc converters play a key role in this. The paper by Marina Jordão, Ricardo Correia, and Nuno Borges Carvalho examines the use of multi-sine signals instead of continuous-wave signals with such converters. High peak-to-average power ratio waveforms are able to enhance the RF-dc conversion efficiency. The paper begins with a review of why such waveforms have this advantage, and how such a system would work. A converter based on multi-sine signals was then built, modeled, and tested. The results showed that the use of such signals could indeed optimize the performance of RF-dc converters. The tests also enabled a study of the impact on performance of the transmitting and receiving antennas in the wireless power transfer system.

The topic of the paper by Michael Duarte, Tiago Varum, João Matos, and Pedro Pinho is the design of 17 GHz antennas for Wi-Fi applications. Microstrip patch antennas were used. The challenge of feeding such a structure at this frequency was addressed. Two different designs were considered, one with a crossed slot and one with an off-centered feed. A 4×4 array was also designed. It was shown that the primary difference resulting from the different feeding arrangement was in the polarization.

Our Other Contributions

Stefan Wijnholds and Asta Pellinen-Wannberg have combined their efforts to bring us a joint Early Career Representative/Women in Radio Science column this time. The subject is a commentary from Jamesina Simpson, who received the Santimay Basu Prize at the 2017 URSI GASS in Montreal. I think you will find her comments on learning and teaching very interesting.

Randy Haupt and Amy Shockley discuss Price's Law in their Ethically Speaking column. This is a relationship that states that half of the publications in any given field are produced by the square root of the number of all contributors. However, there are related relationships that apply to many other quantities than publications. The results lead to some interesting ethical questions.

In the Solution Box, Muhammed Tonga, Barışcan Karaosmanoğlu, and Özgür Ergül present some solutions to problems that are multi-scale. These employ significantly different levels of discretization over different ranges in order to produce time-efficient and accurate solutions. The scattering geometries are canonical (a sphere and a cube). However, the size of the mesh discretization is varied over the surfaces of the scatterers over a range of almost 30:1.

The topic of Jim Lin's Telecommunications Health and Safety column is an analysis of and comments on the conclusions from a peer review panel of the US National Institute of Environmental Health Sciences' (NIEHS) National Toxicology Program (NTP), a part of the US National Institutes of Health (NIH). Earlier this year, the panel concluded that, among other observations, there was statistically significant and "clear evidence" that both GSM- and CDMA-modulated RF radiation had led to the development of malignant schwannoma, a rare form of tumor in the heart of male rats, and there was "equivocal evidence" for the same schwannoma risk among female rats. The column explains what led to these findings, analyzes the process used, and looks at the potential implications for the current safe RF exposure guidelines.

You Can Still Submit to AP-RASC!

The URSI Asia-Pacific Radio Science Conference (AP-RASC 2019) will be held March 9-15, 2019, in New Delhi, India. There is still time to submit a paper to this important conference, one of the main URSI flagship conferences. The submission deadline is **October 15, 2018**. A call for papers appears in this issue. I urge you to submit a paper and plan on attending this conference.

Introduction to the Special Issue on the 11th Congress of the Portuguese Committee of URSI Best Student Paper Award Contest

Pedro Miguel Cruz[1], António Topa[2], and Tiago A. Morgado[3]

[1]Controlar, Lda.
Early Career Representative (ECR)
URSI Commission A
E-mail: pedro.cruz@controlar.pt

[2]Instituto Superior Técnico
Universidade de Lisboa
E-mail: antonio.topa@lx.it.pt

[3]Instituto de Telecomunicações – Coimbra
Department of Electrical Engineering of the University of Coimbra (DEEC-FCTUC)
E-mail: tmorgado@co.it.pt

The Portuguese Committee of URSI held its 11th Congress on November 24, 2017, at the Fundação Portuguesa das Comunicações in Lisbon, under the theme "New Technologies for Mobility."

In an increasingly global world, where transport systems are always fast, automated, and intelligent, new technologies play a key role. They facilitate the introduction of new paradigms, which introduce significant efficiency gains and improve the quality of the services that are offered to users. Intelligent mobility takes advantage of the use of real-time tools to optimize routes and energy consumption, greatly contributing to increasing the safety of the means of transport, and providing up-to-date information to the users, globally providing better and more-integrated management of operations.

Repeating the recipe from previous years, and in a way to encourage the involvement of young researchers and students, the meeting organizers received 12 applications for the Best Student Paper Award (BSPA) that were authored and orally presented by each of the candidates. The Best Student Paper Award jury committee, together with the meeting organization selected three winners. First place was Carolina Gouveia. Second place was Hafssaa Latioui, and third place was Vera da Silva Pedras. During the closing session, certificates and financial support, sponsored by ANACOM, were given to these winners (Figure 1).

After the event, all Best Student Paper Award participants were invited to submit an extended paper for inclusion in this issue of the URSI *Radio Science Bulletin*. An interesting number of extended submissions was received. This was followed by a careful review process by knowledgeable peers together with the guest editorial team, culminating in five manuscripts accepted for final publication.

The Guest Editors and ANACOM-URSI Portugal would like to express their sincere gratitude to Dr. Ross Stone (Editor) for the opportunity to publish this special issue in the URSI *Radio Science Bulletin*, and to thank all the reviewers for their valuable time and expertise invested in the various steps of the review of the extended papers.

Figure 1. The winners of the Best Student Paper Award from the 11th Congress of the Portuguese Committee of URSI (l-r): Hafssaa Latioui, Vera da Silva Pedras, and Carolina Gouveia.

PCI and RSI Conflict Detection in a Real LTE Network Using Supervised Learning

R. Veríssimo[1], P. Vieira[2,3], A. Rodrigues[1,3], and M. P. Queluz[1,3]

[1]Instituto Superior Técnico
University of Lisbon
Portugal
E-mail: rodrigo.verissimo@ist.utl.pt

[2]Instituto Superior de Engenharia de Lisboa
Instituto Politécnico de Lisboa
Portugal
E-mail: pvieira@deetc.isel.pt

[3]Instituto de Telecomunicacões
Lisbon, Portugal
E-mail: [ar, paula.queluz]@lx.it.pt

Abstract

This paper tests two hypotheses regarding how well two distinct Long-Term Evolution (LTE) network problems can be detected through supervised techniques with near-real-time performance. The tested network problems are physical-cell-identity (PCI) conflicts and root-sequence-index (RSI) collisions. These were labeled through configured cell relations that verified these two conflicts. Furthermore, a real LTE network was used. The results obtained showed that both problems were best detected by using each key performance indicator (KPI) measurement as an individual feature. The highest average precisions obtained for PCI conflict detection were 31% and 26% for the 800 MHz and 1800 MHz frequency bands, respectively. The highest average precisions obtained for RSI collision detection were 61% and 60% for the 800 MHz and 1800 MHz frequency bands, respectively.

1. Introduction

Two of the major concerns of mobile network operators (MNO) are to optimize and to maintain network performance. However, maintaining performance has proven to be a challenge mainly for large and complex networks. In the long term, changes made in the networks may increase the number of conflicts and inconsistencies that occur in them. These changes include changing the tilting of antennas, changing the cell's power, or even changes that cannot be controlled by the mobile network operators, such as user mobility and radio-channel fading.

In order to assess the network's performance, quantifiable performance metrics, known as key performance indicators (KPI), are typically used. Key performance indicators can report network performance such as the handover success rate and the channel interference averages of each cell, and are periodically calculated, resulting in time series. A time series can be either univariate or multivariate. As this study uses data samples that represent LTE cells with several measured key performance indicators, then the data consist of multivariate time series.

This paper focuses on applying supervised techniques for detecting two known LTE network conflicts, namely physical-cell identity (PCI) conflicts and root-sequence index (RSI) collisions. The labeling used was only possible due to a CELFINET product that allows obtaining cell relations that label the two mentioned network conflicts; also, real data obtained from a LTE network was used. The aim of this paper is to test two hypotheses regarding how well two distinct LTE network problems can be detected through supervised techniques with near-real-time performance. The resulting conflict-detection solution would then run in an entity external from the LTE architecture during the early morning. The solution would then alert the network engineers of any existing conflicts in order to have prompt responses.

As this paper aims to create models for near-real-time detection of PCI conflicts and RSI collisions, the popular k-nearest neighbors with dynamic-time-warping classification approach was not tested [1]. The reason for this decision was based on the fact that it is computationally intensive and very slow for large data sets, as was the case for this paper.

In order to automatically detect the network fault causes, some work has been done by using key performance indicator measurements with unsupervised techniques, as in[2].

The paper is organized as follows. Section 2 introduces the analyzed network problems, namely PCI conflicts and RSI collisions. Section 3 presents the chosen key performance indicators and machine-learning (ML) models, the two proposed hypotheses, and describe how the models obtained were evaluated. Section 4 presents the results obtained. Finally, conclusions are drawn in Section 5.

2. Network Problems Analyzed

2.1 Physical Cell Identity Conflict

Each LTE cell has two identifiers with different purposes: the Global Cell Identity (ID) and the PCI. The Global Cell ID is used to identify the cell from an operation, administration, and management perspective. The PCI is used to scramble the data in order to aid mobile phones in separating information from different transmitters [3]. Since an LTE network may contain a much larger number of cells than the 504 available values of PCIs, the same PCI must be reused by several cells. However, the user equipment (UE) cannot distinguish between two cells if they both have the same PCI and frequency, a situation called as PCI conflict.

PCI conflicts can be divided into two cases: PCI confusions and PCI collisions. PCI confusions occur whenever an LTE cell has two different neighbor LTE cells with equal PCIs, in the same frequency band [4]. PCI collisions happen whenever an LTE cell has a neighbor LTE cell with identical PCI in the same frequency band [4].

A good PCI plan can be applied to avoid PCI conflicts. However, it can be difficult to do such a plan without getting any PCI conflicts in a dense network. Moreover, network changes – namely increased cell power and variable radio conditions – can lead to PCI conflicts. PCI conflicts can lead to an increase in dropped-call rate due to failed handovers, as well as an increase of blocked calls and channel interference [4].

2.2.2 Root Sequence Index Collision

The user equipment has to perform the LTE random-access procedure to connect to an LTE network, establish or reestablish a service connection, perform intra-system handovers, and synchronize for uplink and downlink data transfers. The LTE random-access procedure can be performed using two different solutions: allowing non-contention-based and contention-based solutions. An LTE cell uses 64 physical random-access channel (PRACH) preambles. Twenty-four of those preambles are reserved by the evolved-NodeB for non-contention-based access. The remaining 40 preambles are randomly selected by the user equipment for contention-based access [3].

The 40 physical random-access-channel preambles that the user equipment can use are calculated by the user equipment through the RSI parameters that the LTE cell transmits in the system information block 2 through the physical random-access channel [5]. Whenever two or more neighbor cells operate in the same frequency band and have the same RSI parameter, this results in the connected user equipment calculating the same 40 physical random-access channel preambles, increasing the occurrence of preamble collisions. The aforementioned problem is known as RSI collision, and can lead to an increase of failed service establishments and re-establishments, as well as an increase of failed handovers.

3. Methodology

This study was performed using real data from an LTE network of a mobile network operator with a PCI reuse factor of three. Furthermore, data were collected for the same weekday of three consecutive weeks, for every period of 15 minutes, the minimum temporal granularity used by network operators, resulting in a daily total of 96 measurements.

Using a CELFINET tool, it was possible to label cells that had PCI conflicts and/or RSI collisions. Source cells that had configured neighbor cells with equal PCI in the same frequency band were labeled as having a PCI collision. Source cells that had two or more neighbor cells with equal PCI in the same frequency band between themselves were labeled as having a PCI confusion. Source cells that had neighbor cells with equal RSI in the same frequency band were labeled as having an RSI collision. Cells that did not present any of these conflicts were labeled as non-conflicting.

3.1 Proposed Key Performance Indicators

The first step involved in collecting a list of key performance indicators for LTE equipment was to choose the most-relevant key performance indicators for detecting PCI conflicts and RSI collisions. The key performance indicators were chosen by taking into account the theory behind LTE and how PCI and RSI are used. Accordingly, the following key performance indicators were chosen for PCI conflict detection:

- Average CQI: the average channel quality indicator measured by the user equipment
- UL PUCCH Interference Avg and UL PUSCH Interference Avg: the average measured interference in the physical uplink control and shared Channel
- Service Establish: the amount of established service connections

- Service Drop Rate: the ratio of the dropped service occurrences
- DL Avg Cell Throughput Mbps: the average measured cell downlink throughput in Mbit/s
- DL Avg User Equipment Throughput Mbps: the average measured user equipment downlink throughput in Mbit/s
- DL Latency ms: the average duration an Internet protocol packet takes since being sent by the user equipment until reaching back to it
- RandomAcc Succ Rate: the success rate of established services made through the random access channel
- IntraFreq Prep HO Succ Rate and IntraFreq Exec HO Succ Rate: the success rate of handover preparation and execution between cells operating in the same frequency band.

To detect RSI collisions, a subsection of the aforementioned key performance indicators were selected, namely: UL PUCCH Interference Avg, UL PUSCH Interference Avg, Service Establish, IntraFreq Exec HO Succ Rate, IntraFreq Prep HO Succ Rate, and RandomAcc Succ Rate.

After discarding cells with high null key performance indicator measurements and interpolating those of the remaining cells, it was decided to separate the data into different frequency bands, namely the 800 MHz and 1800 MHz bands. The 2100 MHz and 2600 MHz frequency bands were not considered, as they represented only 9% of the data, and had few occurrences of PCI conflicts and RSI collisions. This decision to separate the data into different frequency bands was taken in order to create frequency-dependent models, since different frequency bands have different purposes.

The cleaned data for PCI conflict detection in the 800 MHz frequency band consisted of 8666 non-conflicting cells, 1551 PCI confusions, and six PCI collisions. The 1800 MHz frequency-band data had 16675 non-conflicting cells, 1294 PCI confusions, and no PCI collisions. The data concerning each frequency band was split into 80% for the training set and 20% for the test set. Additionally, as PCI collisions are very rare, it was decided to do a 50% split for collisions, yielding three collisions in both the training and test sets.

The cleaned data for RSI collision detection in the 800 MHz frequency band consisted of 10128 non-conflicting cells and 6774 RSI collisions. The 1800 MHz frequency-band data consisted of 17634 non-conflicting cells and 10916 RSI collisions. The data relative to each frequency band was split into 80% for the training set and 20% for the test set.

3.2 Considered Classification Algorithms

In order to reduce the bias from this study, five different classification algorithms were set. The aim of the classifiers was to classify cells as either non-conflicting or conflicting, depending on the detection use case. The considered classification algorithm implementations were taken from the Python Scikit-Learn library [6], and were the following:

3.2.1 Adaptive Boosting (AB)

Adaptive Boosting is an ensemble method, which is a class of a machine-learning approaches based on the concept of creating a highly accurate classifier by combining several weak and inaccurate classifiers. Adaptive Boosting uses subsets of the original data to produce weak performing models (high bias, low variance) and then boosts their performance by combining them together based on a chosen cost function. Adaptive Boosting was the first practical boosting algorithm, and remains one of the most used and studied classifiers [7]. Its implementation uses decision-tree classifiers as weak learners.

3.2.2 Gradient Boost (GB)

Gradient Boost is another popular boosting algorithm for creating collections of classifiers. It differs from Adaptive Boosting because it calculates a negative gradient of a cost function (direction of quickest improvement), and picks a weak learner that is closest to the obtained gradient to add to the model [8]. The Gradient Boost implementation considered uses Decision Trees (DT) as weak learners.

3.2.3 Extremely Randomized Trees (ERT)

This belongs to the family of tree ensemble methods, and uses a technique different from boosting, known as bagging. Bagging-based algorithms aim to control generalization error by perturbing and averaging the generated weak learners, such as decision trees. The Extremely Randomized Trees algorithm stands out from other tree-based ensemble classifiers because it strongly randomizes both feature and cut-point choice while splitting a tree node [9]. Extremely Randomized Trees aims to strongly reduce variance through a full randomization of the cut-point and feature combined with ensemble averaging when compared to other algorithms. By training each weak learner with the full training set instead of data subsets, Extremely Randomized Trees also minimizes bias.

3.2.4 Random Forest (RF)

Random Forest is another bagging-based algorithm in the family of tree ensemble methods. Similarly to Extremely Randomized Trees, several small and weak trees can be grown in parallel, and these set of weak learners result in a strong classification algorithm either by averaging or by majority vote [10]. Random Forest is similar to Extremely Randomized Trees, but differs in two aspects. Random Forest uses data subsets for growing its trees, while Extremely Randomized Trees uses the whole training set. Random Forest chooses a small subset of features to be chosen on splitting a node, while Extremely Randomized Trees chooses a random feature from all features.

3.2.5 Support Vector Machines (SVM)

Support Vector Machines aim to separate data samples of different classes through hyperplanes that define decision boundaries. Similarly to Decision-Trees-based classifiers, Support Vector Machines are capable of handling linear and nonlinear classification tasks. The main idea behind Support Vector Machines is to map the original data samples from the input space into a high-dimensional feature space such that the classification task becomes simpler [11].

3.3 Proposed Hypotheses

In order to reduce bias even further, two hypotheses were proposed to find the one that led to the best-performing models for PCI conflict and RSI collision detection.

3.3.1 Statistical Data Extraction Classification

PCI conflicts and RSI collisions are better detected by extracting statistical calculations from the daily time series of each key performance indicator and using them as features for classification. The Python `tsfresh` tool was used to extract statistical data from the time series [12]. `tsfresh` applies several statistical calculations to the data, followed by feature elimination through statistical significance testing. As it resulted in hundreds of features, Principal Component Analysis (PCA) was applied for dimensionality reduction before applying the data into the Support Vector Machine classifier. This decision was taken because Support Vector Machine takes longer to converge as the dimensionality increases, while it does not significantly increase the training and testing times of the tree-based classifiers. It was decided to use a number of principal components (PC) that led to 98% of the cumulative proportion of variance explained, maintaining most of the original variance.

3.3.2 Raw Cell Data Classification

PCI conflicts and RSI collisions are better detected by using each cell's daily key performance indicator measurements as an individual feature. This hypothesis was proposed to compare a more computationally intensive but simpler approach with the previous hypothesis. Moreover, as there were 96 daily measurements per key performance indicator in each cell, by using, for instance, 10 key performance indicators, this would have yielded $96 \times 10 = 960$ features. Due to the high dimensionality of the data to test this hypothesis, Principal Component Analysis was applied (once again) to reduce its dimensionality before using the Support Vector Machine classifier. It was decided to use a number of principal components that led to 98% of the cumulative proportion of variance explained.

3.4 Model Evaluation

In a binary decision problem, a classification algorithm labels predictions as either positive or negative. A prediction for conflict detection could fit into one of these four categories: True Positive (TP), conflicting cells correctly labeled as conflicting; False Positive (FP), non-conflicting cells incorrectly labeled as conflicting; True Negative (TN), non-conflicting cells correctly labeled as non-conflicting; False Negative (FN), conflicting cells incorrectly labeled as non-conflicting.

As there was a high interest in knowing how well the models obtained could classify PCI conflicts and RSI collisions, the classic accuracy metric by itself was not enough. Classifications where a non-conflicting cell was erroneously classified as a conflict were to be avoided; it was thus chosen to additionally evaluate the models obtained through the precision and recall metrics. The metrics used could then be defined as follows:

$$Recall = \frac{TP}{TP + FN}, \tag{1}$$

$$Precision = \frac{TP}{TP + FP}, \tag{2}$$

$$Accuracy = \frac{TP + TN}{TP + TN + FP + FN}, \tag{3}$$

where *Recall* measures the fraction of conflicting cells that are correctly labeled, *Precision* measures the fraction of cells classified as conflicting that are truly conflicting, and *Accuracy* measures the fraction of correctly classified cells [13]. *Precision* can be thought of as a measure of a classifier's exactness – a low precision can indicate a large

number of False Positives – while *Recall* can be seen as a measure of a classifier's completeness: a low recall indicates many False Negatives.

Since a classification algorithm can output the probabilities of a sample belonging to a specific class, the probability decision threshold can be tuned to alter the model's classification outputs. For instance, increasing the probability decision threshold to classify a specific class may lead to an increase in *Precision* at the cost of a lower *Recall*. *Precision-Recall* (PR) curves are built by changing the decision probability threshold for a class. It thus was decided to also evaluate models through their *Precision-Recall* curves in order to perform a thorough model evaluation. *Precision-Recall* curves, often used in information retrieval [14], have been cited as an alternative to Receiver Operator Characteristic curves for tasks with a large skew in the class distribution, as in PCI conflict detection [15]. Additionally, the average *Precision* is also represented by the *Precision-Recall* curves through the areas under the curves. It should be noted that there is a tradeoff between the number of samples for model training, training duration, and model performance. With more data samples and more training time, the resulting model generalizes better and has more time to learn the data structure.

4. Results

4.1 Physical Cell Identity Conflict Detection

4.1.1 Statistical Data Extraction Classification

The first hypothesis presented in Section 3.3 was tested using the data presented in Section 3.1. Regarding PCI confusion detection, `tsfresh` yielded 798 and 909 significant features for the 800 MHz and 1800 MHz frequency bands, respectively. Concerning PCI collision detection, a total of 2200 features were extracted for the 800 MHz case that were not selected through hypothesis testing, due to the dataset only containing a marginally low number of six PCI collisions. Principal Component Analysis was applied for dimensionality reduction for a faster Support Vector Machine convergence. For PCI confusion detection, this resulted in 273 and 284 principal components for the 800 MHz and 1800 MHz frequency bands, respectively.

The optimal hyperparameters to create each model were obtained through a grid search on the training set with 10-fold cross validation, maximizing the *Precision* metric. After training the models, they were tested on the test set, based on a decision probability threshold of 50%. The results are presented in Table 1.

It should be added that when a classifier did not classify any True Positives or False Positives, the *Precision* was represented as a Not a Number (NaN), since it resulted in a division by zero. The Adaptive Boosting model had the best performance, with a 50% *Precision* for the 800 MHz frequency band. However, no model classified a sample as conflicting in the 1800 MHz frequency band data.

In order to obtain more insights about the models' performance, the *Precision-Recall* curves were obtained, and are represented in Figure 1. The highest average *Precision* was 27%, by using the Gradient Boost classifier. The Gradient Boost presented the highest *Precision* mostly throughout the plot. The Support Vector Machine was clearly the worst-performing model, especially in the 1800 MHz frequency band.

The training and testing running times to obtain the *Precision-Recall* curves were also collected. Gradient Boost, which resulted in the two best models, had a testing time below one second and a training time below 30 seconds for both frequency bands. The learning curves were obtained, and they showed that the average *Precision* would only marginally increase with more data. Gradient Boost thus resulted in the overall best-performing models for both frequency bands by using statistical calculations as features.

Regarding PCI collision detection, Principal Component Analysis resulted in 619 principal components to be used by the Support Vector Machine classifier for the 800 MHz frequency band. The optimal hyperparameters were obtained, and the test results were collected after training the models. A table with the results is not shown, as no tested model was able to classify a sample as conflicting. The *Precision-Recall* curves were obtained and plotted, showing a maximum *Precision* of 23% with 100% *Recall* by Random Forest, while this was approximately zero for the remaining classifiers (the plot is not illustrated in this paper as it would not add much information).

Table 1. Statistical-data-based PCI confusion classification results.

	800 MHz Band			1800 MHz Band		
Model	**Accuracy**	**Precision**	**Recall**	**Accuracy**	**Precision**	**Recall**
ERT	**85.24%**	NaN	00.00%	**93.27%**	NaN	00.00%
RF	**85.24%**	NaN	00.00%	**93.27%**	NaN	00.00%
SVM	**85.24%**	NaN	00.00%	**93.27%**	NaN	00.00%
AB	**85.24%**	**50.00%**	**02.83%**	**93.27%**	NaN	00.00%
GB	85.18%	46.00%	02.43%	**93.27%**	NaN	00.00%

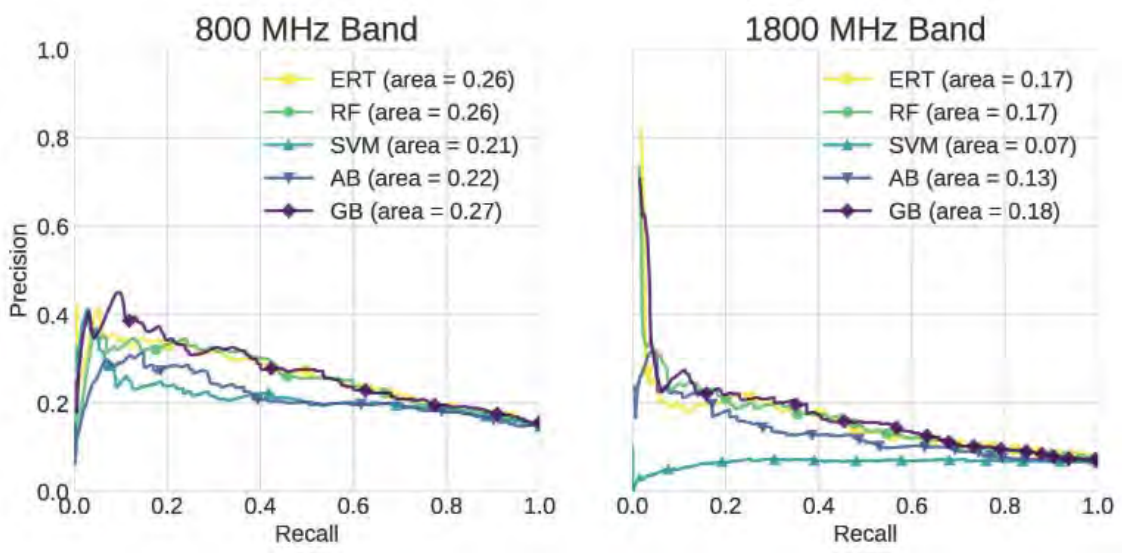

Figure 1. The smoothed *Precision-Recall* curves for statistical-data-based PCI confusion detection.

4.1.2 Raw Cell Data Classification

The second hypothesis presented in Section 3.3 was tested using the data described in Section 3.1. Using each individual key performance indicator measure as a feature, an average filter with a window of size 20 was applied to reduce the noise interference. Principal Component Analysis was applied, which resulted in 634 principal components to be used by the Support Vector Machine classifier for both the 800 MHz and 1800 MHz frequency bands.

Once again, the optimal hyperparameters were obtained through grid search, and the test results were collected after model training. The classification results for a 50% decision probability threshold are shown in Table 2. Overall, Gradient Boost was the classifier that led to the best performance, having the highest *Accuracy* and *Recall* for both frequency bands, but not the best *Precision* for the 1800 MHz frequency band. Both models created by the Extremely Randomized Trees and Random Forest classifiers had a 100% *Precision* for the 1800 MHz frequency band, which meant that Random Forest could result in the best model, as it had higher *Recall*.

In order to see if Gradient Boost led to the best performing model, the *Precision-Recall* curves were obtained, and they are presented in Figure 2. Regarding the 800 MHz frequency band, Gradient Boost showed the highest average *Precision*, with a peak of 60% *Precision* for 4% *Recall*. Concerning the 1800 MHz frequency band, Extremely Randomized Trees presented the best average *Precision*, while Gradient Boost achieved higher *Precision* for a *Recall* lower than 5%. Additionally, Random Forest was not the best performing model, as was seen in Table 2.

The training and testing running times for each model were obtained. In the 800 MHz frequency band, Gradient Boost, which led to the best-performing model, had a testing time below one second and a training time below 14 seconds. Regarding the 1800 MHz frequency band, Extremely Randomized Trees, which led to the best-performing model, was one of the quickest to train (i.e., 40.3 seconds), but it was one of the slowest to test (i.e., 1.4 seconds). Nevertheless, its overall performance was near real time.

Regarding PCI collision detection, Principal Component Analysis resulted in 634 principal components for both frequency bands. The test results were collected with the optimal hyperparameters. The best performing model was the model obtained from Adaptive Boosting, as it detected one out of three PCI collisions with 100% *Precision*. However, due to the marginally low number of PCI collisions in the dataset, the results were not sufficiently significant to draw any conclusions.

Table 2. Raw-cell-data PCI confusion classification results.

	800 MHz Band			1800 MHz Band		
Model	**Accuracy**	**Precision**	**Recall**	**Accuracy**	**Precision**	**Recall**
ERT	85.37%	22.22%	00.71%	93.57%	**100%**	00.45%
RF	85.63%	NaN	00.00%	93.60%	**100%**	00.90%
SVM	85.63%	NaN	00.00%	93.54%	NaN	00.00%
AB	85.63%	NaN	00.00%	93.54%	NaN	00.00%
GB	**85.73%**	**75.00%**	**01.07%**	**93.63%**	80.00%	**01.80%**

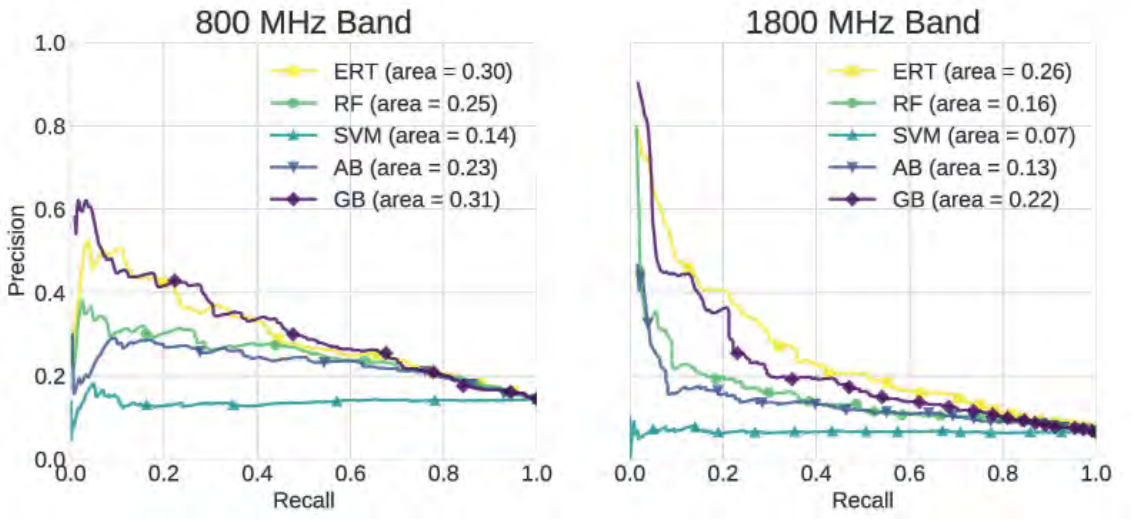

Figure 2. The smoothed *Precision-Recall* curves for raw-cell-data-based PCI confusion detection.

4.2 Root Sequence Indicator Collision Detection

4.2.1 Statistical Data Extraction Classification

The first hypothesis presented in Section 3.3 was tested using the data described in Section 3.1. Regarding RSI collision detection, `tsfresh` yielded 732 and 851 significant extracted features for the 800 MHz and 1800 MHz frequency bands, respectively. In order to reduce the data dimensionality for applying to the Support Vector Machine model, Principal Component Analysis was applied, resulting in 273 and 284 principal components for the 800 MHz and 1800 MHz frequency bands, respectively.

The optimal hyperparameters were obtained through grid search, and the test results are presented in Table 3. The Extremely Randomized Trees model delivered the highest *Precision* for both frequency bands, but Gradient Boost had the highest overall *Accuracy* and *Recall*.

In order to gain more insights regarding the performance of the models, *Precision-Recall* curves were obtained and are presented in Figure 3. The Gradient Boost model was the best for both frequency bands, having a *Precision* peak of 85% and an average *Precision* of 61%. The abnormal curve behavior of the Adaptive Boosting model was due to the assignment of several cells with the same probability values.

The training and testing running times for each model were obtained. The Gradient Boost model showed testing times lower than one second; however, it had one of the highest training times. More specifically, it required 28.4 and 246 seconds of training time for the 800 MHz and 1800 MHz frequency bands, respectively. Nonetheless, the Gradient Boost model presented higher performance relative to other obtained models with near-real-time performance, thus overall being the best model. The learning curves obtained showed that the performance would not significantly increase if more data were added to the dataset.

4.2.2 Raw Cell Data Classification

The second hypothesis presented in Section 3.3 was tested using the data described in Section 3.1. Using each individual key performance indicator's measure as a feature, an average filter with a window of size 20 was applied. Principal Component Analysis was applied, which yielded in 332 principal components to be used by the Support Vector Machine classifier for both the 800 MHz and 1800 MHz frequency bands for RSI collision detection.

The optimal hyperparameters were obtained through grid search, and the results are presented in Table 4. Once

Table 3. Statistical-data-based RSI collision classification results.

	800 MHz Band			1800 MHz Band		
Model	**Accuracy**	**Precision**	**Recall**	**Accuracy**	**Precision**	**Recall**
ERT	60.32%	**100%**	00.48%	62.27%	**72.97%**	02.00%
RF	64.93%	61.30%	32.62%	64.13%	66.94%	12.12%
SVM	60.94%	54.80%	11.55%	61.79%	NaN	00.00%
AB	64.02%	56.79%	40.83%	66.37%	59.88%	36.29%
GB	**66.87%**	61.60%	**44.88%**	**69.39%**	63.97%	**45.53%**

Table 4. Raw-cell-data RSI collision classification results.

	800 MHz Band			1800 MHz Band		
Model	**Accuracy**	**Precision**	**Recall**	**Accuracy**	**Precision**	**Recall**
ERT	59.49%	50.00%	00.83%	59.83%	**75.00%**	00.22%
RF	61.70%	**62.64%**	13.52%	65.55%	63.86%	33.07%
SVM	60.07%	52.24%	16.61%	59.25%	46.67%	09.14%
AB	64.73%	60.38%	37.60%	64.99%	59.59%	**40.32%**
GB	**66.41%**	60.84%	**47.92%**	**66.22%**	62.72%	39.52%

more, the Gradient Boost model revealed more *Accuracy* for both frequency bands. The Random Forest and Extremely Randomized Trees models had the highest *Precision* for the 800 MHz and 1800 MHz frequency bands.

The *Precision-Recall* curves were obtained and are presented in Figure 4. The Gradient Boost model had the highest average *Precision*, while the Random Forest and Extremely Randomized Trees models showed slightly worse average *Precision*.

The training and testing running time for each model were obtained. The Gradient Boost model showed testing times lower than one second, and the third highest training times for both frequency bands. More precisely, it took 12.8 and 24.4 seconds to train in the 800 MHz and 1800 MHz frequency bands, respectively. However, the Gradient Boost model's performance was in near real time, and it was thus overall the best-performing model. The learning curves obtained showed that the results would improve if more data were added to the training set, especially for the Gradient Boost model.

5. Conclusions

This paper tested two hypotheses regarding how well two distinct LTE network problems could be detected through supervised techniques with near-real-time performance.

The PCI confusions were better detected by using the measurement of each cell's daily key performance indicators as an individual feature. This was concluded due to the result that the average *Precision* was higher while testing this hypothesis. Specifically, the average *Precision*s reached 31% and 26% for the 800 MHz and 1800 MHz frequency bands, respectively. No conclusions could be reached regarding PCI collision detection due to the low number of PCI collisions in the data set.

The RSI collisions were detected with similar performance by two proposed hypotheses. However, one could say that the best detection was obtained by using the measurement of each cell's daily key performance indicators as an individual feature because the learning curves showed that the results would further improve if more data was added for the second hypothesis. The best-performing model was the model that used the Gradient Boost classifier, reaching average *Precision*s of 61% and 60% for the 800 MHz and 1800 MHz frequency bands, respectively.

The results showed that supervised techniques for PCI and RSI conflict detection are not well suited. This is because while a cell may have one of these two conflicts, the conflict's impact on the key performance indicators might be negligible. This fact can be due to several factors, such as the distance between cells, their azimuth, and the environment. For future work, an unsupervised approach for network conflict detection followed by manual labeling to be used by a classifier could be investigated. This would

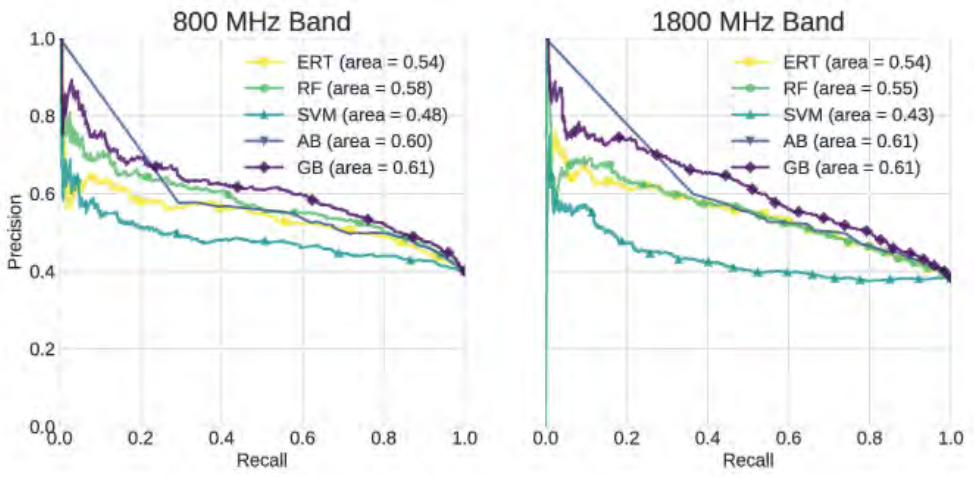

Figure 3. The smoothed *Precision-Recall* curves for statistical-data-based RSI collision detection.

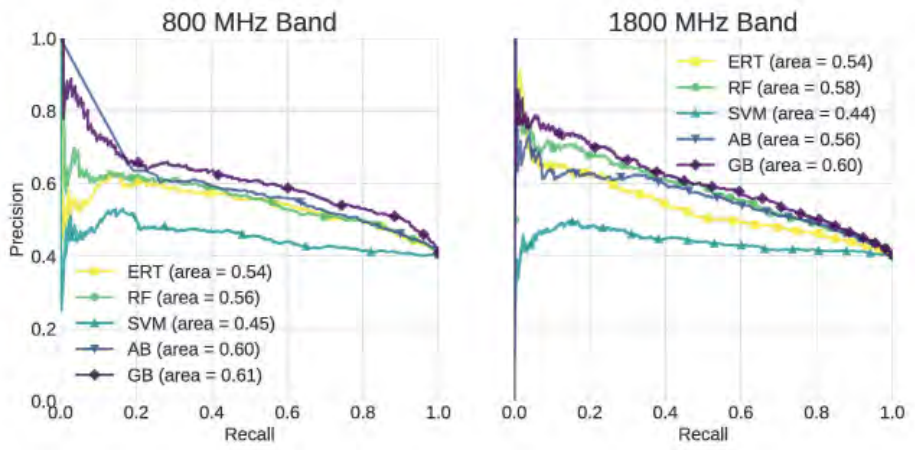

Figure 4. The smoothed *Precision-Recall* curves for raw-cell-data RSI collision detection.

result in the labeling of cells with significant differences between them, which could lead to better classification results.

6. Acknowledgments

The authors would like to thank FCT for the support by the project UID/EEA/50008/2013. Moreover, we acknowledge project MESMOQoE (No. 023110- 16/SI/2016), supported by Norte Portugal Regional Operational Programme (NORTE 2020), under the PORTUGAL 2020 Partnership Agreement, through the European Regional Development Fund. The authors would also like to thank CELFINET for the key performance indicator measurements.

7. References

1. X. Wang et al., "Experimental Comparison of Representation Methods and Distance Measures for Time Series Data," *Data Mining and Knowledge Discovery*, **26**, 2, March 2013, pp. 275-309.

2. A. Gómez-Andrades et al., "Automatic Root Cause Analysis for LTE Networks Based on Unsupervised Techniques," *IEEE Transactions on Vehicular Technology*, **65**, 4, 2016, pp. 2369-2386.

3. H. Holma and A. Toskala, *WCDMA for UMTS: HSPA Evolution and LTE, Fourth Edition*, New York, Wiley Publishing, 2017.

4. Acedo-Hernández et al., "Analysis of the Impact of PCI Planning on Downlink Throughput Performance in LTE," *Computer Networks*, **76**, C, January 2015, pp. 42-54.

5. C. Cox, *An Introduction to LTE, LTE-advanced, SAE, VoLTE and 4G Mobile Communications, Second Edition*, New York, Wiley Publishing, 2014.

6. F. Pedregosa et al., "Scikit-Learn: Machine Learning in Python," *Journal of Machine Learning Research*, **12**, November 2011, pp. 2825-2830.

7. J. Zhu et al., "Multi-Class AdaBoost," *Statistics and Its Interface*, **2**, 3, 2009, 10.4310/SII.2009.v2.n3.a8.

8. A. Natekin and A. Knoll, "Gradient Boosting Machines, A Tutorial," *Frontiers in Neurorobotics*, **7**, 2013.

9. P. Geurts, D. Ernst, and L. Wehenkel, "Extremely Randomized Trees" *Machine Learning*, **63**, 1, April 2016, pp. 3-42.

10. L. Breiman, "Random Forests," *Machine Learning*, **45**, 1, October 2011, pp. 5-32.

11. C.-W. Hsu, C.-C. Chang, and C.-J. Lin, "A Practical Guide to Support Vector Classification," Technical Report, Department of Computer Science and Information Engineering, University of National Taiwan, Taipei, 2003.

12. M. Christ, "Tsfresh," https://github.com/blue-yonder/tsfresh, 2016.

13. J. Davis and M. Goadrich, "The Relationship Between Precision-Recall and ROC Curves," Proceedings of the 23rd International Conference on Machine Learning, ICML '06, New York, ACM, 2006, pp. 233-240.

14. C. D. Manning and H. Schütze, *Foundations of Statistical Natural Language Processing*, Cambridge, MA, MIT Press, 1999.

15. M. Goadrich, L. Oliphant, and J. Shavlik, *Learning Ensembles of First-Order Clauses for Recall-Precision Curves: A Case Study in Biomedical Information Extraction*, Berlin, Springer Berlin Heidelberg, 2004, pp. 98-115.

A Novel and Realistic Power Consumption Model for Multi-Technology Radio Networks

Alexandra Mourato[1], David Duarte[2,3], Iola Pinto[1,4], and Pedro Vieira[1,3]

[1]Instituto Superior de Engenharia de Lisboa
[2]CELFINET
Consultoria em Telecomunicações Lda.
Lisboa, Portugal
E-mail: a39135@alunos.isel.pt
E-mail: david.duarte@celfinet.com

[3]Instituto de Telecomunicações
Lisboa, Portugal
E-mail: pvieira@deetc.isel.pt

[4] Centro de Matemática e Aplicações
FCT/UNL
Lisboa, Portugal
E-mail: ipinto@deetc.isel.ipl.pt

Abstract

Previous research studies have shown that about 10% of the world's energy is consumed by information-communication technology (ICT) infrastructures, mainly generated by nonrenewable sources. Combining global warming with the operational expenditure (OPEX) of mobile operators, it is demanding to understand and develop strategies to reduce the energy consumed. An effort to increase the energy efficiency of these technologies has become a major challenge for future telecommunications systems. The aim of this paper is to develop an energy consumption model for second-generation (2G), third-generation (3G), and fourth-generation (4G) base stations (BSs). In a real network, we investigated the effects of voice and data traffic variations on base-station power consumption. Other features, such as base-station transmitted power, cell availability, or resources allocated to users, were also considered. The models considered supervised learning techniques based on regression analysis, and the result was the predicted base-station power consumption, which was compared with real energy measurements from monitoring equipment installed on site. For validation purposes, metrics such as the Pearson correlation, the root-mean-square error (RMSE), and the mean-absolute-percent error (MAPE), were used. The proposed approach showed the potential of these technologies with regard to energy efficiency, achieving the objective of savings in the power consumption of the operators.

1. Introduction

1.1 Overview

The mobile telecommunications industry deals with countless expenses, both operational and capital. The sky-rocketing technological evolution at the consumer side, based on a massive exchange of data, needs a highly available network framework with abundant resources. This is possible with new and more efficient radio-access technologies (RATs) and increasing efficiency of communication between the radio-access network (RAN) and the network's core. Currently, network providers simultaneously operate with different radio-access technologies, in different frequency bands, providing increased capacity and coverage to users, but unfortunately with added costs due to additional equipment. The ICT is responsible for about 10% of global energy consumption [1]. In mobile communications, the base stations consume most of the system's energy, 70% being spent on amplifiers and cooling systems [2].

It is hence important for the operators to measure with accuracy the base-station power consumption in the radio-access network, not only at the site level, but also in a more-detailed way, by measuring the specific energy consumption in the main base-station components, from radio to baseband unit (BBU) or even in transmission. In order to reduce energy costs, this detailed knowledge around

energy consumption is thus vital, since it allows analyzing future hardware and software upgrades.

The aim of this paper is to develop an energy-consumption model for the three technologies present in current base stations, namely 2G, 3G, and 4G. The models were developed based on real performance management (PM) statistics from a mobile operator, collected at six different sites in different environments. Power-measuring equipment was installed in these base stations in all of the different radio and baseband units. This solution was the property of Celfinet and was completely agnostic in terms of radio-access network hardware suppliers, being able to measure in multi-technology environments (Global System for Mobile Communications: GSM, Universal Mobile Telecommunications System: UMTS, and Long Term Evolution: LTE). Having a lean and simple architecture, it allowed the solution to meet most operators' demands. To measure power consumption, the equipment detected the current flowing through the feeding cable of each installed equipment in the base station, based on the Hall Effect [3]. As further discussed in the following sections, the model considered several inputs according to the technology and radio-frequency (RF) band, called features. The model used circuit-switched (CS) voice traffic and packet-switched (PS) data traffic, power, availability, and bandwidth as inputs. In the end, an enhanced broadcast control channel (BCCH) power consumption optimization feature was studied for GSM, in order to save energy and maintain performance.

1.2 Related Work

Several studies were developed in this context. The energy-saving mode for the radio-access network was analyzed. This strategy consisted of switching off cells when traffic decreased, especially during the night period [4-6]. Other studies have relied on cooperation between base stations [7]: when a base station is disconnected, it releases the resources to neighboring cells, thus allowing the network to be efficiently extended. In order to understand how to optimize the power consumption, several energy-consumption models have been developed, and were described in [8-11]. It was verified that energy consumption depends heavily on the generation of traffic.

This paper is organized as follows. Section 2 presents the methodology for building the model. In Section 3, a characterization of the base station and associated use case is made. Moreover, the traffic pattern and energy-consumption monitoring are also shown. In Section 4, the proposed energy-consumption model for all technologies is presented. Finally, Section 5 summarizes the main conclusions.

2. Methodology

Given a set of network traffic and power observations spread across time in equally distant intervals (e.g., 15 minutes), it is possible to build a model to predict the power consumption as a function of several features concerning data traffic. The sequence of traffic and power samples can be seen as a time series. Time-series data consist of a set of observations, $x(t)$, each observation being recorded at a specific time, *t*. First, a descriptive analysis of the time-series data was performed, considering some basic concepts such as the mean, the autocorrelation function (ACF), the partial autocorrelation function (PACF), and the definition of stationarity. In addition, the graphical representations of the series over time allowed us to identify some patterns in the data, such as the daily seasonality [12].

Considering the results of the previous descriptive analysis, a multiple linear regression model was used, taking the power as a dependent variable and the traffic, transmitted power, cell availability, time, and resource blocks as independent variables, according to each model [13].

There are three principal assumptions that must be verified when a linear regression model is used for purposes of inference and prediction [14].

- The linearity and additivity of the relationship between dependent and independent variables;
- The statistical independence of the residuals (in particular, no correlation between consecutive residuals in the case of time-series data);
- The residuals should be normally distributed, with zero mean and constant variance (homoscedasticity).

If any of these assumptions is violated, scientific insights yielded by a regression model may be inefficient, or seriously biased or misleading.

Nonlinearity is usually most evident in a plot of residuals as a function of predicted values. We hence considered applying a nonlinear transformation to the dependent and/or independent variables whenever it was appropriate. Violations of independence are potentially very serious in time-series regression models, given the existence of autocorrelation between consecutive residuals. In order to remove the autocorrelation between residuals, the data were reordered following a random-number generation process. Such a procedure allowed having samples without time dependence. To test for serial correlation of the residuals, the times series plot was observed and the Durbin-Watson test was used.

Sometimes, the error distribution is influenced by the presence of a few large outliers. Since parameter estimation is based on the minimization of the squared error, a few extreme observations can exert a disproportionate influence on parameter estimates. This factor causes violations of normality. To test the normality assumption, the normal probability plot of the residuals was used. If the distribution

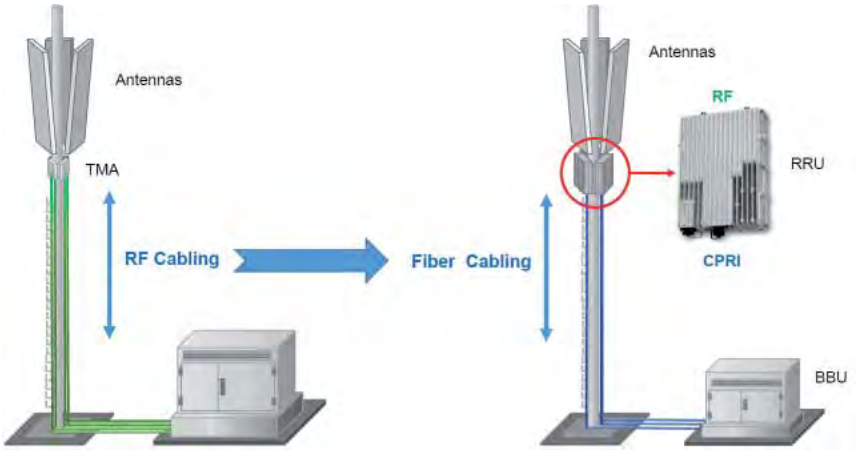

Figure 1. A distributed base station.

is normal, the points on such a plot should fall close to the diagonal reference line. In order to check the normality assumption, several tests were performed, such as the Shapiro-Wilk, Anderson Darling, and Jarque Bera tests. To minimize the potential consequences due to normality departures, an outliers identification process was also implemented, based on cook distance.

2.1 Validation Procedure

The data were divided into a training set and a test set. The training set was comprised of the first three weeks of the data (75%), and the test set comprised the last two weeks (25%).

After finding the appropriate model, it is important to determine if the model is actually fitted to the data. The errors of a fit are the difference between the observations and their model prediction (e_i), defined by

$$e_i = \hat{y}_i - y_r \tag{1}$$

Based on the calculation of the statistical errors, the mean-absolute-percent error is calculated by

$$MAPE = \frac{1}{n}\sum_{i=1}^{n} 100\left(\left|\frac{e_i}{y_i}\right|\right) \tag{2}$$

and the root-mean-square error is given by

$$RMSE = \sqrt{\frac{1}{n}\sum_{i=1}^{n} e_i^2}\ . \tag{3}$$

Additionally, as a measure of the linear association between the model's predictions and the real observations, the Pearson correlation coefficient was used. This indicator varies between -1 and 1. Absolute values close to one indicate a good fit.

3. System Characterization and Monitoring

3.1 Base Station Description

In a conventional radio-access-network base station, the radio equipment is located at the base of the tower, transmitting RF signals through coaxial cable to the tower-mounted amplifier (TMA), which is mounted as close as practical to the antenna at the top of the tower. Moreover, the current base stations have a distributed architecture in which the radio is divided into two main pieces of equipment: a baseband unit and a radio remote unit (RRU). The baseband unit is the unit that performs radio functions in the digital baseband domain. It can be installed in indoor or outdoor environments. This equipment uses common public radio interfaces (CPRI) and electrical or optical cables to communicate with the radio remote units. Additionally, the radio remote unit modulates and demodulates baseband and RF signals, combines and divides baseband and RF signals, and processes data. Radio remote units are installed near the antennas. Figure 1 illustrates an example of the distributed base station.

Normally, a base station has several transmission links (Tx) that allow the interconnection between the base station and the network controller, or between base stations (towards the core). This can be a radio link at the top of the tower, doing communication by microwaves or using optical fiber. Moreover, a rectifier is mounted at the base-station energy entrance, and this is responsible for the alternating current (ac) to direct current (dc) conversion.

Table 1. The base station characterization.

BS	Environment	RRU			
		GU900	U2100	L800	L1800
A	Industrial	X	X	–	X
B	Suburban	X	X	X	X
C	Suburban	X	X	X	X
D	Industrial	X	–	–	X
E	Urban	X	X	X	X
F	Rural	X	–	–	–

3.2 Use Case

The base station's energy monitoring is a very important step in fully understanding the management of modern telecommunications systems. In a first stage, it is important for the operator to measure and properly store the results of the measurements.

The current study was based on measurements from six base stations that could operate with three different radio-access technologies: GSM, UMTS, and LTE. Due to the fact that the radio equipment was shared in the 900 MHz band between GSM and UMTS, the monitoring equipment sensor, GU900, measured the amount of power associated with the two technologies.

The most common base-station configuration consists of three beam sectors. In each sector, one to four cells can be configured, a cell being indexed to a certain frequency. Figure 2 illustrates the association among cells, sectors, bands, and technologies.

Typically, the GSM technology has one transceiver (TRX) per sector, for signaling. This includes the enhanced broadcast control channel that carries only downlink information, and is responsible mainly for synchronization. This is the only channel type enabling point-to-multipoint communications, in which short messages are simultaneously transmitted to several mobiles. Each sector can also have one or more transceivers for the traffic channel (TCH), which is used to carry speech and data traffic. One carrier is attributed to each transceiver. In the case of UMTS, there are four carriers, one in the 900 MHz band and three in the 2100 MHz band. Finally, for LTE, there are two carriers in each sector, one in the 800 MHz band and the other in the 1800 MHz band.

For validation, four classes of environments were defined: rural, suburban, industrial, and urban, named from A to F. Moreover, Table 1 shows the technologies/bands for each base station.

The time series for traffic and consumed power were structured in 15-minute samples. There were therefore 96 samples per day.

Regarding the traffic in GSM, circuit-switched voice was analyzed (in Erlang), as was packet-switched data, presented in bytes/15-minute sample. In UMTS, besides circuit-switched transmission, the packet-switched transmission was divided into high speed downlink packet access (HSDPA) and Release 99 (R99) streams. For LTE, there was only data, since the transmission was performed only through packet-switched transmission.

For power-consumption data, the measured values for the radio remote units were accessed for each sector, and stored in watts. Additionally, measurements were made on other base-station components, namely the baseband unit and transmission.

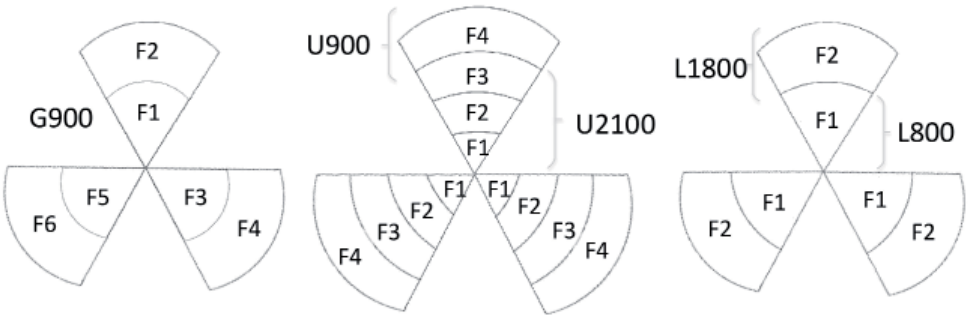

Figure 2. Cell distribution for each technology.

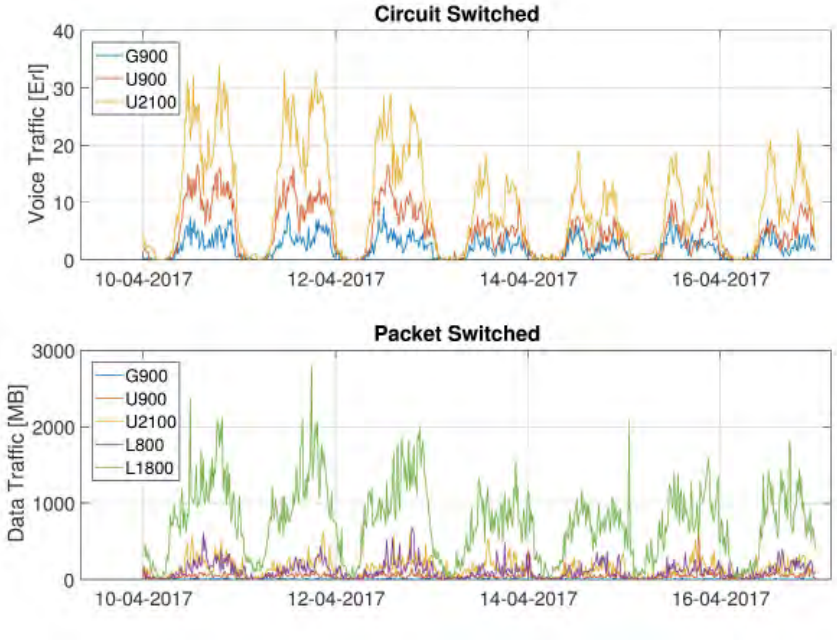

Figure 3. Traffic flow over a week for all technologies.

3.3 Traffic and Power Consumption Analysis

Figure 3 presents the traffic flow of voice and data over a week, for base station B (suburban). As expected, the traffic followed the working-week mobility pattern. It was possible to verify the low-traffic night periods, and also two peaks during the day: at lunch time and at the end of the working day.

The highest voice traffic was in the UMTS technology, as expected since it was the technology with the highest voice penetration. For the data traffic, LTE was the main service provider to users. This technology had the best data rates and bandwidth, guarantying the best quality of service for packet-switched transmission.

In order to analyze the power variation, Figure 4 presents the radio remote unit, baseband unit, and

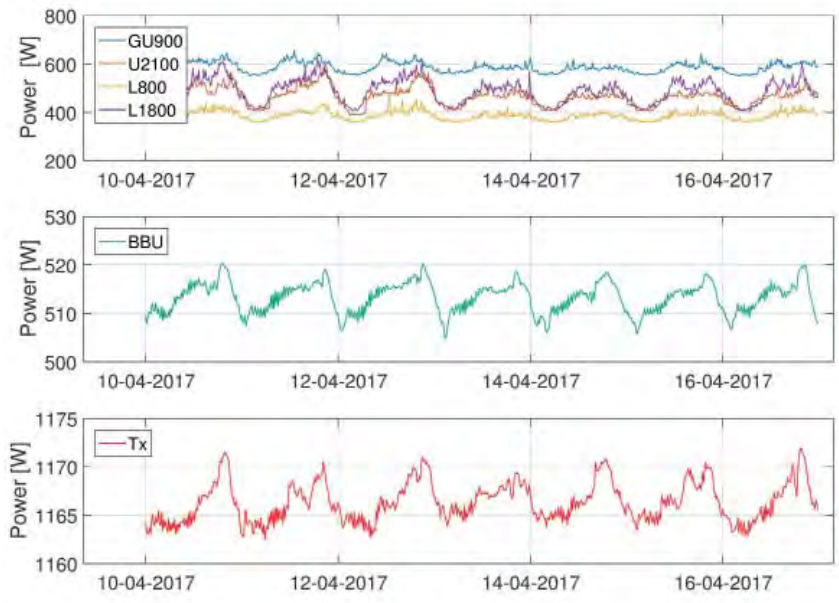

Figure 4. Radio remote unit (RRU), radio to baseband unit (BBU), and transmission links (Tx) power flow over a week.

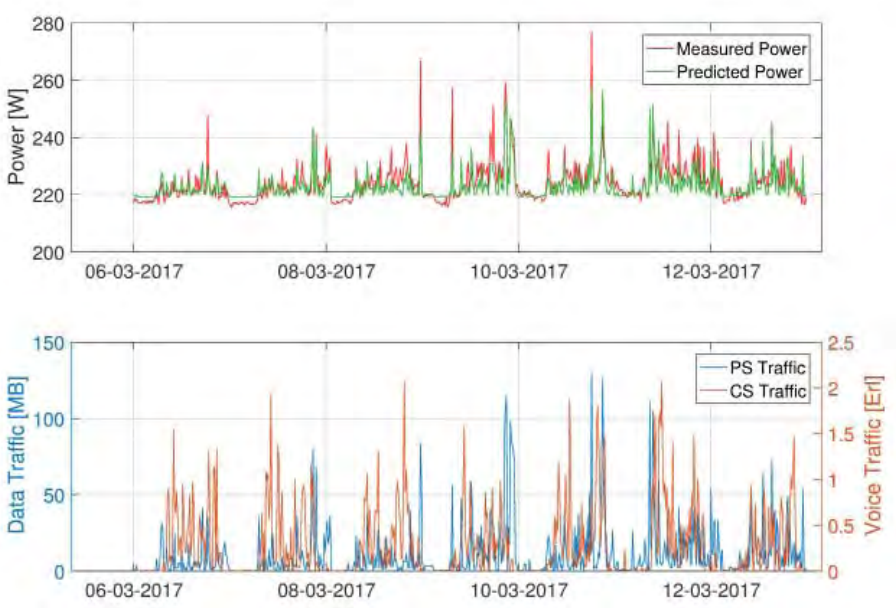

Figure 5. The application of the GU900 model.

transmission-link power flow over the same week and for the same base station.

Just by looking at Figures 3 and 4, the existence of a direct relationship between base-station-traffic load and power consumption could be noted.

4. Energy Consumption Model

Different tests using traffic and their respective energy consumptions for each technology were made, and a strong correlation was verified. This allowed concluding that traffic usage was a good starting point for building the models. Based on two weeks of data, three models were defined: GU900, U2100, and LTE, considering all base stations in Table 1.

The equations presented in this section correspond to the models developed, and the figures shown illustrate two charts. In the upper chart, the real power (the red curve) and the estimated power (the green curve) are presented. In the lower chart, the associated traffic can be analyzed.

Each model has its own independent variables that improve the results. For example, for the LTE model, the physical resource blocks (PRBs) were considered, because this is a specific characteristic of that technology related to user-resource allocation. The transmitted power was not considered in this model once it wasn't available. However, in another model iteration it will certainly be present in the equation. For the U2100 model, the time stamp (Hour) was considered as a variable. At night, the hardware switches-off some of the cells in this band in order to save energy, and the time information is useful to help the model to predict the energy consumption.

Note that for validation purposes, the training set was different from the test set.

4.1 GU900 Model Application

The GU900 model is given by Equation (4), which takes into account data ($T_{PS_{GSM}}$), voice ($T_{CS_{GSM}}$), enhanced broadcast control channel power consumption feature (F_{BCCH}), and the maximum transmission power (P_T) of both cells, GSM and UMTS. The model also considers the data ($T_{PS_{UMTS}}$) and voice ($T_{CS_{UMTS}}$) for UMTS.

$$P^t_{GU900} = \beta_0 + \beta_1 T_{PS_{GSM}} + \beta_2 T_{CS_{GSM}} + \beta_3 T_{PS_{UMTS}}$$

$$+\beta_4 T_{CS_{UMTS}} + \beta_5 F_{BCCH} + \beta_6 P_T \qquad (4)$$

In Figure 5, the measured and the predicted power are shown, along with the associated traffic, voice, and data of base station F, mentioned in Table 1. Figure 5 used a seven-day time window. In this experiment, the enhanced broadcast control channel feature [15] was deactivated, that is 0 dB. The radio remote unit radiated two carriers for GSM, with 20 W for both enhanced broadcast control channel and traffic channel frequencies. For the UMTS carrier, 46 dBm (about 39.8 W) was defined. The estimated power followed the progress of the measured power with a correlation of around 81.8%, with a prediction error of 1.21% (mean-absolute-percent error) and 4.05 W (root-mean-square error).

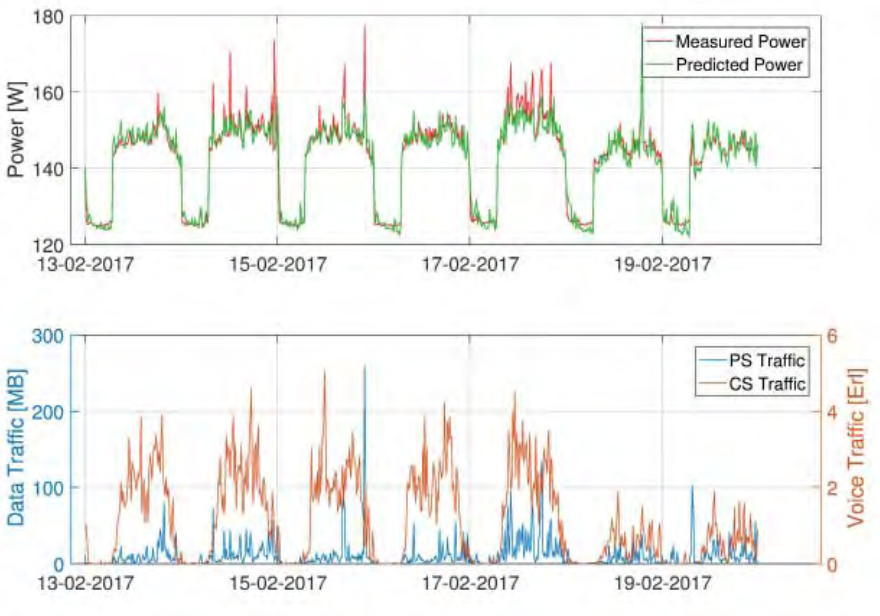

Figure 6. The application of the U2100 model.

The tests performed in all other sectors of the base station allowed identifying that the average error associated with this model was 3.99%.

4.2 U2100 Model Application

For UMTS in situations where there are several cells in the same sector, an algorithm was applied that allowed switching off certain carriers in the case of low traffic load, allowing an energy savings in that period of time, typically at night. This condition was verified in the 2100 MHz band of UMTS, which had up to three cells (carriers) per sector. On top of traffic, it was therefore possible to consider the number of active cells in order to know the real transmitted power. The U2100 model was given by Equation (5), and considers data (T_{PS} and T_{R99}), transmitted power (P_T), and hour (H).

$$P'_{U2100} = \beta_0 + \beta_1 T_{CS} + \beta_2 T_{PS} + \beta_3 P_T + \beta_4 H \quad . (5)$$

In Figure 6, the measured and the predicted power, and also the associated traffic, voice, and data of base station C are presented. Figure 6 relates to seven days. One active

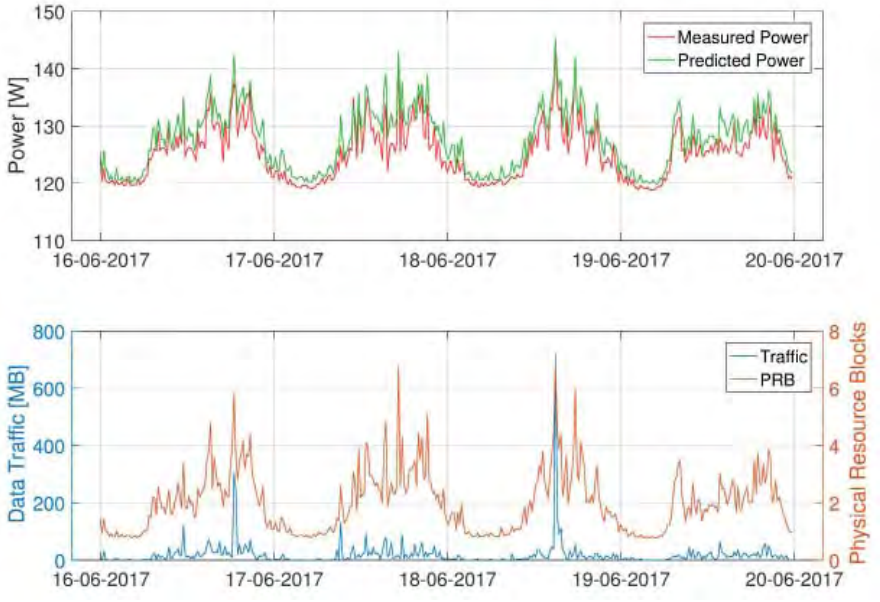

Figure 7. The application of the LTE model.

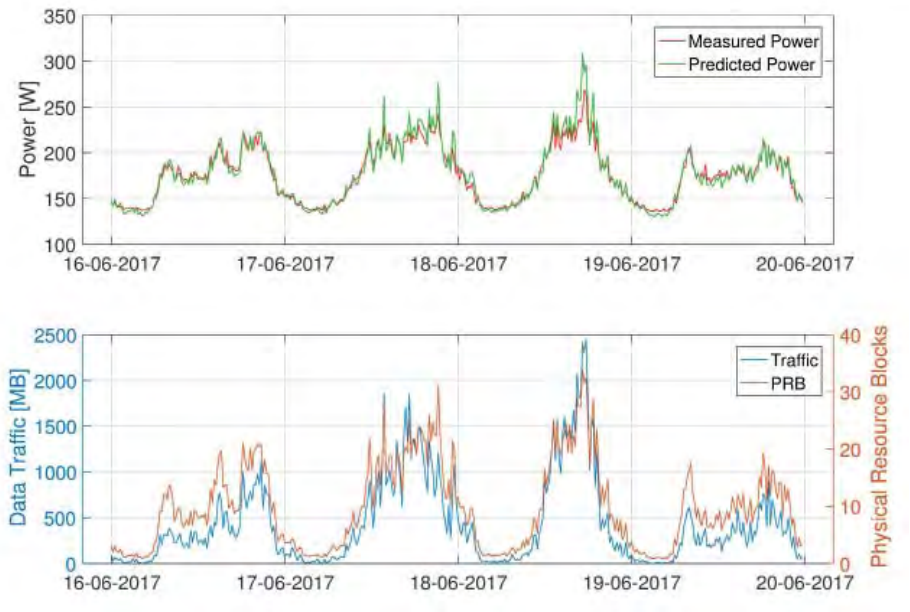

Figure 8. The application of the LTE model to the 1800 MHz band.

cell (carrier) was on between 0:00 and 7:00 a.m. The other two cells were switched off because of low traffic load. During this period, the maximum transmitted power was 44.2 dBm (26.3 W), corresponding to the F_1 carrier, as presented in Figure 2.

It was possible to conclude that the progress of measured and estimated power was similar, with a strong correlation of 97% and an error of only 1.2% (mean-absolute-percent error) and 2.73 W (root-mean-square error).

The tests performed on all other sectors of the remaining base stations allowed us to identify that the average error associated with this model was 2.2%.

4.3 LTE Model Application

For LTE, the physical resource blocks usage (N_{PRB}) was introduced, besides the traffic (T). In order to use the model for the two 800 MHz and 1800 MHz bands, the bandwidth (Bw) was subsequently added. The model is hence given by

$$P'_{LTE} = \beta_0 + \beta_1 T + \beta_2 N_{PRB} + \beta_3 Bw \,. \qquad (6)$$

The measured and predicted values were plotted for the 800 MHz and 1800 MHz bands, and are presented in Figures 7 and 8, respectively, for base station B. The configured bandwidths were 10 MHz and 20 MHz for the 800 MHz and 1800 MHz bands, respectively. The results showed that the model worked nicely for both bands, reaching predicted errors of 1.85% and 2.76% (mean-absolute-percent error), 2.77 W and 8.18 W (root-mean-square error), and correlations between 95.7% and 97.7%, for 800 MHz and 1800 MHz, respectively.

The test performed for all other sectors of the base stations allowed identifying that the average error associated with this model was 2.4%.

4.4 Energy Consumption Optimization

The RF module housing the enhanced broadcast control channel transceiver is one of the base-station components that consumes the most energy. The enhanced broadcast control channel power consumption optimization feature introduces a way to reduce power consumption by reducing the RF transmitted power on some time-division multiple-access (TDMA) timeslots carried in the enhanced broadcast control channel transceiver. With this feature, the transmitted power of non-enhanced broadcast control channel timeslots on the enhanced broadcast control channel transceiver can be decreased during off-peak hours.

It is important to include this vendor feature in the GU900 model given by Equation (4), since this configuration for the transmitted power will increase or decrease the radio equipment's power consumption. With F_{BCCH} , the model can thus statistically explain the different configuration values of this feature for the radio energy consumption.

This feature allowed a 10.1% reduction in energy consumption by a 3 dB decrease in GSM radio transmitted power. It was activated on Thursday afternoon, about 7:00 p.m. The traffic pattern on Friday remained constant, not changing after feature activation. On the weekend, the

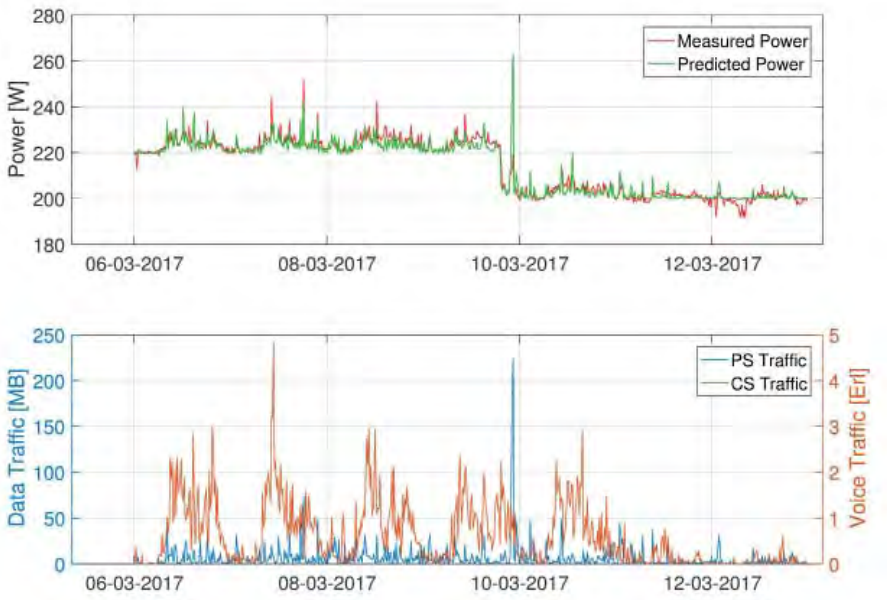

Figure 9. Activation of the enhanced broadcast control channel (BCCH) power consumption feature.

traffic decreased normally, and it was not caused by the power reduction feature. After this verification, the feature was applied to a cluster of 40 cells surrounding base station A and its neighboring cells.

In Figure 9, the impact of the feature's activation can be analyzed (for base station A). In order to analyze the network performance after this change, the call drop rate, key performance indicators (KPI) for GSM were analyzed (see Figure 10). No impact was observed in the key performance indicators after applying this feature, which was activated on March 21 (blue line). Before the feature activation, the call drop rate was 0.57%, and after activation it was 0.49%. In conclusion, it was possible to save energy, maintaining the call drop rate performance.

5. Conclusions

This paper has presented recent research results on the development of a novel power-consumption model for radio base stations using real measurements. Three different approaches for energy consumption were developed, corresponding to current GSM, UMTS, and LTE technologies. A high dependency was verified between the generated traffic and the power consumption along with the transmission power and the cell availability.

For LTE, the main impact factor for power consumption was the usage of physical resource blocks. The progress of predicted power followed the progress of

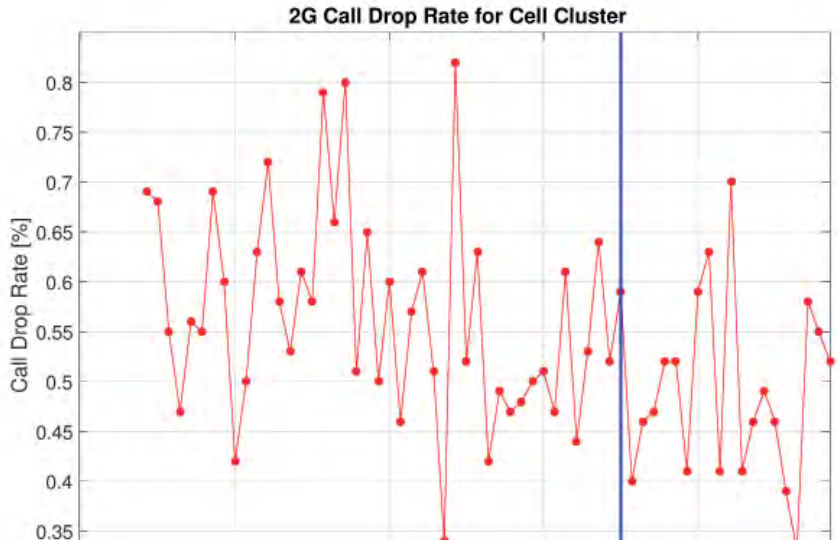

Figure 10. The global 2G call drop rate for cell cluster.

measured power, thus obtaining correlations of 80% to 97% for all technologies. GU900 and U2010 models were the worse and best models, respectively, with average errors of 7.7% and 3.5%.

Finally, the activation of the enhanced broadcast control channel power consumption optimization feature was studied and tested. Using this feature, 10% energy savings were reached in the GU900 radio remote unit while keeping the call dropped rate, and hence not degrading performance.

6. Acknowledgments

The authors would like to thank FCT for the support by the project UID/EEA/50008/2013. Moreover, we acknowledge project MESMOQoE (n 023110 - 16/SI/2016) supported by Norte Portugal Regional Operational Programme (NORTE 2020), under the PORTUGAL 2020 Partnership Agreement, through the European Regional Development Fund (ERDF).

7. References

1. G. Fettweis, and E. Zimmerman, "ICT Energy Consumption – Trends and Challenges," 11th International Symposium on Wireless Personal Multimedia Communications, 2008.

2. Huawei, "Save Energy and Reduce Emissions to Achieve Sustainable Development and Improve Corporate Competitiveness," whitepaper for Saving Energy and Reducing Emissions, 2012.

3. CELFINET, "RAN Energy Optimizer, Product Description," 2016.

4. C. Lubritto et al., "Telecommunication Power Systems: Energy Saving, Renewable Sources and Environmental Monitoring," INTELEC 2008, IEEE 30th International Telecommunications Energy Conference, San Diego, 2008, pp. 1-4.

5. T. Cunha et al., "Energy Savings in 3G Using Dynamic Spectrum Access and Base Station Sleep Modes," 1st URSI Atlantic Radio Science Conference (URSI AT-RASC), Las Palmas, 2015, pp. 1-1.

6. J. Wu, Y. Zhang, M. Zukerman and E. K. N. Yung, "Energy-Efficient Base-Stations Sleep-Mode Techniques in Green Cellular Networks: A Survey," *IEEE Communications Surveys & Tutorials*, 2015, pp. 803-826.

7. F. Han et al., "Energy-Efficient Cellular Network Operation Via Base Station Cooperation," 2012 IEEE International Conference on Communications (ICC), Ottawa, ON, 2012, pp. 4374-4378.

8. A. Spagnuolo, A. Petraglia, C. Vetromile, R. Formosi, and C. Lubritto, "Monitoring and Optimization of Energy Consumption of Base Transceiver Stations," *Energy*, **81**, March 2015, pp. 286-2931.

9. Ma. Dahal J. Shrestha and S. Shakya, "Power Consumption Modeling of Base Station as per Traffic Generated," *South American Journal of Academic Research*, May 2016.

10. D. Gadze, S. Aboagye, and K. Agyekum, "Real Time Traffic Base Station Power Consumption Model for Telcos in Ghana," *International Journal of Computer Science and Telecommunications*, **7**, 5, July 2016.

11. J. Lorincz, T. Garma, and G. Petrovic, "Measurements and Modeling of Base Station Power Consumption under Real Traffic Loads," *Sensors*, 2012.

12. M. Monteiro, "Forecasting Traffic and Balancing Load for Quality Driven LTE Networks," Instituto Superior Tcnico, 2016.

13. D. Montgomery and G. Runger, *Applied Statistics and Probability for Engineers*, New York, John Wiley and Sons, 2003.

14. R. Nau, *Statistical Forecasting: Notes on Regression and Time Series Analysis*, Fuqua School of Business, Duke University, Durham, 2016, http://people.duke.edu/rnau/411home.htm 15.

15. Huawei, "Enhanced BCCH Power Consumption Optimization Feature Parameter Description," Huawei Technologies Co., Ltd., 2014.

Bio-Radar Performance Evaluation for Different Antenna Designs

Carolina Gouveia[1], Daniel Malafaia[1], José N. Vieira[1,2], and Pedro Pinho[1,3]

[1]IT - Instituto de Telecomunicações
Campus Universitário de Santiago
Aveiro, Portugal

[2]IEETA - Instituto de Engenharia Electrónica e Telemática de Aveiro
Campus Universitário de Santiago
Aveiro, Portugal

[3]ISEL - Instituto Superior de Engenharia de Lisboa R. Conselheiro Emídio Navarro 1
Lisboa, Portugal

E-mails: carolina.gouveia@ua.pt, danielmalafaia@ua.pt, jnvieira@ua.pt, ppinho@deetc.isel.pt

Abstract

Cardiopulmonary monitoring without any physical contact with the human body has several applications, such as health monitoring of bedridden patients, monitoring sleeping, or even for rescuing people from collapsed buildings. The Bio-Radar system can accurately measure vital signals by using the principle of the Doppler effect, which relates the properties of the received signal to the distance change between the radar antennas and the person's chest wall. In this paper, a mathematical model of the Bio-Radar is presented. The algorithm used for extracting breathing rate is explained, and an analysis of the influence of the radiation pattern of the antenna on the quality of the received signal is presented. Moreover, we show that an antenna with a narrow beam leads to a better signal-to-noise ratio (SNR). The full performance of the developed prototype was also evaluated by using a certified measuring system to monitor vital signals simultaneously with the Bio-Radar. The signals extracted using both acquisition methods are presented, and a comparison is made in order to prove the accuracy of the prototype.

1. Introduction

Sensor-less measurement of bio-signals has the potential to improve many areas. Among many other applications in the medical field, the continuous monitoring of vital signals in bedridden patients can be highlighted, such as in a burn unit, where physical contact with the patient is discouraged. Other applications include monitoring sleep, to support cases of Obstructive Sleep Apnea Syndrome without interfering with the normal lifestyle of the patients, or in the prevention of Sudden Infant Death Syndrome [1]. In terms of commercial applications, driver monitoring can be highlighted, where the driver's vital signals are monitored to avoid any possible accident in case of cardiac failure. Applications in psychology are also possible, such as, for example, the measurement of stress response [2].

The Bio-Radar system is composed of a continuous-wave Doppler radar that continuously transmits a sinusoidal carrier, generated digitally, and receives the echo from the reflecting target. Due to the Doppler effect, there is a phase change as the subject's chest wall moves towards or away

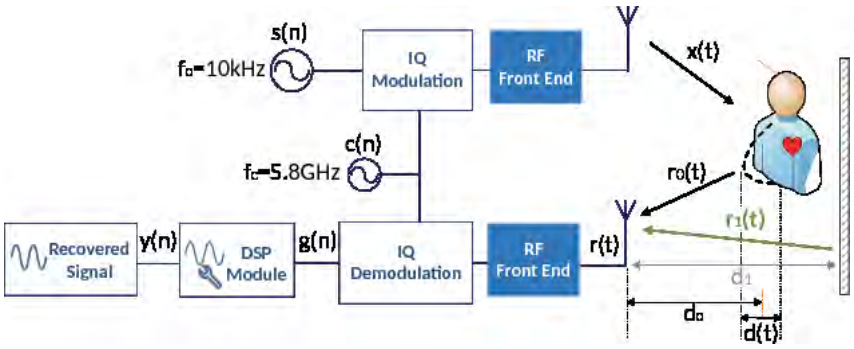

Figure 1. The block diagram of the Bio-Radar system

from the radar, and hence a phase modulation in the received signal is created [3]. The overall system is represented by the block diagram in Figure 1.

The concept of non-contact signal extraction of human physiological parameters was demonstrated by pioneers during the 1970s, where both respiration and heartbeat were separately measured during apnea interspersed periods [4]. Later, between the 1980s and 1990s, this system was implemented using analog and digital signal processing. The state-of-the-art of these systems thus followed a timeline of hardware implementation. The first proposed prototypes were implemented with transceivers composed of single radio-frequency (RF) hardware components interconnected with each other [5]. Later, the RF front-end components were integrated into a single chip using CMOS processes [6]. Nowadays, research in this area is even more focused on the development of systems with features that guarantee low power, small dimensions, better accuracy, long-range detection, and more robust operation. With this in mind, in [7] a bio-radar implementation was proposed using a front-end based on a software-defined radio (SDR) system. These radars allow the digital configuration of the inputs and outputs (receiver and transmitter) with respect to the required frequency and sampling rate of the current application. These configurable systems present an advantage compared to the previously referred-to systems, due to their flexibility and compactness.

Considering the work developed until recent times, the Bio-Radar prototype developed for this work has a front-end based on a software-defined radio and operates in real time, using the *LabVIEW* software. In this way, the acquired signals can be processed and visualized during their acquisition time. In this paper, a mathematical model that synthesizes the Bio-Radar system's behavior is also presented. Bio-signals have low amplitudes, and the modulation that they create on the radar's transmitted signal in baseband will be very close to dc. They hence are highly sensitive to several sources of noise, such as reflections from surrounding objects. The antenna design should therefore guarantee maximum directivity and a narrow beamwidth to focus exclusively on the human chest wall, and to thus avoid the reception of undesired reflections. Experiments were conducted using two antennas with different designs and different carriers. The dc component present in the signal was computed for each experiment, in order to evaluate the impact of the antenna's design on the received signal. Finally, the performance of the proposed Bio-Radar prototype was evaluated by measuring the vital signals of a subject simultaneously with a certified measuring system, called BioPac.

This paper is organized as follows. In the next section, we will start by presenting a mathematical model for the Bio-Radar system. In Section 2.2, we present a description of the extraction of the breathing signal. In Section 3, we present the implementation of the system and some real measurements obtained by the software-defined-radio-based test bed. The main conclusions are finally presented. All the tests conducted were focused on the acquisition of the respiratory signals.

2. Modeling the Bio-Radar System

2.1 Signal Model for the Bio-Radar Channel Response

Regarding the block diagram presented in Figure 1, a baseband signal is digitally generated with a sampling rate f_s. The signal is a complex sinusoid, with frequency ω_0 and amplitude A, and it is represented by

$$s(n) = Ae^{j\omega_0 n}. \tag{1}$$

The signal $s(n)$ is then modulated with in-phase and quadrature (IQ) modulations, with a carrier frequency ω_c This leads to the signal given by Equation (2), which is transmitted towards the target:

$$x(t) = A\cos\left[(\omega_0 + \omega_c)t\right]. \tag{2}$$

The received signal encompasses the time-variant signal $r_0(t)$, corresponding to the chest-wall reflection and the stationary signal, $r_1(t)$, which represents the sum of the total contributions of the reflections from static objects (clutter). The total signal at the receiver's input can be expressed as

$$r(t) = r_0(t) + r_1(t) \tag{3}$$

$$= A_0\cos\left[(\omega_0 + \omega_c)t + \varphi(t)\right] + A_1\cos\left[(\omega_0 + \omega_c)t + \theta_1\right]$$

where A_0 and A_1 are the amplitudes of the received signal from the subject and the clutter, respectively; $\varphi(t)$ is the phase-change function, which contains the respiratory information; and θ_1 is the phase change due to clutter. After its reception, the signal $r(t)$ is IQ demodulated, resulting in Equation (4), and is sampled at the same sampling rate, f_s, as in the transmission channel:

$$g(n) = A_0 e^{j\varphi(n)} + A_1 e^{j\theta_1}, \tag{4}$$

where θ_1 can be expressed as $\theta_1 = 4\pi d_1/\lambda$, considering that the clutter source is located at an equivalent distance d_1 from the radar, and λ is the wavelength.

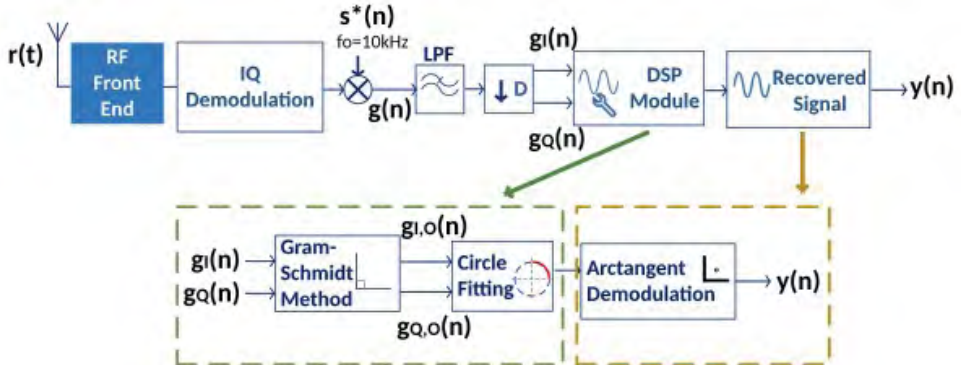

Figure 2. The receiver channel showing the DSP algorithm implementation.

The phase-change function, $\varphi(n)$, results from the chest-wall motion, which changes the distance the wave travels and hence modulates the reflected signal. The phase-change function can this be described by

$$\varphi(n) = \theta_0 + \frac{4\pi d(n)}{\lambda}, \qquad (5)$$

where θ_0 is the phase corresponding to the total path traveled by the wave. This can be expressed as $\theta_0 = (4\pi d_0/\lambda) + \phi$, where d_0 is the nominal distance between the radar and the target, and ϕ is the phase change at the surface of the target. In [8], it was shown that the respiratory signal should be modeled as a half cycle of a sinusoid raised to the *p*th power. However, in the remainder of this work a simpler model is considered, in which the chest movement is described as $d(n) = a_r \cos(2\pi f_1 n)$, where a_r is the amplitude of the chest movement and f_1 is the breathing rate.

2.2 The Extraction Algorithm for the Breathing Signal

Once at baseband, the complex signal $g(n)$ is then processed by the digital signal processing (DSP) algorithm, represented by the block diagram in Figure 2.

The signal $g(n)$ is down-sampled once it is a narrowband low-pass signal, and thus high sampling rates are not needed. The new sampling rate is f_{s2}. For the case of this work, the sampling rates were defined as $f_s = 100$ kHz and $f_{s2} = 100$ Hz.

The phase variation due to the target's motion is represented in the polar plot by an arc (Figure 3a), where the length of the arc is proportional to the amplitude of the respiratory signal, a_r, and the radius of the arc is the received signal's amplitude, A_0.

In an ideal scenario, the arc would fit to a perfect circle centered at zero. However, in real-world scenarios, there is an IQ imbalance effect. This occurs when both the real and imaginary parts do not have the same amplitude, and the phase relationship is not exactly 90°. The arc formed hence becomes an ellipse instead of a circle (Figure 3b). There are also dc offsets present in both the real and imaginary parts of the baseband signal caused by the clutter, which lead to an offset in the arc's center. Figure 3c shows the arc formed with the IQ imbalance effect and the dc offset. These effects should be digitally removed before the phase demodulation in order to guarantee an accurate arctangent result.

The IQ imbalance can be removed by using the Gram-Schmidt method [3, 4] by applying Equation (6),

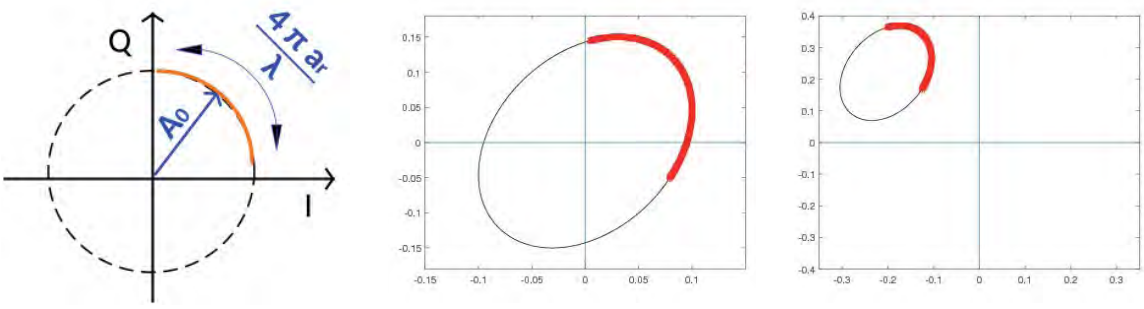

Figure 3. Complex plots of the baseband signal, $g(n)$, due to the target's motion: (a) in an ideal scenario, (b) with the IQ imbalance effect, (c) with a dc offset and the IQ imbalance effect.

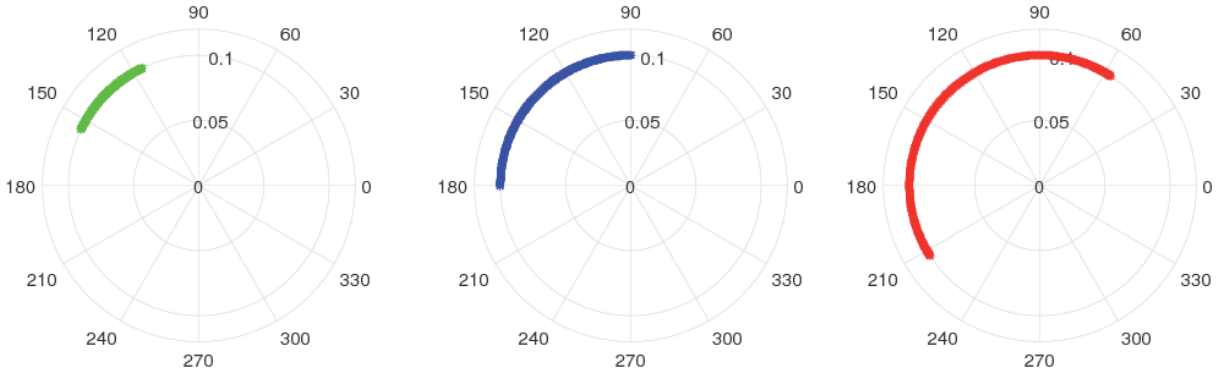

Figure 4. The influence of the carrier frequency, f_c, considering the amplitude of the motion to be $a_r = 0.00325$ for: (a) $f_c = 5.8$ GHz, (b) $f_c = 2.5$ GHz, (c) $f_c = 10$ GHz.

which restores the orthogonality of the baseband signal in quadrature:

$$\begin{bmatrix} g_{I,O}(n) \\ g_{Q,O}(n) \end{bmatrix} = \begin{bmatrix} 1 & 0 \\ -\tan(\psi_E) & \dfrac{1}{A_e \cos(\psi_E)} \end{bmatrix} \begin{bmatrix} g_I(n) \\ g_Q(n) \end{bmatrix} \quad (6)$$

The parameters ψ_E and A_e are the measured phase and amplitude imbalances, respectively; $g_I(n)$ and $g_Q(n)$ are the in-phase and quadrature parts of the baseband signal; and finally, $g_{I,O}(n)$ and $g_{Q,O}(n)$ are the in-phase and quadrature parts with the orthogonality restored. After the imbalance compensation, the dc offsets are estimated and removed using the circle-fitting method [9], which tracks the coordinates of the circle's center, and subtracts them from the complex signal, forcing the arc to be centered at zero. Finally, the arctangent is evaluated in order to extract the respiratory signal [3, 9], obtaining the signal, $y(n)$. From this signal, the respiration rate can be obtained by performing a power-spectrum analysis.

2.3 Carrier Wavelength Impact

The impact of the wavelength was simulated in *MATLAB* and is shown in Figure 4. Different carrier frequencies were used, revealing differences in the arc length.

In [8], it was concluded that the arc length is directly related to the phase modulation. It can be quantified in radians by Equation (7), and the SNR is dependent on the carrier wavelength. Carriers with a higher wavelength thus lead to low SNR, and vice-versa.

$$\Delta\phi = \frac{4\pi\varphi(n)}{\lambda}. \quad (7)$$

Besides the increasing SNR, other advantages in the usage of high frequencies have been identified, for instance, the possibility of using more-compact and portable radar modules, because smaller size antennas can produce the same gain and directivity using higher frequencies. High frequencies also maintain full beam radiating properties for longer distances, and increase the radar cross section of the area of the vital signals [1]. In [10], a study of the optimum carrier frequency in the framework of the detection of bio-signals was made, where the advantages of using the Ka-band were pointed out. Nonetheless, a balance should be reached regarding the increase in frequency. Higher frequencies lead to smaller wavelengths, which eases the detection of signals with low amplitude, such as

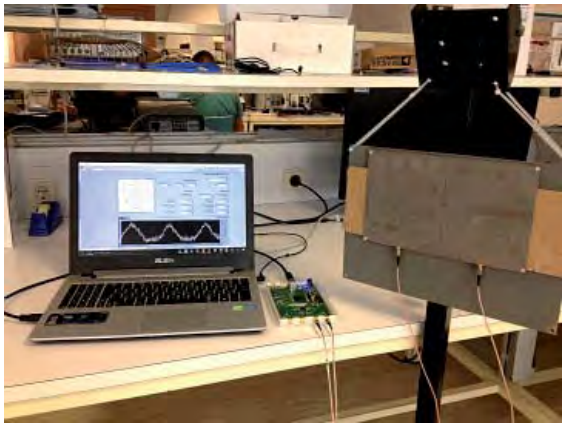

Figure 5. The Bio-Radar prototype, using 5.8 GHz antennas.

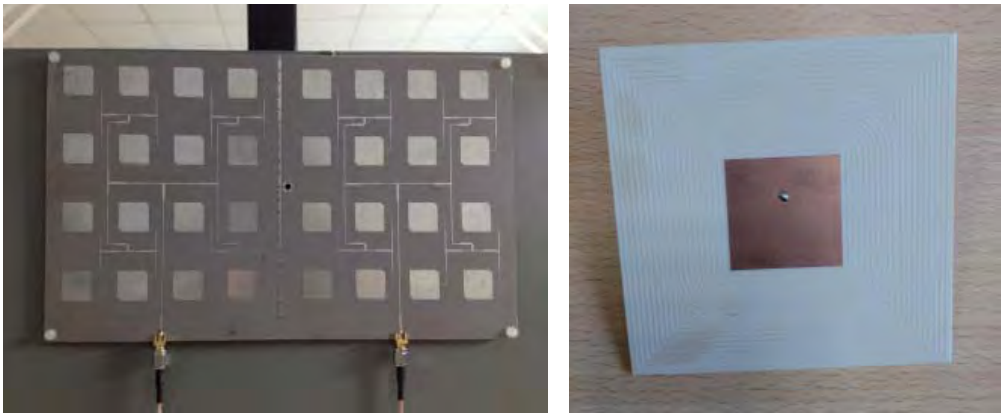

Figure 6. (a) Antenna 1: a 4×4 array of patch antennas at 5.8 GHz, (b) Antenna 2: a single patch of this linear array at 2.5 GHz.

the heartbeat signal. However, when small wavelengths are used, the respiratory signal, $d(n)$, is comparable with the wavelength, and a series of harmonic tones will be produced [1]. This effect can lead to intermodulation between the respiration signal and the heartbeat signal, and can hence hamper the simultaneous measurement of the respiration and heartbeat signals. Furthermore, with lower wavelengths, the arc length is larger, and hence it can easily achieve the full 2π phase rotation in the complex circle [3], causing multiple wraps in the extracted signal.

3. Implementation

The developed Bio-Radar prototype (Figure 5) consisted of a real-time measuring system implemented with the *LabVIEW* software. Signals were acquired using two antennas, one for transmission and the other for reception. The front-end was based on a software-defined radio system, which was a reconfigurable platform that established the connection of the front-end hardware and the DSP software. In the framework of this application, the software-defined radio used was an USRP B210. It digitally did the modulation and demodulation of the RF signals, giving more flexibility on the DSP side. The USRP B210 board operates over a limited range of carriers (70 MHz to 6 GHz). We therefore only used two frequencies: 2.5 GHz and 5.8 GHz.

The experiment conducted was divided into two parts. The goal of the first part was to compare the system's performance with two different types of antennas. Antenna 1 was a 4×4 antenna patch array tuned to a higher frequency, specifically 5.8 GHz. Antenna 2 was a single patch with a frequency of operation equal to 2.5 GHz (see Figure 6). The measured radiation patterns of the antennas are shown in Figure 7, and the magnitudes of the S_{11} values are in Figure 8.

In order to guarantee the same conditions for the experiments with both antennas, the chest-wall simulator (CWS) in Figure 9 was used to emulate the motion of the chest wall at a frequency of 0.4 Hz. For each antenna, the chest-wall simulator's motion was measured twice, at two different nominal distances, for $d_0 = 50$ cm and for $d_0 = 70$ cm. For each experiment, the dc component was measured by computing the absolute value of the signal's mean. The values obtained are discussed in the next section.

The second part of the conducted experiment aimed to validate the prototype's performance. For this purpose, certified measuring equipment, called a Biopac MP100, was

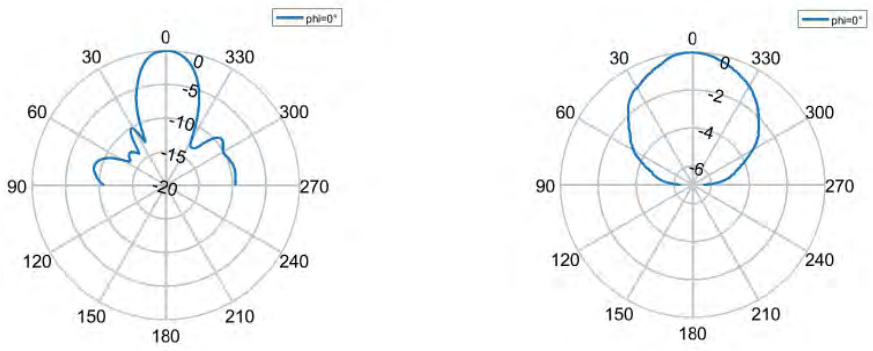

Figure 7. The radiation patterns of the antennas for phi = 0°: (a) antenna 1, (b) antenna 2.

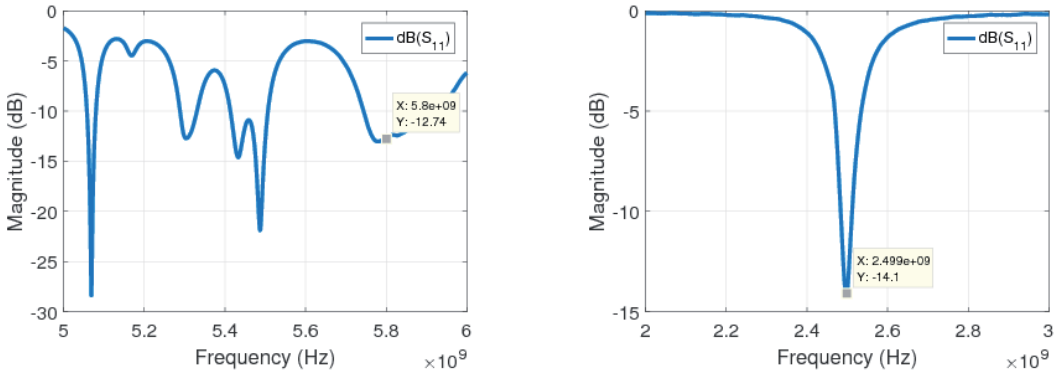

Figure 8. The S_{11} parameter values for (a) antenna 1, (b) antenna 2.

simultaneously used to monitor the vital signals with the Bio-Radar. The Biopac MP100 system was connected to an acquisition board that had several modules for different types of signal acquisition, such as ECG, breathing, and blood pressure. The RSP100C module was focused on the processing of data acquired from a respiration-transducer chest band, TSD201, placed around the chest cavity of the subject in the test. This transducer measured the respiratory effort by analyzing the instantaneous thoracic perimeter. The system set up is shown in Figure 10.

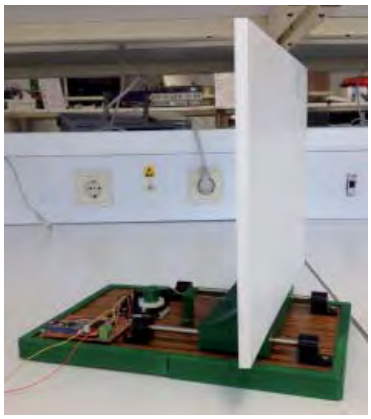

Figure 9. The chest-wall simulator.

A total of three tests were conducted in order to monitor the normal breathing of a healthy volunteer. The subject was seated in front of the Bio-Radar's antennas, with the chest band in place. The subject was asked to stay still while the BioPac and Bio-Radar continuously acquired data. Since it was extremely difficult to start both measuring systems at the same time, an initial breathing pattern (IBP) from the patient was needed as a trigger to establish the beginning of the measurement in order to sync the signals acquired by both the Biopac and the Bio-Radar. The initial breathing pattern was composed of three heavy breaths followed by an apnea period. Figure 11 shows an example of the resultant signal, with the initial breathing pattern and the rest of the measurement. In *MATLAB*, the samples acquired considered for processing were the samples collected during that measuring time (after the initial breathing pattern) labeled as "Normal Breathing" in Figure 11.

The results obtained are presented in the next section, where a comparison is made between the extracted signals acquired by the Bio-Radar and the Biopac.

Table 1. The dc values from the experimental tests.

	$d_0 = 50$ cm	$d_0 = 70$ cm
Antenna 1: 5.8 GHz	0.0115	0.0044
Antenna 2: 2.5 GHz	0.2330	0.2521

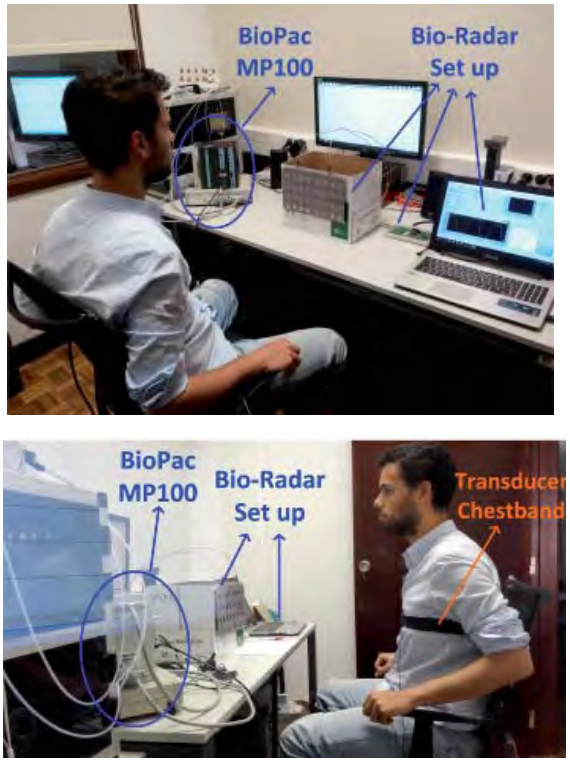

Figure 10. The setup for the conducted tests using the BioPac MP100 and the Bio-Radar: (a) a view of the workbench, (b) a view showing the subject wearing the transducer chest band.

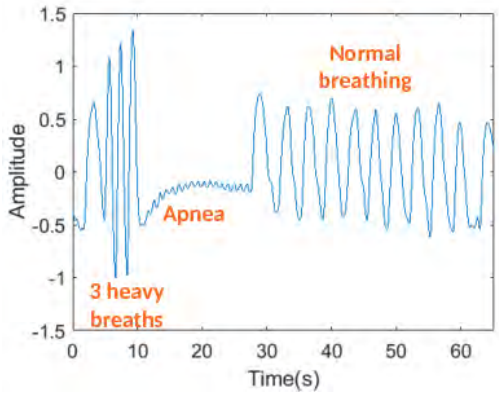

Figure 11. The Biopac signal showing the respiratory pattern (initial breathing pattern, IBP) used for the conducted experiment.

4. Discussion of Results

Regarding the implementation described in the previous section, the discussion of the results is divided in two sections: the influence of the design of the antennas, and the validation of the performance of the full prototype.

4.1 Impact of the Design of the Antennas

Considering the radiation patterns in Figure 7, the half-power beamwidth (HPBW) was computed for each radiation diagram in order to compare the directionality. Antenna 1 presented a half-power beamwidth of 30°, and the half-power beamwidth of antenna 2 was 115°. These results showed that the beam of antenna 1 focused in a specified area reducing the reception of clutter, in contrast with antenna 2, for which in this case more parasitic reflections would be received. This effect is represented by the vectorial diagram of Figure 12.

As previously mentioned, the clutter was perceived as a dc offset, present in both the real and imaginary parts of the signal. This effect was confirmed by the results of the experiments conducted, as presented in Table 1.

The results obtained showed that independently of the target's distance (near to or far from the antennas), antenna 1 presented a lower dc component. In contrast, antenna 2 presented a higher dc component at both testing distances.

Table 2. The respiratory rate for each test using both the Biopac and Bio-Radar, and the center coordinates of the arcs after dc-offset cancellation for the Bio-Radar case.

	Respiratory Rate [Breaths/min]		Arc Center Coordinates	
	Biopac	Bio-Radar	X_{dc}	Y_{dc}
Test 1	17.55	17.55	–4.1021e–18	3.6176e–18
Test 2	18.13	18.13	–2.4369e–17	3.0512e–17
Test 3	14.34	14.93	–1.9019e–18	–6.5228e–18

By implementing the DSP algorithm presented in Section 2.2, the target's motion could be extracted in each test performed, as shown in Figure 13. The signal extracted for antenna 2 had a high presence of noise. To the contrary, the signal from antenna 1 presented significantly less noise. The rate of motion was correctly obtained for both cases (Figure 14 presents the major spectral component at $f_1 = 0.3906$ Hz) regarding the motion frequency of the chest-wall simulator, previously mentioned as 0.4 Hz.

4.2 Bio-Radar Performance Evaluation Using Biopac

Considering the initial breathing pattern used to synchronize both respiratory signals acquired by Bio-Radar and Biopac, their rates were computed using the `pwelch` function from *MATLAB*, and the waveforms obtained were compared. The results are summarized in Table 2. The values of the arc's center coordinates after dc compensation are also presented, once we were dealing with real signals, and thus the DSP algorithm could be also validated.

Comparing the plotted signals from Figure 15, the Bio-Radar and Biopac signals almost totally matched during the proper respiration measurement (after the initial breathing pattern).

The Biopac signal presented a periodic signal with a constant trend, although the signal acquired from the Bio-Radar suffered from some distortion effects due its operating principle. For example, in Figure 15d, a noticeable effect could be observed. In this figure, the Bio-Radar signal

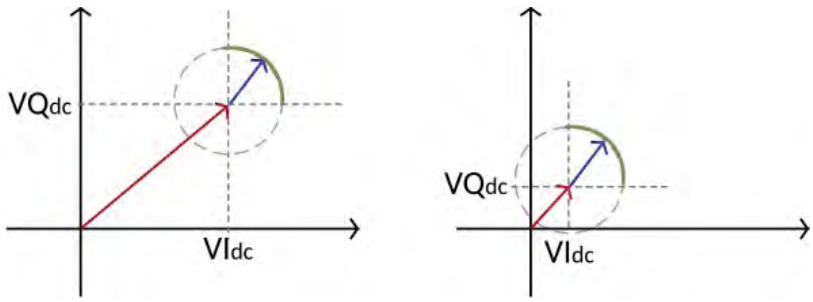

Figure 12. Vectorial diagrams representing the dc components, where the red arrow represents the dc component and the blue arrow represents the signal: (a) For case of non-directive antennas, the dc component is larger than in (b), where a directive antenna was used, and there was less clutter influence.

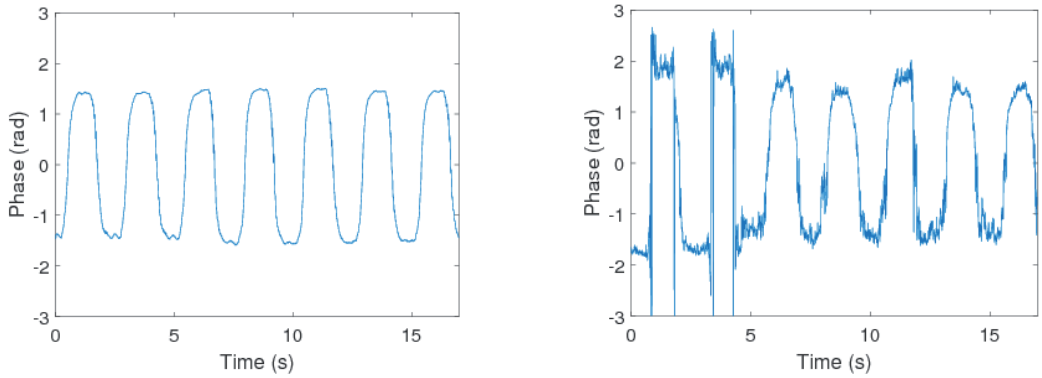

Figure 13. Extraction of the target's motion at a distance of $d_0 = 50$ cm: (a) for antenna 1, (b) for antenna 2.

had a slightly varying mean value. The occurrence of this effect was expected, because the patient did not maintain the same breathing rate and amp Figures 15a, 15c, and 15e represent the signals obtained during the full test, including the initial breathing pattern. The usage of the initial breathing pattern allow providing a visible trigger, and thus, after the apnea period, it was possible to shift the respiratory signal so that it could start at the same instance as the Biopac signal. In these latter figures it was also possible to verify the changed trend in the Bio-Radar signal.

Despite the small effects present in the Bio-Radar signal, it was possible to verify that its extracted signal matched with the Biopac signal.

5. Conclusion

In this work, a mathematical model of the Bio-Radar system was introduced, as well as the DSP algorithm needed for phase demodulation and respiratory signal extraction. The impacts of the design of the antennas and the carrier frequency were also studied. Experimental tests using the chest-wall simulator showed that directive antennas acquired better signals with small dc components and therefore less noise in the signal. However, the narrow beam of antenna 2 implied a better alignment between the antenna and the patient. Finally, the performance of the Bio-Radar in real time and its signal acquisition were validated using the Biopac MP100 measuring system. The Biopac kit acquired the respiratory signal using a transducer chest band located around the thorax of the patient. The signals extracted using both acquisition methods were presented, and a comparison of their computed average rate was made, as well. From the analysis of these, it was possible to conclude that no significant differences were detected, confirming that good performance of the prototype was achieved.

As future work, we intend to design a beamforming antenna with a tracking algorithm to maintain the alignment.

6. Acknowledgement

This work was supported by the European Regional Development Fund (FEDER), through the Competitiveness and Internationalization Operational Programme (COMPETE 2020) of the Portugal 2020 framework

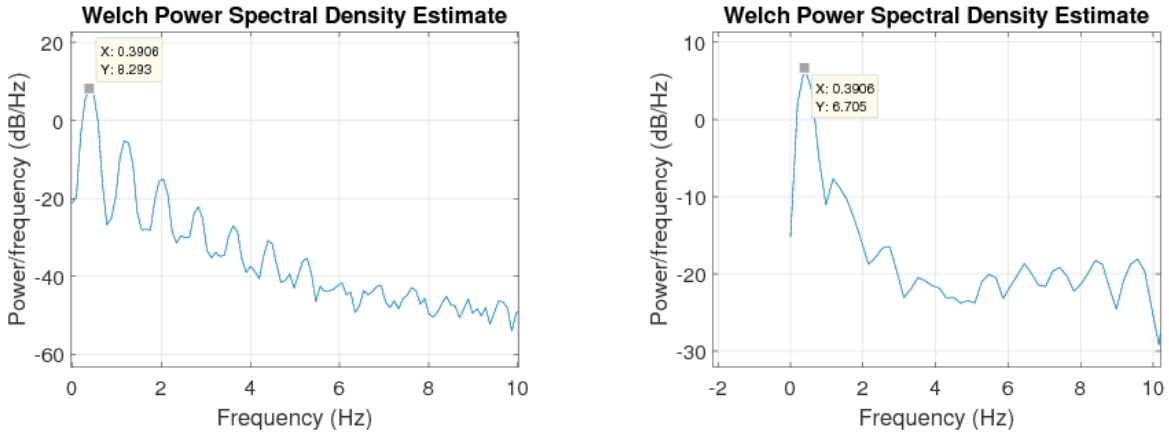

Figure 14. The power spectral density: (a) for antenna 1, (b) for antenna 2.

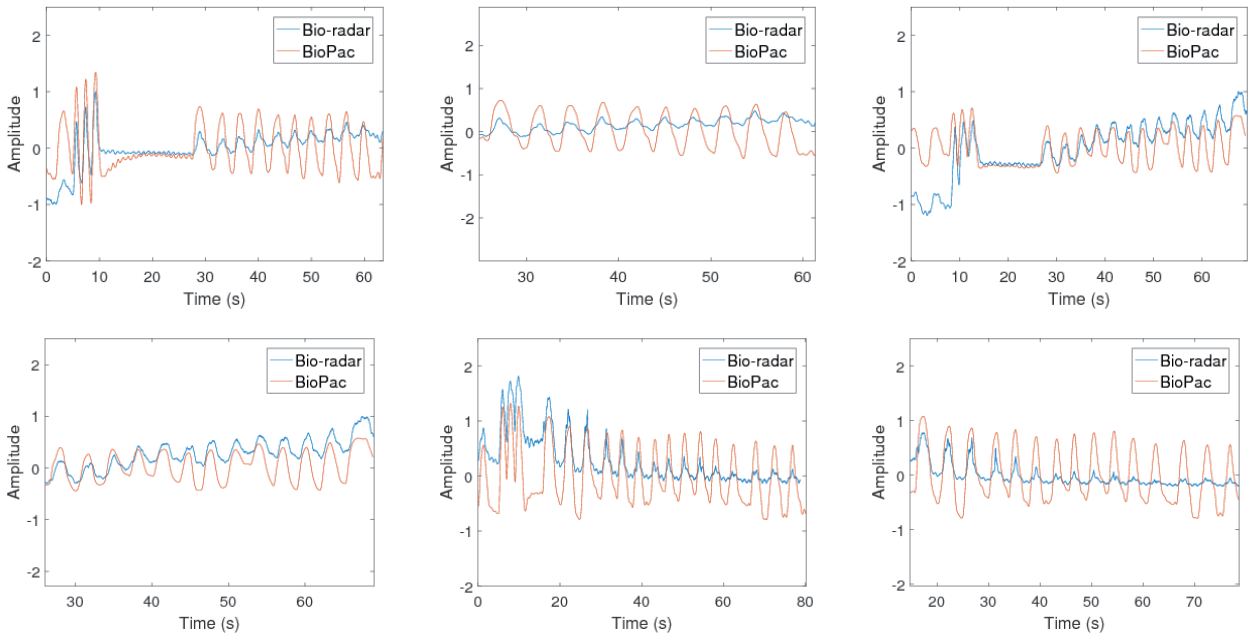

Figure 15. The extracted signal for (respectively) Test 1, Test 2, and Test 3: the signals for the full test are shown in 15a, 15c, and 15e; the extracted respiratory signals are shown in 15b, 15d, and 15f.

[Project TexBoost with Nr. 024523 (POCI-01-0247-FEDER-024523)].

7. References

1. C. Li, V. Lubecke, O. Boric-Lubecke, and J. Lin, "A Review on Recent Advances in Doppler Radar Sensors for Noncontact Healthcare Monitoring," *IEEE Transactions on Microwave Theory and Techniques*, **61**, 5, 2013, pp. 2046-2060.

2. D. Malafaia, et. al., "Cognitive Bio-Radar: The Natural Evolution of Bio-Signals Measurement," *Journal of Medical Systems*, **40**, 10, 2016, p. 219.

3. O. Boric-Lubecke, V. Lubecke, A. Droitcour, B. Park, and A. Singh, *Doppler Radar Physiological Sensing*, New York, John Wiley & Sons, 2015.

4. A. Droitcour, *Non-Contact Measurement of Heart and Respiration Rates with a Single Chip Microwave Doppler Radar*, Doctoral Dissertation, Stanford University, 2006.

5. P. Byung-Kwon, A. Vergara, O. Boric-Lubecke, V. M. Lubecke, and A. Høst-Madsen, "Quadrature Demodulation with DC Cancellation for a Doppler Radar Motion Detector," *IEEE Transactions on Microwave Theory and Techniques*, 2007.

6. C. Li, X. Yu, C. M. Lee, D. Li, L. Ran, and J. Lin, "High Sensitivity Software Configurable 5.8 GHz Radar Sensor Receiver Chip in 0.13 µm CMOS for Non-Contact Vital Sign Detection," *IEEE Transactions on Microwave Theory and Techniques*, **58**, 5, 2010, pp. 1410-1419.

7. D. Malafaia, J. Vieira, and A. Tomé, "Improving Performance of Bio-Radars for Remote Heartbeat and Breathing Detection by using Cyclostationary Features," Proceedings of the International Joint Conference on Biomedical Engineering Systems and Technologies, **4**, pp. 344-349.

8. M. Zakrzewski, H. Raittinen, and J. Vanhala, "Comparison of Center Estimation Algorithms for Heart and Respiration Monitoring with Microwave Doppler Radar," *IEEE Sensors Journal*, **12**, 3, 2012, pp. 627-634.

9. B. Park, V. Lubecke, O. Boric-Lubecke, and A. Høst-Madsen, "Center Tracking Quadrature Demodulation for a Doppler Radar Motion Detector," Microwave Symposium IEEE/MTT-S International, 2007, pp. 1323-1326.

10. C. Li and J. Lin, "Optimal Carrier Frequency of Non-Contact Vital Sign Detectors," IEEE Radio and Wireless Symposium, 2007, pp. 281-284.

Multi-Sine Channel Optimization for RF-to-dc Performance Characterization

Marina Jordão, Ricardo Correia, and Nuno Borges Carvalho

Instituto de Telecomunicações
Departamento de Eletrónica, Telecomunicações e Informática
Universidade de Aveiro
Aveiro 3810-193, Portugal

Abstract

The main objective of this work is to present a characterization system capable of generating different multi-sine signals to optimize the performance of RF-dc converters. The system allows the measurement in real time of the efficiency of the RF-dc converters, according to different multi-sine signals that are generated by using *LabVIEW*.

In Internet of Things (IoT) environments, wireless power transfer (WPT) assumes an important role, and RF-dc converters are one of the key technologies for this purpose. Consequently, it is very important to characterize and measure the wireless power transfer devices in order to enhance their behavior and also to improve their performance in 5G scenarios.

1. Introduction

At radio frequencies (RF), one of the big challenges is to optimize systems and devices in order to make them more efficient and to thus to increase their performance. The role of the measurement and characterization of systems is not only the validation and testing of devices, but also to find their faults for further improvement. Measurement techniques capable of identifying the failures of these systems are increasingly prominent in the RF field.

Nowadays, 5G, IoT, and wireless power transfer are hot topics in RF world. Developing efficient gadgets, mechanisms, widgets, and systems for these fields are some of the challenges that RF engineers face these days. Accordingly, RF engineers are increasingly developing wireless power transfer devices that can be used in the IoT field, and these devices are studied more and more. RF-dc converters are an example of devices used in wireless power transfer and IoT. In this way, RF-dc converters can increase their use and perform better in wireless power transfer, IoT, and 5G scenarios. For this reason, RF-dc converters need to be characterized in order to increase their efficiency and performance.

Studying ways to increase the efficiencies of these converters is therefore a necessity. Many studies [1-5] have indicated that one of the ways to improve the efficiency of RF-dc converters is to use multi-sine signals instead of continuous-wave (CW) signals. High peak-to-average power ratio (PAPR) waveforms are able to enhance the RF-dc conversion efficiency of energy-harvesting circuits, especially at low input power levels. This is due to their greater ability to overcome the built-in potential of the

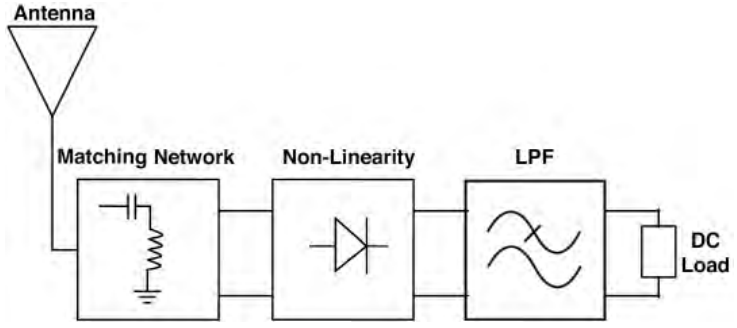

Figure 1. A block diagram of an RF-dc conversion circuit.

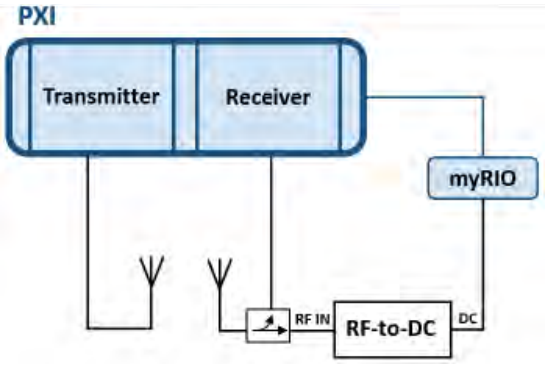

Figure 2. The system block diagram.

rectifying devices when compared to constant-envelope continuous waves. Since the diode has a threshold voltage, the multi-sines increase peak-to-average power ratio and, in this way, the RF-dc converters present more efficiency when compared with a traditional continuous wave.

Due to this fact, a system capable of measuring the efficiency of RF-dc converters that allows the possibility of configuring the number of multi-sine signals generated in real time using *LabVIEW* is proposed.

2. RF-to-dc Converters and the Multi-Sine Role

Figure 1 shows the block diagram of an RF-dc conversion circuit. These circuits are composed of an antenna, a matching network to enable the power transfer, a nonlinear device (a Schottky diode), a low-pass filter, and the resistive load.

In order to maximize the RF-dc conversion efficiency, circuit-level optimization is conventionally carried out. Alternatively, the RF-dc conversion efficiency can be boosted by selecting properly formatted waveforms, such as high peak-to-average-power-ratio in-phase multi-sine signals that are capable of efficiently surpassing the turn-on voltage of rectifying devices at low average power levels [6].

When all multi-sine signal components are aligned in phase and with the same levels of power, the device performance can be optimized [7]. The efficiency of the RF-dc converter between the transmission antenna and the receiving antenna can thus also be optimized. In this way, strategic analysis of the impact of multi-sine signals on the performance of RF-dc converters in real time, and considering the distance between transmitting and receiving antennas, are challenges from a scientific point of view.

3. System Characterization

It is intended to have a *LabVIEW* application that in real time performs the measurement of the efficiency of

Figure 3. The system setup at the laboratory.

the RF-dc converter, depending on the number of multi-sine signals that were generated. In addition, another objective is to vary the distance between the transmitting and receiving antennas to realize the impact of the distance on the performance of the RF-dc converter by varying the number of multi-sine signals.

The system furthermore aims to study the performance of the RF-dc converter at several frequencies and for different numbers of multi-sine signals. Consequently, a three-dimensional sweep system was developed, in order to provide the RF-dc performance information for these characterization parameters.

To characterize the RF-dc converter and to improve its performance, a characterization system was built using *LabVIEW* and using equipment from National Instruments (NI). Figure 2 shows the block diagram of the system. An RF transmitter (NI 5793) was used to generate the multi-sine signal, and an antenna was used to send the signal (TX antenna). To read the received signal, a receiving (RX) antenna was required, and a coupler was connected. The antennas used in this system were the 736624 Kathrein antennas, which work from 870 MHz to 960 MHz, with vertical polarization and with a gain of 7 dBi. The received signal was sent to the RF-dc converter and to the receiving antenna. To read the dc voltage from the RF-dc converter in real time, the NI myRIO-1900 was used. The system setup can be seen in Figure 3.

4. *LabVIEW* Application

A *LabVIEW* application was developed in order to implement the multi-sine channel optimization to characterize the RF-dc performance. The algorithm's application procedure is illustrated in Figure 4.

The system is first configured (frequencies, power, and devices). After this, the multi-sine signals can be configured according to the carrier spacing, phase spacing, and the number of multi-sine signals generated. The system aims to configure uniform multi-sine signals (in terms of power, phase, and frequency) and arbitrary spacing (in terms of phase and frequency), in order to study the best approach for improving the efficiency of each RF-dc converter.

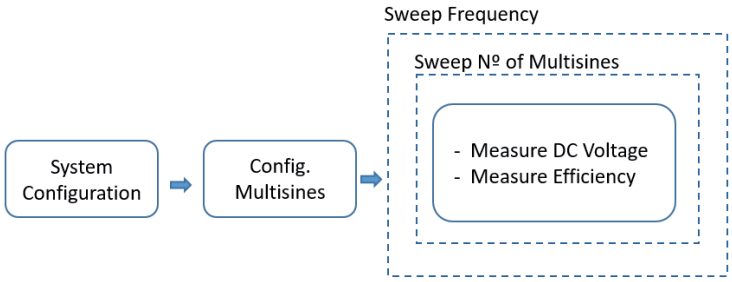

Figure 4. The application procedure.

The coupler port is then acquired by the receiver, which gives information about the multi-sine signals that are read in real time. The dc voltage of the device is thereafter read, and the efficiency is consequently calculated, using Equations (1) and (2) [8, 9]:

$$P_r = P_t G_t G_r \left(\frac{c/f}{4\pi d} \right)^2 , \qquad (1)$$

$$Eff\,(\%) = \frac{DC^2/R_L}{P_r} 100 , \qquad (2)$$

where P_r is the received power; P_t is the transmitted power; G_t and G_r are respectively the gains of the transmitting and receiving antennas (7 dBi); d is the distance between the antennas; f is the frequency; and c is the speed of light.

The front panel of the *LabVIEW* application can be seen in Figure 5. On the left side of the application can be seen the configuration of the devices, the power configuration, the chosen frequencies, the configuration of the multi-sine signals, and the distance between antennas. The measurement results are shown on the right side of the application. For each frequency measured, the number of multi-sine signals is swept and the efficiency results are shown on the graph. The table also shows the measured dc voltage and the respective efficiency for each number of multi-sine signals. In the end, a three-dimensional graph presents the measurement for each frequency, the number of multi-sine signals, and the efficiency.

5. Measurements

5.1 RF-dc Converter

To use this characterization platform, an RF-dc converter was designed to fit the specifications of the antennas. The converter used is shown in Figure 6, and the respectively simulated and measured S_{11} values can be seen in Figure 7. The major objective in this work was the optimization of the rectifier for a considerable bandwidth

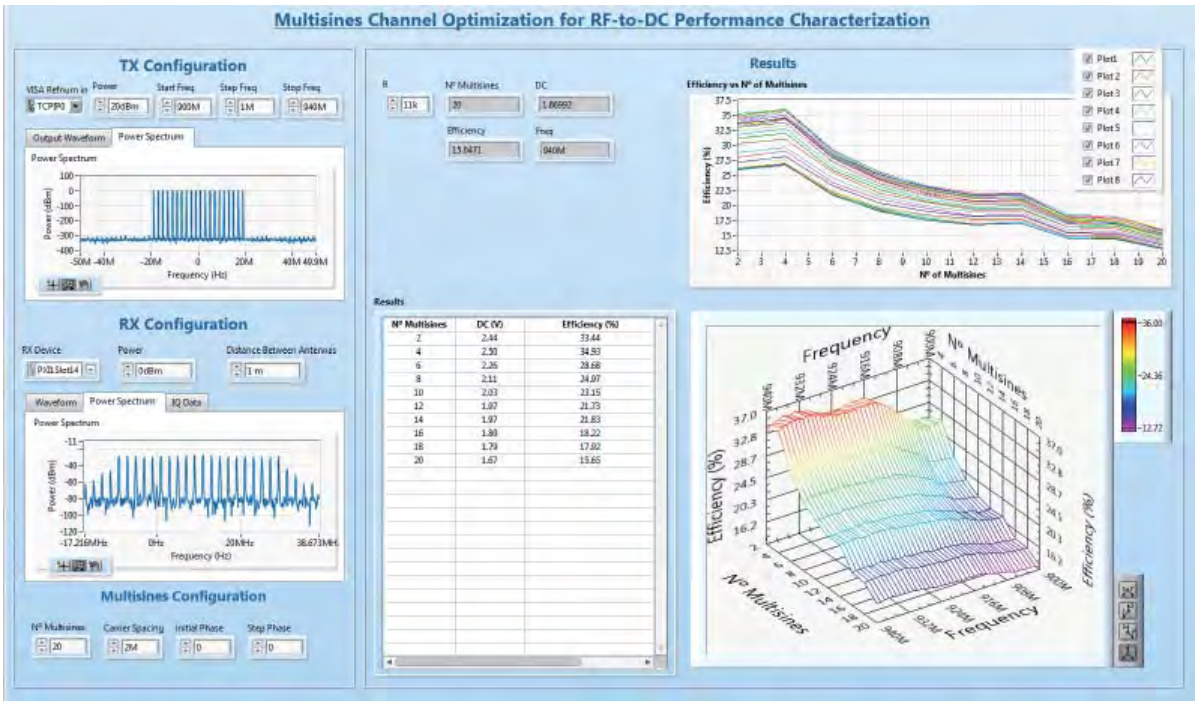

Figure 5. The *LabVIEW* application front panel.

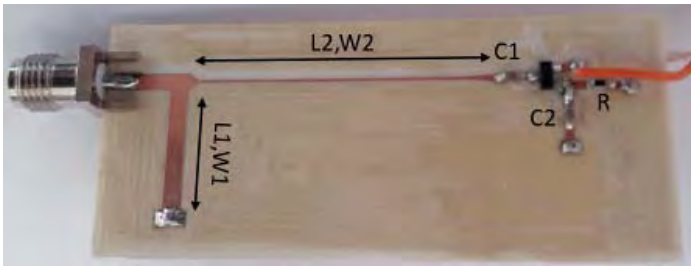

Figure 6. A photograph of the proposed RF-dc conversion circuit. The values were $L1 = 12.6$ mm, $W1 = 2$ mm, $L2 = 28$ mm, $W2 = 0.4$ mm, $C1 = 68$ pF, $C2 = 68$ pF, $R = 11$ kΩ. The substrate for the transmission lines was Astra MT77, with a thickness of 0.762 mm, $\varepsilon_r = 3.0$, $\tan\delta = 0.0017$.

to enable the possibility of performing the multi-sine characterization. Nevertheless, and due to the parasitic effects of the diode, the matched frequency suffered a shift that in no way compromised this work. Comparing the measured and simulated results, it could be seen that the rectifier was still optimized for the desired frequency (900 MHz).

As was mentioned in Section 2, the RF-dc converter is typically composed of an antenna, a matching network to allow maximum power transfer, a nonlinear rectifying device followed by a low-pass filter, and a dc load. In order to use a multi-sine signal at the input, the rectifier should have considerable bandwidth, as can be seen in Figure 7.

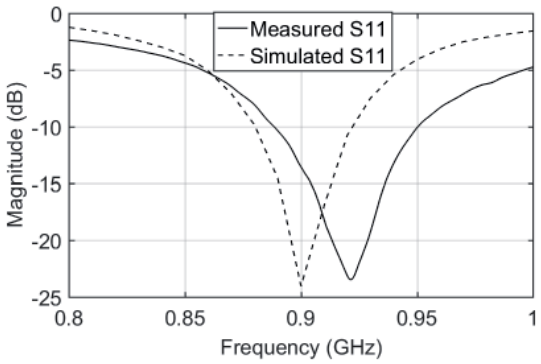

Figure 7. The measured and simulated S_{11} parameter values as a function of frequency.

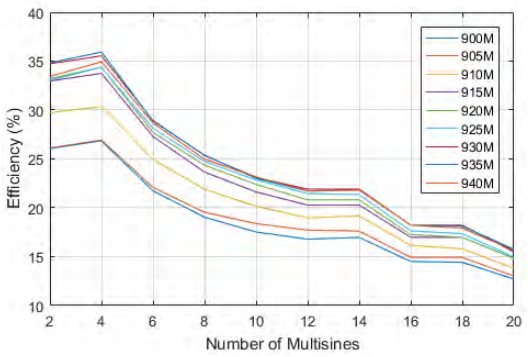

Figure 8. The RF-dc converter results for a distance of 1 m, with a transmitted power of 20 dBm and 2 MHz between multi-sines.

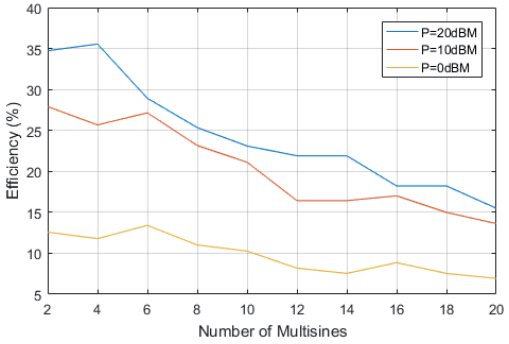

Figure 9. The RF-dc converter results for different transmitted powers, 1 m of distance, with 2 MHz between multi-sines, at 930 MHz.

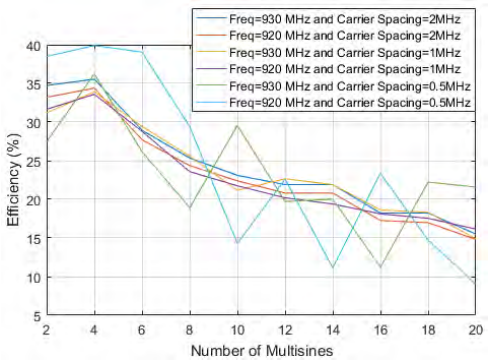

Figure 10. The RF-dc converter results for a distance of 1 m, with a transmitted power of 20 dBm, for two frequencies.

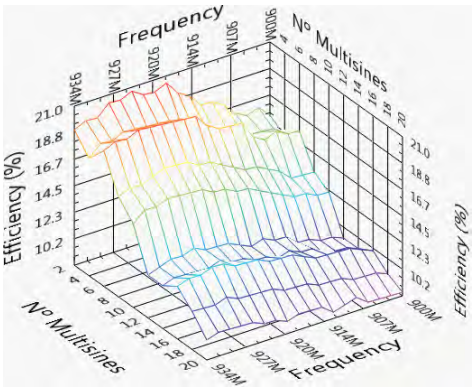

Figure 11. The three-dimensional results for a distance of 0.5 m, for a transmitted power of 0 dBm and with 2 MHz between multi-sines.

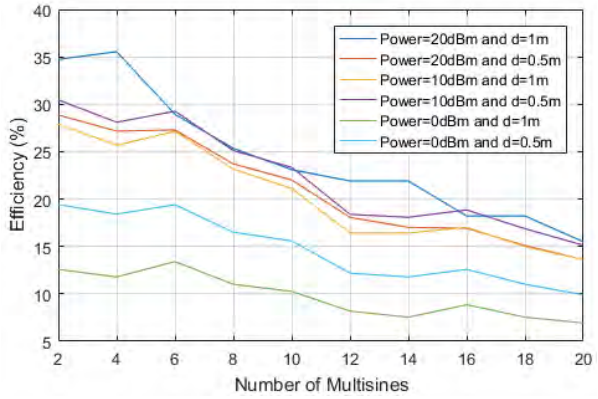

Figure 12. The RF-dc converter results for different transmitted powers and distances, with 2 MHz between multi-sines at 930 MHz.

The multi-sine signal results from the sum of several sine waves each with a given amplitude, phase and frequency. To create a high peak-to-average-power-ratio signal, the sine waves must be constructively combined in phase [1, 2, 10].

5.2 Results

The transmitter from NI only provided power theoretically up to 10 dBm, but effectively just provided 6 dBm of power. In order to achieve more power and consequently to have diverse measurements, a vector signal generator (VSG) from Rohde & Schwarz was used, which was able to provide 20 dBm of power. In this way, the multi-sine signals were generated in *LabVIEW* and then sent to the vector signal generator to maintain the same system/procedure when the NI transmitter was used.

We conducted the measurements to prove that this application had an enormous diversity. First, the antennas were placed at a distance of 1 m from each other. A multi-sine signal was generated of between two to 20 multi-sine signals, and then frequency swept from 900 MHz to 930 MHz. The signals were generated with 20 dBm. The results can be seen in Figure 8. Through the configurations, it could be concluded that the RF-dc converter had better performance when four multi-sines were used.

Other measurements were then conducted for the same distance between antennas (1 m) and the same carrier spacing (2 MHz), but with different transmitted power values, in particular, 10 dBm and 0 dBm. In these cases, the frequencies were also swept (from 900 MHz until 930 MHz). However, to compare the performance at different transmitted power values, results are only shown for one frequency (930 MHz). The respective results are shown in Figure 9. As expected, when the power decreased, the efficiency of the converter also dropped. However, for lower powers, the converter had better efficiency when six multi-sines were used.

In order to show the impact of the space between multi-sines in the RF-dc converter, the device was characterized with a multi-sine signal with carrier spacings of 2 MHz, 1 MHz, and 0.5 MHz. Figure 10 presents the results for a transmitted power value of 20 dBm, for two frequencies (920 MHz and 930 MHz), with a distance of 1 m. In this case, it could be concluded that the device presented a linear performance for 2 MHz and 1 MHz between multi-sines, where the 2 MHz case allowed more efficiency.

The same measurements were thereafter made for a distance of 0.5 m. Figure 11 shows the three-dimensional graphical results for this distance, with a transmitted power of 0 dBm and 2 MHz between multi-sine signals. The results for different distances ($d = 1$ m and $d = 0.5$ m), for 2 MHz between multi-sine signals, and for a frequency of 930 MHz are presented in Figure 12.

6. Conclusion

A characterization system to optimize the performance of RF-dc converters using multi-sine signals was proposed. By using this approach, we were able to get the best multi-sine channel optimization to improve the performance of RF-dc converters. In addition, using this approach, it was possible to study the distance relationship between transmitting and receiving antennas, and the impact on the performance of the device.

7. References

1. A. Boaventura, N. B. Carvalho and A. Georgiadis, "The Impact of Multi-Sine Tone Separation on RF-dc Efficiency," 2014 Asia-Pacific Microwave Conference, Sendai, Japan, 2014, pp. 606-609.

2. D. Belo and N. B. Carvalho, "Harmonic Spaced Multisines for Efficient Wireless Power Transmission," *2015 IEEE Wireless Power Transfer Conference (WPTC)*, Boulder, CO, 2015, pp. 1-4.

3. A. S. Boaventura and N. B. Carvalho, "Spatially-Combined Multisine Transmitter for Wireless Power Transmission," *2013 IEEE Wireless Power Transfer (WPT)*, Perugia, 2013, pp. 21-24.

4. B. Clerckx and E. Bayguzina, "Low-Complexity Adaptive Multisine Waveform Design for Wireless Power Transfer," *IEEE Antennas and Wireless Propagation Letters*, **16**, 2017, pp. 2207-2210.

5. M. S. Trotter, J. D. Griffin and G. D. Durgin "Power-Optimized Waveforms for Improving the Range and Reliability of RFID Systems," IEEE International Conference on RFID, 2009, pp. 80-87.

6. R. D. Fernandes, A. S. Boaventura, N. B. Carvalho and J. N. Matos, "Increasing the Range of Wireless Passive Sensor Nodes Using Multisines," *2011 IEEE International Conference on RFID-Technologies and Applications,* Sitges, 2011, pp. 549-553.

7. A. S. Boaventura and N. B. Carvalho, "Maximizing dc Power in Energy Harvesting Circuits Using Multisine Excitation," IEEE International Microwave Symposium, Baltimore, USA, June 2011.

8. I. Chaour, A. Fakhfakh, and O. Kanoun, "Enhanced Passive RF-dc Converter Circuit Efficiency for Low RF Energy Harvesting," *Sensors*, 2017.

9. K. Nishikawa and H. Sakaki, "Impact of modulation Scheme on Rectifier RF-dc Efficiency and Optimal Signal Control Technique," *2015 IEEE MTT-S International Microwave and RF Conference (IMaRC),* Hyderabad, 2015, pp. 288-291.

10. A. S. Boaventura and N. B. Carvalho, "Maximizing DC Power in Energy Harvesting Circuits Using Multisine Excitation," *2011 IEEE MTT-S International Microwave Symposium,* Baltimore, MD, 2011, pp. 1-4.

In-House Development of 17 GHz Antennas: Potentials and Difficulties

Michael Duarte[1,2], Tiago Varum[1], João Matos[1,2], and Pedro Pinho[1,3]

[1]Instituto de Telecomunicações
Aveiro, Portugal

[2]Universidade de Aveiro
Aveiro, Portugal

[3]Instituto Superior de Engenharia de Lisboa Lisboa, Portugal

E-mail: michael.duarte@ua.pt, tiago.varum@ua.pt, matos@ua.pt, ppinho@deetc.isel.pt

Abstract

The work described in this paper is focused on the design of antennas that could be an asset to the development of high-performance wireless networks in the 17 GHz band. Due to the small size of the antennas at these frequencies, the study of the feeding methods for microstrip antennas was carried out since this is one of the main difficulties in the design. The selected feeding method was aperture-coupling feeding, which has been shown to achieve better performance at this frequency. A group of circularly polarized antennas for indoor and outdoor applications was designed, presenting satisfactory results in terms of bandwidth, gain, and polarization purity.

1. Introduction

Wi-Fi is a technology that provides the user with freedom and flexibility to move around within a certain area and keep a connection to the Internet [1]. It is therefore being widely used everywhere, in both private and public places. Wi-Fi technology is known for being inexpensive to build/implement and free of fees, because it usually operates in the ISM (industrial, scientific, and medical) band, particularly in the bands of 2.4 GHz and 5 GHz.

Nowadays, wireless traffic in these frequency bands has exponentially increased due to its extensive use for applications besides the Wi-Fi solution, and due to the increase in devices with Wi-Fi capabilities. This has led to interference and congestion of the Wi-Fi frequency spectrum, significantly reducing the quality of service provided to users [2].

According to [2], if the frequency spectrum is congested, in order to meet the demands of users it is necessary to reduce the cell size or to deploy a network to another frequency band. One of the possible solutions for these problems is therefore to change the Wi-Fi operating frequency band. The use of a different frequency band higher in the spectrum, in the region of the 17 GHz band, is thus suggested to avoid the congested frequency bands. Moreover, with the increase in frequency it is possible to achieve higher bandwidths, which lead to higher bit rates.

This frequency band has already been identified by the recommendation of the European Radiocommunications Committee (ERC) [3] as a band to meet the needs of high-performance local-area network (HIPERLAN) standards for indoor and outdoor applications. ETSI has intended regulations known as HIPERLINK (also known as HIPERLAN type 4), which have set a 200 MHz bandwidth (17.1 GHz to 17.3 GHz) for transmission rates up to 155 Mbit/s in a surrounding area of 150 m.

Antennas have been constantly studied to improve their range of coverage, increasing the gain, directivity, and bandwidth to meet the demands of the users and of the applications [2, 4]. This paper is therefore focused on the antenna element for a wireless communications system for the 17 GHz band.

According to [4], antennas for indoor Wi-Fi applications should present gains between 0 dBi and 6 dBi, provide omnidirectional coverage, have a high isolation (typically, around 30 dB to 40 dB) between the orthogonal polarizations (for polarized antennas), and should be compact. For outdoor Wi-Fi applications – namely, point-to-point links – it is desired to have antennas with gains up to 29 dBi.

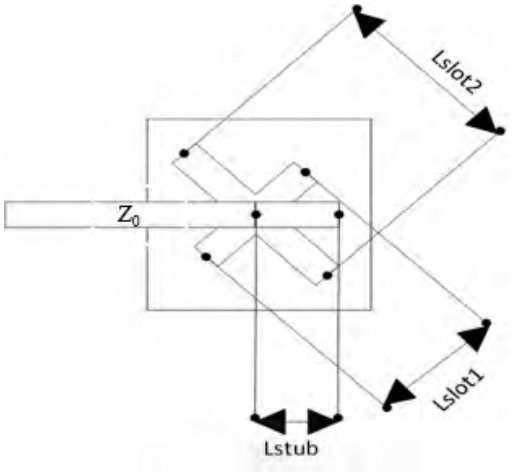

Figure 1. The geometry of an aperture-coupled square microstrip-patch antenna with crossed slots.

This paper will propose two antennas for indoor and outdoor applications with similar characteristics for the antennas operating in the 2.4 GHz and 5 GHz bands. The study and design of these antennas, based on microstrip structures, is presented. They operate in a new range of frequencies in the 17 GHz band, which can add value to the progress of wireless networks. The design steps and the simulation results for two possible antenna solutions for this application are presented.

This paper is divided into six sections, starting with an introduction to the topics addressed. Section 2 describes the selection of the feeding method and the antenna's structure. The design of two circularly polarized aperture-coupled microstrip patches are shown in Sections 3 and 4, with the main simulated results. Section 5 describes the array antenna designed for outdoor Wi-Fi applications, with the results obtained from the simulations. Finally, the most important conclusions are stated in the last section.

2. Selection of the Feeding Method

Microstrip antennas have important features that fit into modern wireless communication systems [5], such as a low profile, high versatility, compactness, low cost, and ease of manufacturing [6]. They therefore present attractive features for Wi-Fi applications and were used in this work. The design process for microstrip-patch antennas was based on the transmission-line model [6].

The dimensions of these antennas depend on both the operating frequency and the characteristics of the dielectric substrate: its thickness (h) and dielectric constant (ε_r). The substrate used was Rogers RO4725 ($h = 0.78$ mm, $\varepsilon_r = 2.55$, and $\tan\delta = 0.0026$). The electromagnetic simulations were performed using CST *Microwave Studio* (CST *MWS*).

One of the main difficulties during the design of antennas for this band (17 GHz) is their feeding, due to their small size (patch dimensions ≈ 6.6 mm × 5 mm). A study of the feeding methods for microstrip antennas was thus carried out.

Several single patches were designed using the different feeding methods studied (microstrip line using a quarter-wavelength transformer, inset-fed line, and aperture coupling), and the aperture-coupling feed stood out. This feeding method presented a larger bandwidth, over 1 GHz, and a gain of about 5 dBi, which was acceptable for these Wi-Fi applications.

The aperture-coupling feed is used to improve the bandwidth in circularly polarized microstrip-patch antennas [7-9]. To improve the reliability of Wi-Fi communications applications independently of the direction of the source at these frequencies, there may be a requirement to use circularly polarized antennas. The aperture-coupling method was therefore chosen. Circularly polarized antennas were also used in this paper since they are able to overcome the problem of multipath fading. Furthermore, the electromagnetic wave emitted by the antenna is more robust to atmospheric attenuation and it does not require the transmitting and receiving antennas to have the same orientation, preventing misalignment [9, 10].

It was demonstrated in [11] that it is possible to obtain circular polarization with two orthogonal non-overlapping slots in a square patch using a 90° hybrid coupler, also known as an off-centered slot feed [12]. A problem found in this solution is the structural asymmetry, which deteriorates the axial ratio and limits the polarization purity.

Another approach is the crossed-slot configuration, formed by a single microstrip feed placed diagonally to the cross [12, 13]. This approach leads to an acceptable polarization bandwidth, does not create asymmetry on the patch antenna, and is simpler to design than the off-centered solution [12].

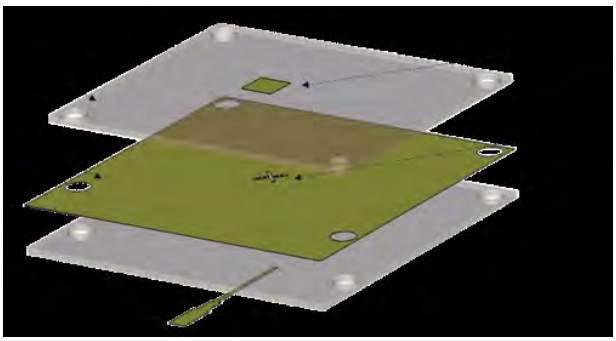

Figure 2. An aperture-coupled patch antenna using a crossed slot.

Table 1. The design parameters for the microstrip patch with crossed slots.

Parameter	Dimension (mm)
W	4
L	4
L_a	3.65
K_s	1.15
W_{z0}	0.55
L_{z0}	12.00
L_{stub}	2.10
Antenna size	(48.06 × 48.06)

3. Design of the Aperture-Coupled Microstrip-Patch Antenna with Crossed Slot

The crossed slot was centered with the square patch (the width and length of the patch were equal), and shifted 45° with respect to the microstrip feed line, as can be observed in Figure 1. The antenna's structure has several layers, as shown in Figure 2.

The first step performed in the design of the antenna was a study of the impact of each dimensional parameter on the antenna's performance, namely the width (W) and length (L) of the patch, the length of each slot (L_{slot1}, L_{slot2}), and the length of the stub (L_{stub}). To simplify this study, the width of each slot was set to be 10% of the corresponding slot's length. It was concluded that the operating frequency of the antenna depended on the slot length, since that defines the amount of coupling between the feed line and the patch [12]. It was also verified that the ratio between the length of the slots (K_s *Ks*) has a major impact on the axial ratio, as it was mentioned in [13, 14]. The length of the stub (L_{stub}) only affects the impedance matching of the antenna [14].

At this point, the design procedure presented in [14] was followed, and the optimization of the antennas was performed using the CST tool. According to [15], the length of each slot (L_{slot1}, L_{slot2}) depends on the average of the lengths of the slots (L_a), which will impact the amount of coupling (in other words, this defines the size and resonance of the slots), and K_s, per Equations (1)-(3).

$$K_s = \frac{L_{slot1}}{L_{slot2}}, \tag{1}$$

$$L_{slot1} = \frac{2L_a}{K_s + 1}, \tag{2}$$

$$L_{slot2} = \frac{2L_a K_s}{K_s + 1}. \tag{3}$$

The first step was therefore to find the L_a dimension that led to a satisfactory amount of coupling. By using the parameter-sweep tool of CST *MWS*, the L_a dimension that led to a better result in terms of impedance matching was 3.65 mm. Using the same method, the slot ratio that allowed achieving an acceptable polarization level was then found to be between 1.1 and 1.2. The dimensions of the designed antenna are presented in Table 1.

3.1 Simulation Results

The antenna was designed and simulated using CST *MWS*, and its main parameters were analyzed. As could be observed in Figure 3, the antenna presented an S_{11} of −26 dB at 17 GHz, and an impedance matching bandwidth (assuming the criteria of $S_{11} < -10$ dB) of 2.3 GHz (14%).

The axial ratio measures the quality/purity of the circular polarization [6]. Whenever the axial ratio is lower than 3 dB, the antenna is considered to have an acceptable circular polarization, 0 dB being the ideal value. The designed antenna presented an axial ratio of 0.56 dB at

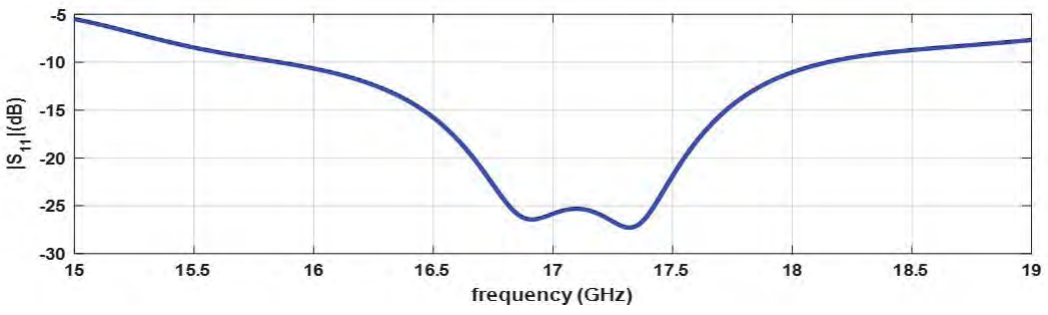

Figure 3. The simulated S_{11} values of the designed patch antenna.

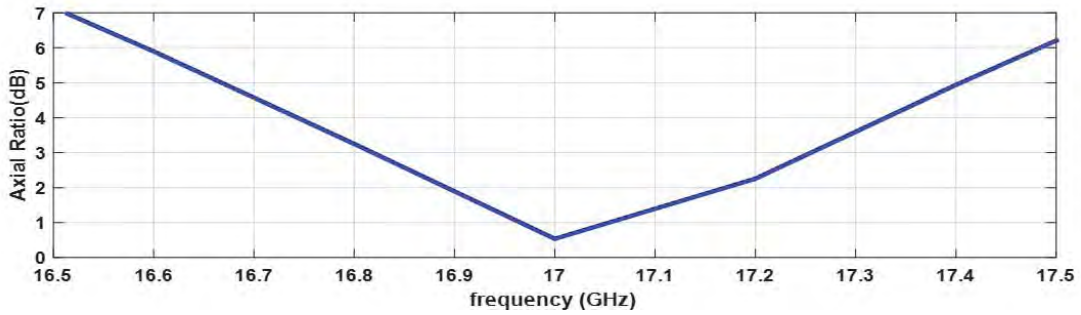

Figure 4. The simulated axial ratio of the designed patch antenna.

17 GHz, and an axial-ratio bandwidth of about 500 MHz (from 16.8 GHz to 17.3 GHz), as is shown in Figure 4.

The antenna therefore had the desired characteristics between 16.8 GHz and 17.3 GHz (3%), where it presented a fine impedance match and good circular polarization.

Concerning the circular polarization, by analyzing the radiation pattern of the antenna (in Figure 5), it was possible to verify that the antenna had right-hand circular polarization (RHCP) with a left-hand component rejection of 30 dB. Finally, the antenna presented a gain of 5.3 dBi and a directivity of 5.8 dB in the boresight direction.

4. Design of the Aperture-Coupled Microstrip-Patch Antenna with Off-Centered Feed Using a 90° Quadrature Hybrid

The antenna with off-centered feed is formed by a square patch above a ground plane where the two non-overlapping off-centered slots are placed. The feed network is located on the bottom layer. It is composed of a power divider that creates a 90° shift between the ports that feed the slots, which excite two orthogonal propagation modes, creating circular polarization.

The first step in the development of the antenna was the design of the microstrip quadrature hybrid coupler out of the antenna's structure, shown in Figure 6. The theoretical dimensions were used as a starting point, and it was optimized in CST *MWS*. From this process, the obtained the dimensions that are listed in Table 2.

The design of the aperture-coupled microstrip patch antenna previously described at 17 GHz, but using two independent slots, led to their intersection. The configuration presented in Figure 7 was therefore used. This was suggested by [16] and it was shown to be possible to obtain circular polarization, impedance matching, and to avoid the intersection of the slots. As can be observed in Figure 7, two symmetry axes of the square patch (A) and (B) were drawn. Axis (A) divided the patch into two symmetric parts, and in each part was placed one slot centered on the symmetry axis (B) with orthogonal positions (horizontal, vertical), also referred to as a T configuration [16]. The distance between the centers of each slot to the center of

Table 2. The dimensions of the hybrid obtained in CST *MWS*.

Impedance (Ω)		Dimensions (mm)				
Z_0	Z_a	W_{Z0}	W_a	L_1	L_a	L_{Z0}
100	70.71	0.55	0.9	3.9	3.6	2

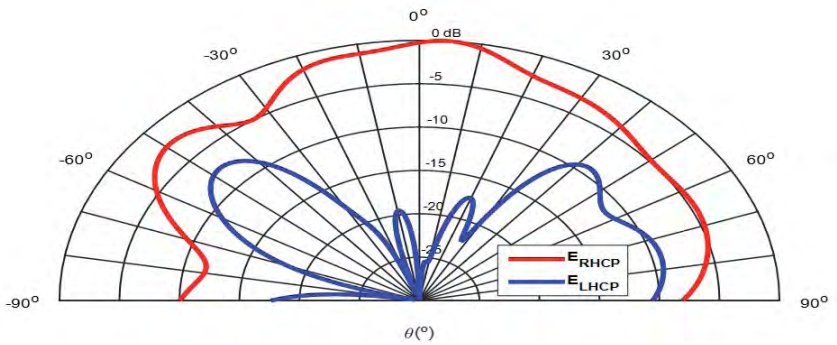

Figure 5. The normalized radiation patterns of the designed antenna for right-hand and left-hand polarization components.

Table 3. The dimensions of the designed antenna.

Parameter	Dimensions (mm)
W	4.1
L	4.1
L_{slot1}	1.88
L_{H1}	1.3
W_{slot1}	0.48
W_{H1}	0.39
L_{slot2}	1.34
L_{H2}	1.64
W_{slot2}	0.43
W_{H2}	0.45
Antenna size	45.77 × 45.77

the patch was set to be 1 mm. This was the shortest distance that avoided the intersection of the slots and guaranteed that the slots were immediately under the patch. In the T configuration, each of the slots presented a different position relative to the patch antenna, leading to a different impedance seen by each slot. *slot_1* and *slot_2* therefore had different dimensions.

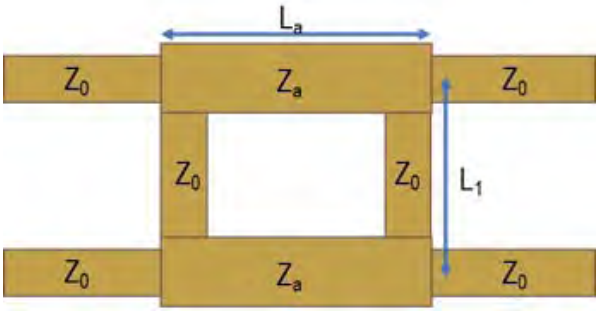

Figure 6. A schematic of a quadrature hybrid.

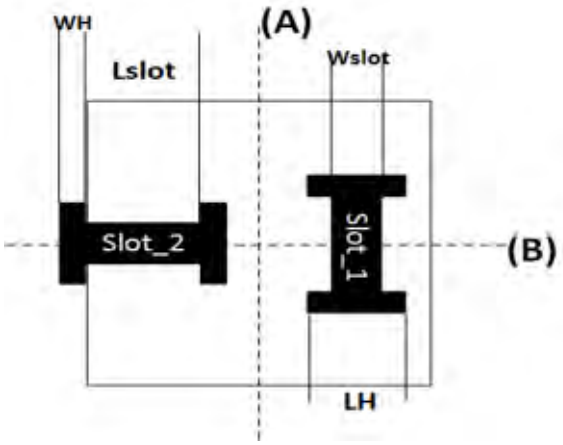

Figure 7. A schematic of the slot configuration used.

Note that in the beginning of the antenna design, the feed network was formed only by two feed lines (one for each slot), and the CST *MWS* tool created the phase difference. The following step was therefore to design the microstrip lines that were responsible for the "connection" between the slots and the quadrature hybrid. It was ensured that the phase offset created in each of these feed lines was the same to guarantee that the phase difference of the signal at each slot was created exclusively by the quadrature hybrid. Finally, the quadrature hybrid was introduced into the antenna's structure, and the overall performance was tested. Figure 8 presents the structure of the designed antenna, and its dimensions are listed in Table 3.

4.1 Simulation Results

The antenna was designed, simulated, and its main parameters, which are presented in the following figures, were analyzed.

Concerning the impedance matching, by observing Figure 9, it was possible to conclude that the antenna had a satisfactory S_{11}, both when the signal was applied to port 1 (−22 dB at 17 GHz) or at port 2 (−30 dB at 17 GHz). It also

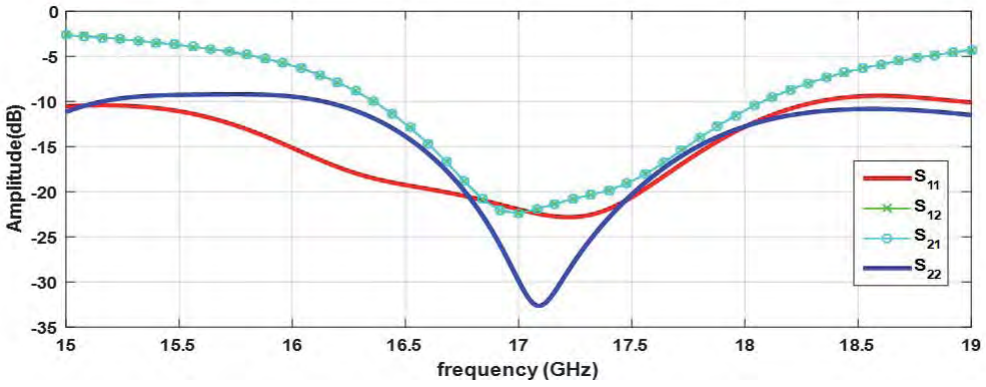

Figure 8. The antenna's structure designed in CST MWS.

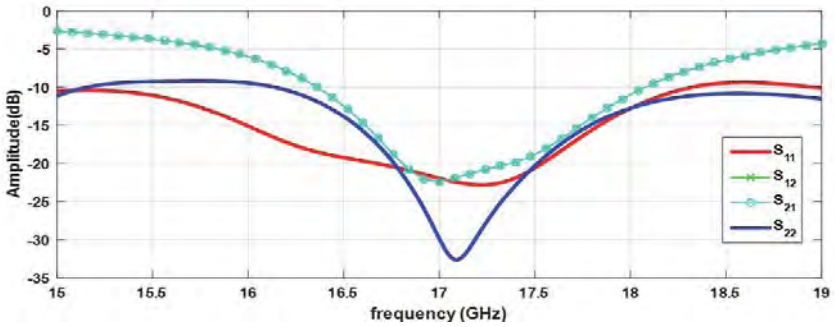

Figure 9. The simulated S_{11}, S_{12}, S_{21}, and S_{22} values of the designed antenna.

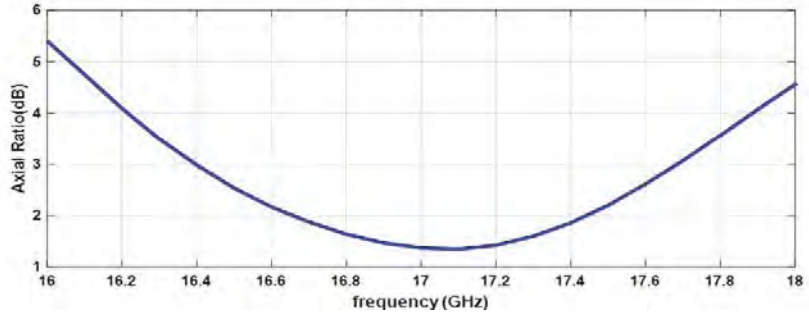

Figure 10. The simulated axial ratio of the patch antenna.

achieved high isolation between port 1 and port 2 (−22 dB at 17 GHz), as could be observed from the S_{12} and S_{21} parameters (which were the same) presented in Figure 9.

The antenna presented a different impedance bandwidth depending on to which port the signal was applied. When the signal was applied to port 1, the antenna presented an impedance bandwidth of 3.33 GHz (20%). When the signal was applied to port 2, the antenna presented an impedance bandwidth of 2.86 GHz (17%).

In terms of circular polarization, it was possible to observe the axial ratio of the antenna in Figure 10. For the intended operating frequency it presented a value of 1.37 dB. The axial-ratio bandwidth was 1.32 GHz (8%).

As was already mentioned, this antenna allows choosing the orientation of the circular polarization. Left-hand circular polarization (LHCP) was obtained when the signal was applied to port 2 and port 1 was terminated with a matched load. The antenna presented a right-hand-component rejection of 23.7 dB in the boresight direction ($\theta = 0°$), shown in Figure 11. For left-hand circular polarization, the antenna had a bandwidth of 1.32 GHz (8%) and presented a gain of 5.8 dBi.

When the signal was applied to port 1 and port 2 was terminated by a matched load, it accomplished right-hand circular polarization. In this case, the antenna showed a left-hand-component rejection of 22 dB on boresight, as could be seen in Figure 12. For right-hand circular polarization,

Table 4. The variation of the gain with the distance between the elements.

Spacing Between Elements (As a Function of Wavelength)	Gain (dB)
0.5λ	7.4
0.6λ	7.9
0.7λ	8.0
0.8λ	7.9
0.9λ	7.8
λ	7.8

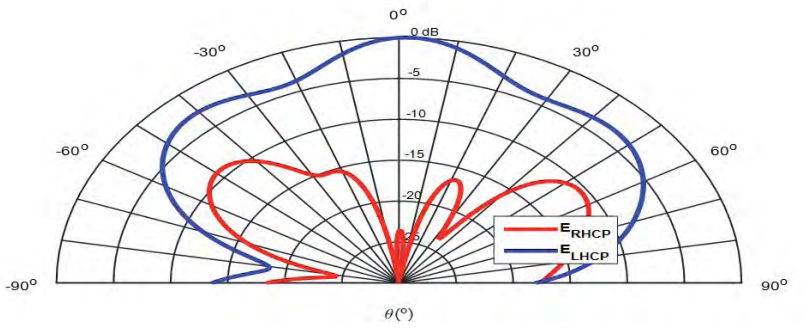

Figure 11. The radiation pattern of the antenna (showing the left-hand circular polarization and right-hand circular polarization components) when the signal was applied to port 2.

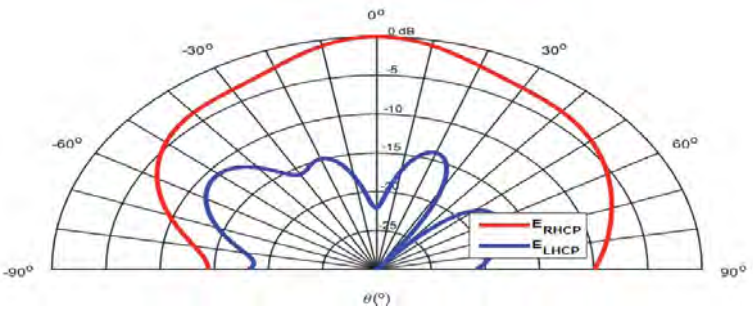

Figure 12. The radiation pattern of the antenna (showing the left-hand circular polarization and right-hand circular polarization components) when the signal was applied to port 1.

the antenna presented a bandwidth of 1.32 GHz (8%) and had a gain of 5.8 dBi.

Figure 13 shows the radiation efficiency of the antenna as a function of frequency, showing curves when it was fed in both port 1 and in port 2. It was possible to verify that the antenna had a maximum in efficiency around the frequency of interest, close to 94%. However, between 16 GHz and 18 GHz, the radiation efficiency was always higher than 90%, which is an important value considering the complexity of the antenna's structure.

5. Design of a 4×4 Array Antenna for Outdoor Wi-Fi Applications

The primary step was to design an array with two elements (Figure 14) to understand the influence of the distance between the elements of the array on the gain and on the radiation pattern of the antenna. A sweep of the distance between elements was performed using CST MWS. The maximum gain was obtained with an element spacing of $0.7\lambda_0$, as it was possible to conclude by observing Table 4.

The radiation pattern of the two-element antenna array is presented in Figure 15 for the main radiation plane affected by the two elements. It could be seen that the main lobe was more directive, and the sidelobes appeared as the distance between the elements increased.

The distance between elements was chosen to accomplish higher gain with the lowest sidelobe level. The distance was set to be $0.65\lambda_0$, presenting a gain of 8 dBi. The patch element was then placed in a 2×2 array

Table 5. The dimension of a single element placed in the array configuration.

Parameter	W	L	L_a	K_s	L_{stub}
Dimensions (mm)	3.93	3.93	3.71	1.12	2.10

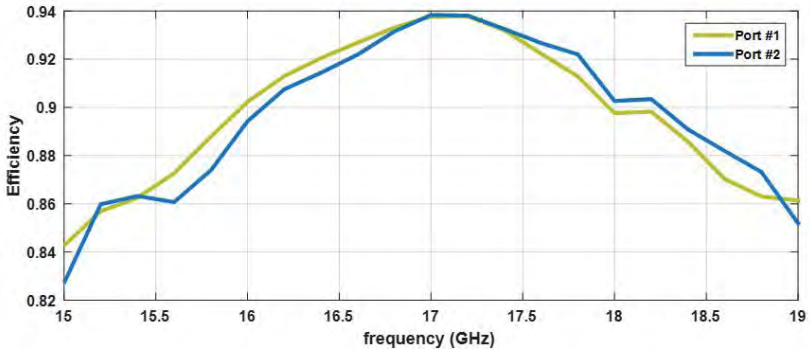

Figure 13. The simulated radiation efficiency of the designed antenna.

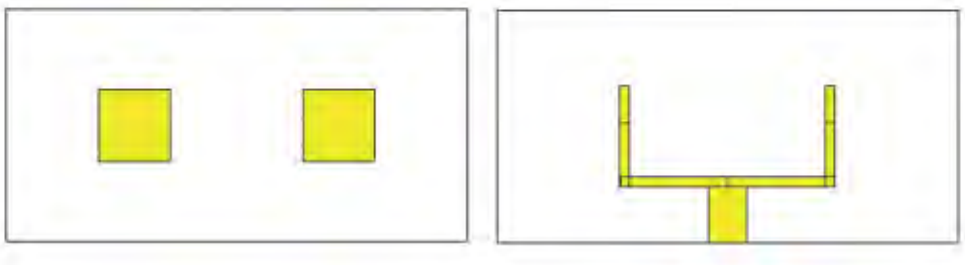

Figure 14. The two-element antenna array as designed (front and back views)

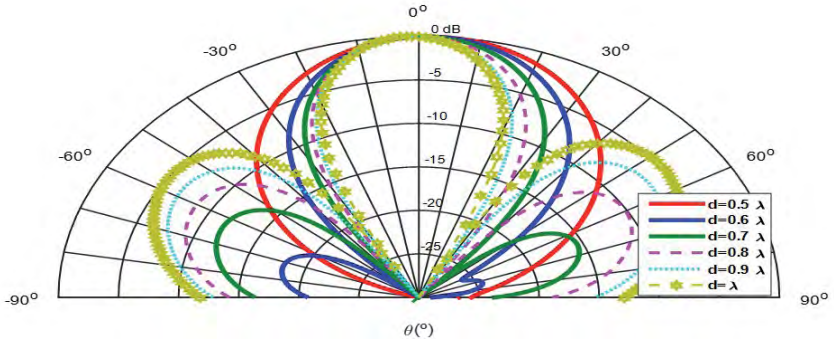

Figure 15. The variation of the radiation pattern of the 1×2 array antenna as a function of the distance between the antenna elements.

configuration, without any feed network connecting the elements. They were fed using a CST MSW tool that allowed simultaneously feeding the four elements. It was possible to notice the impact of the mutual coupling in the impedance matching and the axial ratio. To compensate for this phenomenon, the sizes of the elements were adjusted, and the parameters obtained are given in Table 5 (these dimensions are referred to the previous single-element design with the crossed slots that composed the array).

The feed network that connected all four elements of the array antenna was designed, as shown in Figure 16. It started with a 100 Ω characteristic impedance microstrip line connected to the patch (this was the impedance used to feed the single patch). The feed network was formed by microstrip lines of 50 Ω and 100 Ω characteristic impedance, and $\lambda/4$ impedance transformers, to transform the impedance observed at a certain point to the desired impedance.

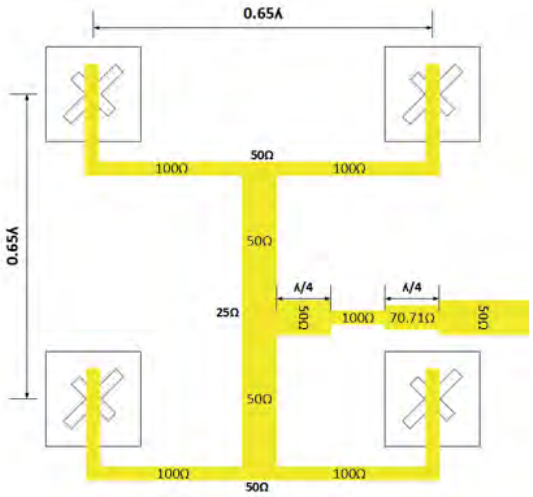

Figure 16. A schematic of the antenna's array feed network.

5.1 Simulation Results

The 2×2 antenna array was designed in CST MSW, and its structure is shown in Figure 17. It was simulated, and its main resulting parameters, as presented in the next figures, were analyzed in terms of impedance matching, polarization, and radiation pattern.

In terms of impedance matching, it was possible to observe the S_{11} of the antenna in Figure 18, which for the operating frequency presented a value of −32.9 dB. The antenna therefore presented an insignificant reflected wave (most of the power was accepted by the antenna). The array antenna had an impedance bandwidth of 1.27 GHz between 16.33 GHz and 17.60 GHz.

Since the single element had right-hand circular polarization, it was expected that the array would have the same polarization orientation. The antenna presented a left-hand component rejection of 30.3 dB on boresight as was shown in Figure 19 for the plane $\varphi = 0°$. The

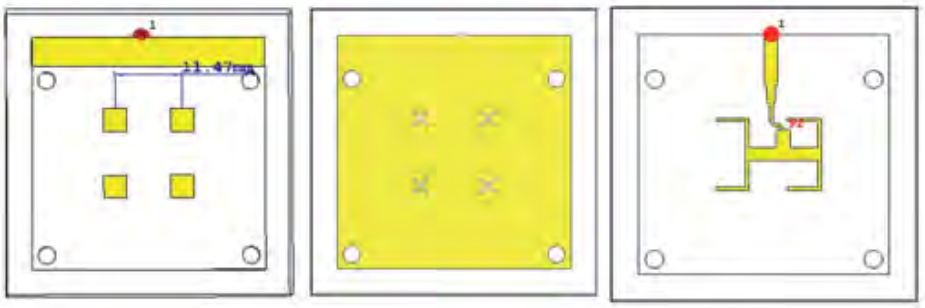

Figure 17. The antenna array implemented in CST MSW (front, ground, and back views).

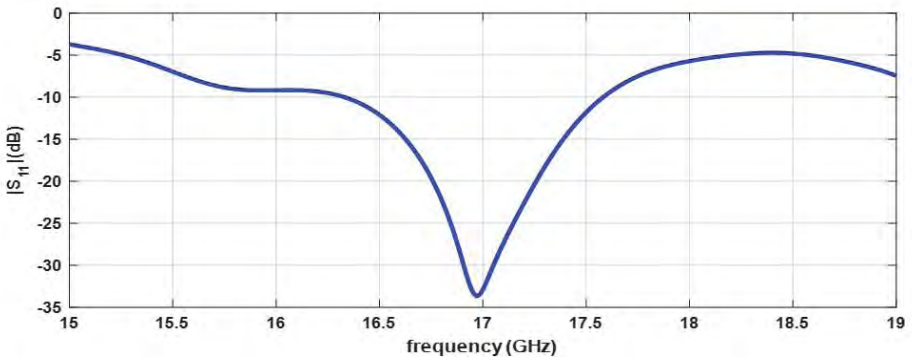

Figure 18. The simulated S_{11} values (dB) of the designed array antenna.

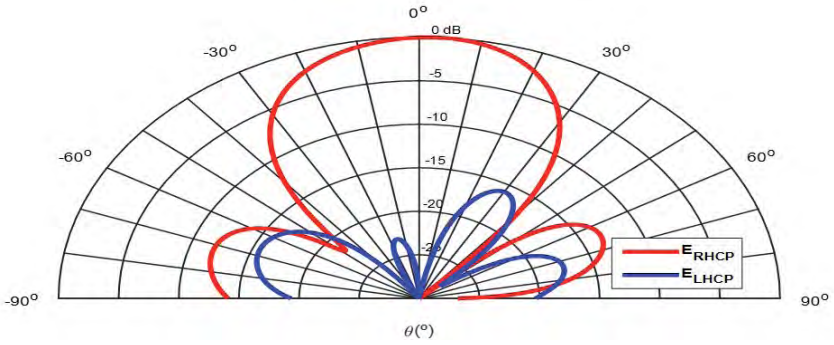

Figure 19. The simulated radiation pattern of the designed antenna array (showing the left-hand circular polarization and right-hand circular polarization components) for the plane $\varphi = 0°$.

purity of the circular polarization was also verified by the axial-ratio value, which for the operating frequency was 0.53 dB, as shown in Figure 20. The array antenna presented a suitable circular polarization and impedance matching between 16.85 GHz and 17.19 GHz, so the antenna had a bandwidth of 340 MHz.

The designed antenna array presented a gain of 10.1 dBi and a sidelobe level of -12.2 dB. The array presented a half-power beamwidth of 45° in the plane $\varphi = 0°$ and 47° in the $\varphi = 90°$ plane.

6. Conclusions

A group of antennas was presented in this paper for Wi-Fi applications in a higher frequency band. We assumed this frequency to be around the 17 GHz spectrum zone, since it was already recommended for high-performance wireless networks. Both of the designed antennas were similar in terms of gain and size, and obeyed the requirements for Wi-Fi applications. However, their performance related to polarization was different. The antenna with crossed slots showed a better polarization purity level and a higher

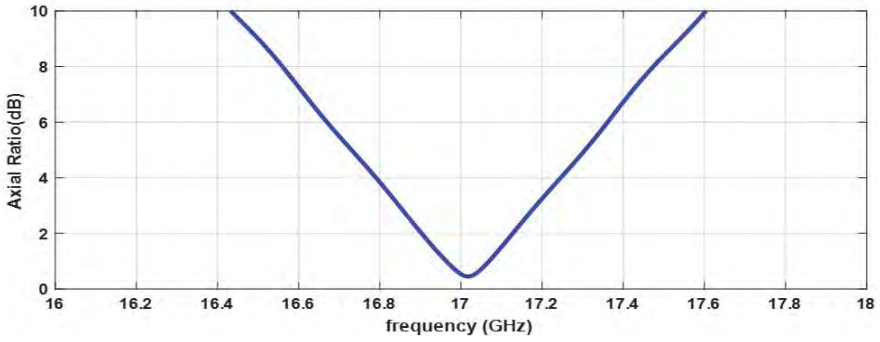

Figure 20. The axial ratio of the designed antenna array.

rejection level of the orthogonal component. These results were explained by the simpler structure of the antenna with crossed slots when compared to the antenna with off-centered slots. The antenna with off-centered slots presented a more complex design, due to the complexity of its structure. However, it allowed obtaining both right-hand circular polarization and left-hand circular polarization without any change in the antenna's structure, in contrast to the antenna with crossed slots, and achieved a wider bandwidth. The antenna array presented a gain around 10 dBi, which was acceptable for both point-to-point and point-to-multipoint applications.

7. Acknowledgment

This work was supported by the European Regional Development Fund (FEDER), through the Competitiveness and Internationalization Operational Programme (COMPETE 2020) of the Portugal 2020 framework, Project, RETIOT, POCI-01-0145-FEDER-016432.

8. References

1. K. Dinakaran, M. Vajikabanu, M. Piriyadharsini, and D. Rajeshwari, "Design of Microstrip Patch Antenna for Wi-Fi Applications" *International Journal of Advanced Research in Electronics and Communication Engineering*, **5**, 1, January 2016, pp. 38-41.

2. C. Kienmayer, R. Thuringer, M. Tiebout, W. Simburger and A. L. Scholtz, "An Integrated 17 GHz Front-End for ISM/WLAN Applications in 0.13 µm CMOS," 2004 Symposium on VLSI Circuits, Digest of Technical Papers, Honolulu, USA, June 2004, pp. 12-15.

3. CEPT Recommendation T/R 22-06: "Relating to the Harmonised Radio Frequency Bands for HIgh PErformance Radio Local Area Networks (HIPERLANs) in the 5 GHz and 17 GHz Frequency Range," European Communications Office, 2001 (http://www.erodocdb.dk/Docs/doc98/official/pdf/TR2206E.PDF).

4. Z. N. Chen, X. Qing, T. S. P. See and W. K. Toh, "Antennas for Wi-Fi Connectivity," *Proceedings of the IEEE*, **100**, 7, July 2012, pp. 2322-2329.

5. N. Mohamed, S. Banu, M. R. Prabhu, and U. T. Sasikala, "Design a Square Microstrip Patch Antenna for S-Band Application," *Journal of Electronics and Communication Engineering*, **10**, 2, March 2015, pp. 2-30.

6. C. A. Balanis, *Antenna Theory: Analysis and Design, Third Edition*, New York, USA, John Wiley & Sons, 2005.

7. R. C. Paryani, *Design of a Wideband Dual-Polarized Cavity Backed Slot Antenna*, PhD Thesis, University of Central Florida, 2010, archived at http://purl.fcla.edu/fcla/etd/CFE0003066

8. M. H. C. Dias, B. R. Franciscatto, E. M. B. Nogueira and T. P. Vuong, "On the Design of a Dual-Fed Aperture-Coupled Circularly Polarized Microstrip Patch Antenna," 2013 SBMO/IEEE MTT-S International Microwave & Optoelectronics Conference (IMOC), Rio de Janeiro, Brazil, August 2013, pp. 1-5.

9. D. Pavithra and K. R. Dharani, "A Design of H-Shape Microstrip Patch Antenna for WLAN Applications," *International Journal of Engineering Science Invention*, **2**, 6, June 2013, pp. 71-74.

10. Intelsat: Circular Polarization vs. Linear Polarization, [http://www.intelsat.com/wp-content/uploads/2013/02/Polarization.pdf]

11. A. Adrian and D. H. Schaubert, "Dual Aperture-Coupled Microstrip Antenna for Dual or Circular Polarisation," *Electronics Letters*, **23**, 23, November 1987, pp. 1226-1228.

12. D. M. Pozar, "A Review of Aperture Coupled Microstrip Antennas: History, Operation, Development, and Application," May 1996, Internet Archive of University Massachusetts at Amherst, archived at http://www.ecs.umass.edu/ece/pozar/aperture.pdf.

13. J. Coll, A. Skrivervik, J. Casals, and M. Veljovic, "X-Band Antenna for Cubesat Satellite," Laboratory of Electromagnetics and Antennas, École Polytechnique Fédérale de Lausanne, 2017, archived at http://hdl.handle.net/2117/100554

14. M. Albooyeh, N. Kamjani, and M. Shobeyri, "A Novel Cross-Slot Geometry To Improve Impedance Bandwidth of Microstrip Antennas," *Progress In Electromagnetics Research Letters*, **4**, 2008, pp. 63-72.

15. G. S. Kirov and D. P. Mihaylova, "Circularly Polarized Aperture Coupled Microstrip Antenna with Resonant Slots and a Screen," *Radioengineering*, **19**, 1, April 2010, pp. 111-116.

16. S. C. Gao, L. W. Li, P. Gardner and P. S. Hall, "Wideband Dual-Polarised Microstrip Patch Antenna," *Electronics Letters*, **37**, 20, September 2001, pp. 1213-1214.

Second Announcement

URSI AP-RASC

2019 URSI Asia Pacific Radio Science Conference

India Habitat Centre, Delhi, India

9-15 March 2019, New Delhi, India

www.aprasc2019.com

Asia Pacific Radio Science Conference (AP-RASC) is a triennial flagship event of the International Union of Radio Science (URSI). It is an international conference in the field of radio science, where eminent researchers and experts from all over the world gather to share their knowledge and experience, and also to encourage scientific exchange and fellowship amongst industry colleagues and professionals globally. It is our pleasure to invite participation to AP-RASC 2019 not just from Asia but also from Europe, South and North America, Oceania and Africa. The scientific program will provide an opportunity for participants to exchange new ideas and information on many important issues related to recent advances in radio science. Presented papers will be submitted to IEEE Xplore, if the authors choose. The scope of radio science broadly covered in the AP-RASC 2019 falls under the ten commission of URSI as follows.

A continent-sized country, India possesses an amazing wealth of sights and sounds, tastes and textures. As a tourist destination, India will be very attractive to all delegates whether it is adventure, heritage or eco-tourism.

Topical Areas

- Commission A: Electromagnetic Metrology, Electromagnetic Measurements and Standards
- Commission B: Fields and Waves
- Commission C: Radio-communication Systems and Signal Processing
- Commission D: Electronics and Photonics
- Commission E: Electromagnetic Noise and Interference
- Commission F: Wave Propagation and Remote Sensing
- Commission G: Ionospheric Radio and Propagation
- Commission H: Waves in Plasmas
- Commission J: Radio Astronomy
- Commission K: Electromagnetics in Biology and Medicine

Important Dates

- Paper Submission Open
  01 August, 2018
- Paper Submission Deadline
  15 October, 2018
- Acceptance Notification
  01 December, 2018
- Online Registration Open
  01 September, 2018
- Early Bird Registration End
  15 January, 2019

Young Scientist Programs

The following two programs are planned for young scientists:

- Student Paper Competition (SPC)
- Young Scientist Award (YSA)

Conference Chairs

Prof Subra Ananthakrishnan
General Chair

Prof Kazuya Kobayashi
General Co-Chair

Prof Piergiorgio L E Uslenghi
General Co-Chair

Dr Amitava Sen Gupta
Chair, Local Organizing Committee

In Memoriam: Don Farley

Don Farley, pioneer of incoherent-scatter radar theory, world leader of ionospheric research, and inspiring teacher and mentor, died peacefully in Ithaca, New York, on May 13, 2018. He was 84.

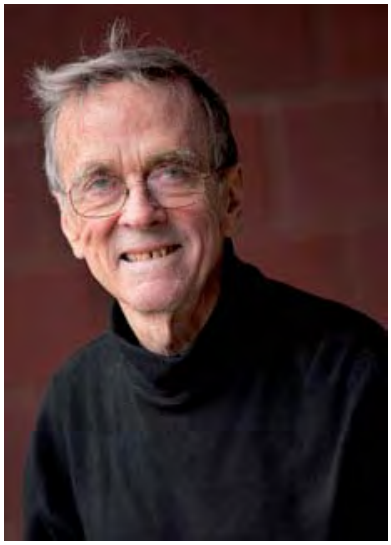

Don entered the College of Engineering at Cornell University under a full athletic scholarship, running for the track and cross-country teams. After receiving his BEng Phys and PhD degrees from Cornell, Don spent a year at Cambridge University as a NATO Postdoctoral Fellow and a year as Docent at Chalmers University in Sweden. He then spent six years in Peru at the Jicamarca Radio Observatory, three of them as director, before returning to the United States and joining the Cornell faculty as a full professor in 1967. He returned to Sweden in 1985 for a year as the Tage Erlander Visiting Professor at the Uppsala Ionospheric Observatory. In 1995, he was the Von Humboldt Senior Scientist at the Max-Planck Institute fur Aeronomie in Katlenberg-Lindau. Between 1979 and 2003, he was the Principal Investigator for the NSF award supporting research at Jicamarca. Don was the J. Preston Levis Professor of Engineering in Electrical and Computer Engineering at Cornell, before becoming Professor Emeritus in 2006.

Throughout his career, Don was a pioneer in radio and space physics. His PhD work considered how electrostatic fields vary along geomagnetic field lines. However, his best-known early-career work focused on the development of incoherent-scatter theory, the theory of radiowave scattering from thermal density fluctuations in ionospheric plasmas. Incoherent scatter would become the most incisive tool available for studying ionospheric plasmas from the ground. Don developed not only the theory but also the practical methods for ionospheric research with incoherent scatter at emerging facilities such as the Arecibo Radio Telescope in Puerto Rico and at the Jicamarca Radio Observatory in Peru. It was especially at the latter facility where the effects of the Earth's magnetic field required special attention. Working at Jicamarca, Don also discovered the class of electrojet plasma waves and instabilities now known also to exist at middle and high latitudes, and that now bear his name. Don also introduced important new methods to radio science, including radar interferometry, which plays a key role not only in ionospheric research but also in radar studies of the mesosphere, stratosphere, and troposphere (MST).

Don was a Fellow of the Institute of Electrical and Electronics Engineers, and a member of the American Geophysical Union, the International Union of Radio Scientific (URSI), and the American Association for the Advancement of Science. He received US Department of Commerce Distinguished Authorship awards in 1963 and 1964, as well as the US Department of Commerce Gold Medal in 1967. He was the recipient of the 1996 URSI Sir Edward Appleton Prize, the 1997 Royal Astronomical Society Gold Medal for Geophysics, and the 2010 Hannes Alfvén Medal from the European Geophysical Union, in addition to awards for teaching and advising at Cornell. He was the recipient of the CEDAR Distinguished Lecture in 2012 (https://cedarweb.vsp.ucar.edu/wiki/index.php/Workshop:CEDAR_Distinguished).

First and foremost, Don was a teacher and adviser whose door was never closed to his students. Quite a few of Don's students, and some of their students, are working in radio and space physics today because of him. Don Farley was a brilliant, accomplished, and unpretentious scientist, teacher, and mentor. He will be sorely missed.

David Hysell
Earth and Atmospheric Sciences
Cornell University
E-mail: dlh37@cornell.edu

In Memoriam:
E. Folke Bolinder

Prof. E. (Erik) Folke Bolinder passed away on March 1, 2018, in Gothenburg, Sweden. He was born on August 11, 1922, in Uppsala, Sweden. He received the Master's degree in 1946, the degree of Teknologie Licentiat in 1954, and the Teknologie Doktor (PhD) degree in 1959, all at the Royal Institute of Technology (KTH), Department of Electrical Engineering, Stockholm, Sweden.

After a year of military service as a Special Engineer in the Swedish Air Force, he started a professional career in governmental institutions. He became a Radio Engineer at the Aviation Administration (1945), at the Naval Administration (1946), and at the Swedish Defence Research Agency (FOA) from 1947 to 1951, working on different microwave projects and combining the work with graduate studies at the Royal Institute of Technology.

In 1951, he became a Fellow of the Sweden-America Foundation, under whose auspices he worked (1952-1953) in transient synthesis as a Research Assistant at the Research Laboratory of Electronics, Massachusetts Institute of Technology (MIT), Cambridge. During the winter of 1954-1955, he carried out research at the Institute Nacional de la Investigación Científica, Mexico City. During 1955-1957, he was a Research Staff Member of the Research Laboratory of Electronics at MIT. He then worked as a Physicist in the US Air Force Cambridge Research Laboratories, Bedford, Massachusetts, during 1958-1963, and served as a consultant to FOA in 1963-1964.

He was Professor in Network Theory at Chalmers University of Technology, Gothenburg, Sweden from 1964 until his retirement in 1989. At Chalmers, Prof. Folke Bolinder started and led a very active research group the main interest of which was phased-array theory and design. An early achievement in the 1960s was a 137 MHz linear antenna, designed to receive the weather information from a satellite, and a ferrite-controlled X-band phased array. In the beginning of the 1970s, a very innovative antenna, CHALMANT (CHAlmers L-band Maritime ANTenna), was successfully used to communicate between a ship and a Marisat satellite (an Inmarsat precursor maritime satellite system). This antenna consisted of a large two-dimensional planar 8×8 cavity-backed slot antenna phased array at 1.6 GHz (uplink) and 1.5 GHz (downlink). With mechanical rotation in azimuth and electronic scan in elevation, this antenna was followed by the CHALSCAN conformal cylindrical phased array of 8×4 elements. During a period of more than 20 years, Prof. Bolinder's group of network theory kept very close ties with the FOA and with Ericsson antenna departments. This fruitful cooperation was the basis for Ericsson's present activity in phased arrays. A strong cooperation was also established in slotted waveguide arrays, leading to several military and satellite antennas. The group also developed the theory for dichroic surfaces that was used in the ESA Rosetta space probe.

Prof. Bolinder's personal interests were of a more theoretical nature. He authored publications in electrical circuit theory, and microwave and antenna theory. Worth mentioning here are "The Relationship of Physical Applications of Fourier Transforms in Various Fields of Wave Theory and Circuitry" (*IRE Transactions on Microwave Theory and Techniques*, 1957) and "Geometric Analysis of Partially Polarized Electromagnetic Waves" (*IEEE Transactions on Antennas and Propagation*, 1967).

A special interest – and his true research love – was the application of Clifford algebra and Clifford numbers to circuit theory and electromagnetics. His interest for this unusual topic was aroused when he attended a series of seminal lectures that the great mathematician, Marcel Riesz, delivered at the University of Maryland, College Park, between October 1957 and January 1958. These lectures, supplemented by additional notes that Riesz dictated to Folke in the following year, became a book edited by P. Lounesto and E. F. Bolinder (Marcel Riesz, *Clifford Numbers and Spinors*, Kluwer Academic, 1993). This provided a thorough introduction to Clifford algebra and the basis for further research on the subject. An excellent summary of Clifford algebra, including applications to network and electromagnetic theories, can be found in the paper, "Clifford Algebra: What Is It?," which Prof. Bolinder wrote for the August 1987 *IEEE Antennas and Propagation Society Newsletter*, following an international NATO/SERC workshop held at the University of Kent, England, during September 15-27, 1985, on the topic "Clifford Algebras and Their Applications in Mathematical Physics."

Prof. Bolinder is warmly remembered among the European community of antenna researchers for his invaluable activity within the European Cooperation in Science and Technology (COST) initiatives (http://www.cost.eu/). Folke initiated and lead, over almost a quarter of a century (1973-1997), five COST Actions in Antennas that created a unique forum for technical exchange in the field of antennas in Europe. The number of participating European countries grew from five in the first Action ("Aerial Networks with Phase Control," 1973-1977) to eighteen in the last Action chaired by Prof. Bolinder ("Active Phased Arrays and Array Fed Antennas," 1993-1997). After his retirement, his initiative continued with further Antenna COST Actions, including up to 27 European countries

The strong momentum created by Prof. Bolinder in these Actions resulted eventually in lasting institutions such as the European Association on Antennas and Propagation (EurAAP), the annual European Conference on Antennas and Propagation (EuCAP), and the European School of Antennas (ESoA).

Prof. Folke Bolinder is remembered by all of us as a remarkable creative leader and as a very kind and sociable person. His concluding joke at the end of the social COST events became a truly appreciated tradition, which was mandatory to follow for all the COST Antenna chairpersons who came after him.

His burial notice included this citation, attributed to Albert Einstein: "Logic will get you from A to B. Imagination will take you wherever." Folke certainly led us to unexpected developments.

Juan R. Mosig (juan.mosig@epfl.ch)
Peter Balling
Per Ingvarson
Antoine Roederer
Piotr Starski

In Memoriam: Bill Wright

Bill Wright, a pioneer in HF ionospheric sounding using advanced techniques, passed away on May 5, 2018, in Longmont Colorado.

Figure 1. John William (Bill) Wright.

John William Wright (Figure 1) was born December 8, 1929, in New Castle, Pennsylvania. He received a bachelor of science at Baltimore City College in the early 1950s. He then served in the United States Army at Fort Monmouth, New Jersey, where his responsibilities included loading and unloading cameras and processing film images of ionograms. He was later stationed in the Aleutian Islands, doing similar work. He then took a job at the Environmental Sciences Service Administration (ESSA, later called NOAA) with the US government. That was initially in Washington, DC, but he had the good luck to be quickly transferred to Boulder, Colorado, sometime in the 1950s.

The time at NOAA was very productive. His first visit to the Max Planck Institute for Ionosphere Research (later renamed to "for Aeronomy") in Lindau am Harz, Germany, was for a planning meeting for the International Geophysical Year (1957). Bill used ionosondes as a diagnostic for various chemical release experiments, explosions, and ionospheric heating experiments, in many parts of the world. For example, in the 1960s he operated his sounder to support the National Bureau of Standards (NBS, now NIST) 16 in gun on Barbados, which launched 122-kilogram chemical-release payloads to 180 kilometers. One of his sons commented that "While I lived under his roof, it seemed he was always off to some far-away place."

Bill's aim was to extract as much information as possible from an ionogram (or radio sounding), and in this, he succeeded admirably. In collaboration with others – in particular, M. L. V. Pitteway – he led the development of new sounder systems employing digital computers at NOAA. One example was the "Kinesonde," which finally led to the development in the late 1970s of the "Dynasonde" HF radar, with the additional collaboration of R. N. Grubb. The Dynasonde incorporated many important, advanced features such as frequency agility, phase coherence, well-defined interfaces, and flexible software such that most of these features lasted well into the 21st century. Bill liked the term "research ionosonde" for this instrument as compared to "monitoring ionosonde" for many of the other sounders. A photo (Figure 2) shows Bill in front of the Bear Lake Observatory (Utah) Dynasonde. The Dynasonde in Tromsø still provides top-quality data, thanks to the software developments Bill contributed to over the years. A substantial number of newer sounders were based on the same ideological foundation, and are operated now as Dynasondes to advance our understanding of the complex interactions between the geospheres. The Dynasonde's success is a legacy to Bill's uncompromising aim for perfection.

Bill was awarded a Doctor of Science, honoris causa, from Brunel University ("got doctored," according to Mike Pitteway) on December 1, 1982. Bill remained at NOAA until 1983, when he retired from government service. In June of that year, he moved to the Max Planck Institute for Aeronomy (now Max Planck Institute for Solar System Research), Germany. There, he worked with data from

Figure 2. Bill Wright in front of the Bear Lake Observatory (Utah) Dynasonde

the Dynasonde in Tromsø, used as a diagnostic tool for ionospheric-heating experiments, as well as for studying the complex auroral ionosphere together with the EISCAT incoherent-scatter radars.

Around 1985, he left Lindau for Cambridge (UK), and worked at the British Antarctic Survey. He remained there until July 1989, before returning to Colorado. In the 1990s, after the Dynasondes were converted to PC control and data acquisition, Bill and collaborators further developed Dynasonde analysis with such innovations as phase-based echo detection, vector-velocity determination, all in near real-time. This culminated (with Nick Zabotin) in a true-height electron-density inversion technique allowing for tilted ionospheric layers. From about 2000, Bill was a Research Associate at CIRES, University of Colorado, Boulder. With Nick, he formed Dynasonde Solutions to supply the final analysis package to a new generation of sounders such as the VIPIR HF radar.

Holding strong principles that he vigorously defended, Bill was not afraid to voice his opinion at meetings or in writing, and several of his collaborations did not remain harmonious. He has left behind at least 90 scholarly publications, not counting numerous presentations at meetings, where he was easily recognizable in his characteristically casual attire.

Bill was a well-traveled man who enjoyed life, particularly through music (I remember he was fond of Bach), cycling, walking, and French wine and cheese. He is survived by his third wife, two daughters, two sons-in-law, four sons, and two daughters-in-law.

Michael Rietveld
EISCAT Scientific Association
9027 Ramfjordbotn
Norway
E-mail: mike@eiscat.uit.no

IUCAF 2017 Annual Report

1. Introduction

The Scientific Committee on Frequency Allocations for Radio Astronomy and Space Science, IUCAF, was formed in 1960 by its adhering Scientific Unions, IAU, URSI, and COSPAR, at the behest of URSI. The IUCAF brief is to study and coordinate the requirements of radio-frequency allocations for passive (i.e., non-emitting or receive-only) radio sciences (radio astronomy, space research, and remote sensing), in order to make these requirements known to the national administrations and international bodies that allocate and regulate the use of radio frequencies. IUCAF operates as a standing interdisciplinary committee under the auspices of ICSU, the International Council for Science. IUCAF is a Sector Member of the International Telecommunication Union's Radiocommunication Sector (ITU-R). IUCAF is an observer at the Space Frequency Coordination Group (SFCG). IUCAF is online at http://www.iucaf.org.

2. Membership and Member Affiliations With Other Bodies

IUCAF member Subramaniam Ananthakrishnan expressed a wish to retire at the conclusion of his term as URSI Vice President during the URSI GASS in August 2017. He is to be greatly thanked for nearly 25 years of service to IUCAF. He was replaced by Dr. Haiyan Zhang of the National Astronomical Observatories (Chinese Academy of Sciences), who became the first IUCAF member from China. At the end of 2017, the IUCAF membership elected by the three adhering Unions was as given in Table 1.

Additionally, the Counselor for ITU-R Study Group 7 (Science Services), Mr. Vadim Nozdrin, is an ex-officio member by virtue of his ITU-R position, as specified in IUCAF's terms of reference. IUCAF also has an informal group of Correspondents, in order to improve its global geographic representation and for specific issues, for instance, concerning astronomical observations in the optical and infrared domains.

IUCAF member van Driel chairs CRAF, the European Committee on Radio Astronomy Frequencies of the European Science Foundation (see http://www.craf.eu). The members of CRAF also include Tiplady. Chung is Chair of the Radio Astronomy Frequency Committee in the Asia-Pacific region (RAFCAP), the members of which also include Ohishi, Tzioumis and Zhang (see http://www.atnf.csiro.au/rafcap/). Tzioumis is Chair of ITU-R Working Party 7D (Radio Astronomy). Ohishi, IUCAF's Immediate Past Chair, is the official liaison between the IAU and the ITU. Liszt is a member of the American Astronomical Society's Committee on Light Pollution, Radio Interference, and Space Debris, and a member of the Steering Committee of the IAU Inter-Division Commission C.B4 on Protection of Existing and Potential Observatory Sites. Van Driel is Secretary of IAU Commission B4 on Radio Astronomy and a member of its Organizing Committee.

3. IUCAF's Terms of Reference (2015)

A revision to the statement of IUCAF's composition, operating practices, and Terms of Reference (TOR) was approved by ICSU's Executive Board in 2015: see http://www.iucaf.org/IUCAF_Terms_Of_Reference.pdf.

These originally dated to 1972, when IUCAF was the Inter-Union Committee on Allocation of Frequencies

Table 1. The IUCAF membership elected by the three adhering Unions as of the end of 2017.

URSI	Dr. Haiyan Zhang	China
	Dr. Steven Reising	USA
	Dr. Ingemar Häggström	Sweden
	Dr. Anastasios Tzioumis	Australia
	Dr. Wim van Driel	France
IAU	Dr. HyunSoo Chung	Korea (Republic of)
	Dr. Harvey Liszt (Chair)	USA
	Dr. Masatoshi Ohishi	Japan
	Dr. Adrian Tiplady	South Africa
COSPAR	Dr. Yasuhiro Murata	Japan

Table 2. The regional and international meetings in which IUCAF members participated during January to December 2017.

March	ITU-R Working Party WP 7D	Geneva
May	ITU-R WP 5A, 5B, 5C	Geneva
May	ITU-R TG 5/1	Geneva
May	CRAF-60th meeting	Bonn
June	ITU-R WP 1A, 1B	Geneva
August	URSI GASS + RFI Workshop	Montreal
September	SFCG-37	Montreal
September	ITU-R TG 5/1	Abu Dhabi
October	ITU-R WP 4C	Geneva
October	ITU-R WP 4A	Geneva
October	ITU-R WP 7D	Geneva
November	ITU-R Workshop on WRC-19 Preparation and 90th Anniversary of the CCIR and ITU-R Study Groups	Geneva

4. Spectrum Meetings

During the period from January to December 2017, IUCAF members participated in the regional and international meetings given in Table 2. In addition, IUCAF members participated in numerous national spectrum-management proceedings, working in their capacities as spectrum managers at their observatories.

5. IUCAF Business Meetings

IUCAF held in-person business meetings immediately prior to each of the ITU-R sessions of Working Party 7D in Geneva listed above and at the URSI GASS in Montreal. During the year, IUCAF business is undertaken via e-mail as matters arise.

6. Finances

The IUCAF budget is held at and managed by URSI. As requested by IUCAF, sustaining contributions of €5,000, €2,000, and €1,000 were gratefully received from IAU, URSI, and COSPAR, respectively, for calendar year 2017. Expenses were €5584 in support of IUCAF participation at SFCG-37, ITU-R TG 5/1, and the ITU-R event in November.

7. The IUCAF Role in Protecting Passive Radio Science Services

IUCAF is the global forum where spectrum-management concerns of passive radio services in all ITU-R Regions are regularly addressed in a comprehensive manner. The group is expert in the underlying science, in the spectrum-management needs of the science, and in the workings of the spectrum-regulatory regime that allocates spectrum and makes the rules for spectrum use. IUCAF has been an important contributor to the support of radio astronomy at the ITU-R in Geneva since its inception in 1960, and it provides the interface between radio astronomy and the space-science community. As such, IUCAF is a unique resource, with a long record of contributions. The history of these was recounted by a former IUCAF Chair, Brian Robinson, in "Frequency Allocation: The First Forty Years," *Annual Reviews of Astronomy and Astrophysics*, **37**, 1999, pp. 65-96, available at www.gb.nrao.edu/sd03/talks/40_years.pdf.

8. Contact with ICSU, the IUCAF Sponsoring Unions (IAU, URSI, COSPAR) and Other International Organizations

IUCAF maintains regular contact with its adhering Unions and the parent body, ICSU. These organizations play a strong supporting role for IUCAF, the members of which are greatly encouraged thereby. A report of recent IUCAF activities was requested by ICSU in preparation for the ICSU General Assembly in October 2017, which IUCAF was unable to attend owing to a very unfortunate conflict with activities in Geneva. The report is available online at ftp://ftp.cv.nrao.edu/NRAO-staff/hliszt/ICSU/IUCAF-ICSU_IB_2017_GA_aug2017.docx. A report to URSI was prepared for the GASS ftp://ftp.cv.nrao.edu/NRAO-staff/hliszt/URSI/IUCAF-ReportToURSICouncil2017.docx. IUCAF reported in person to a business meeting of URSI Commission J during the GASS. IUCAF organized a spectrum-management session during the GASS, and members attended the RFI mitigation workshop on the day before the opening. IUCAF accepted its first member from China and its first female member at the GASS.

Pursuing its brief, IUCAF maintains strong links with other passive radio-science communities and with space science, especially the Space Frequency Coordination Group. There, IUCAF is an accredited observer and has encouraged ongoing coordination with operators of high-powered orbiting Earth-mapping radars.

Figure 1. The panel discussion at the 90th anniversary of the CCIR and ITU-R Study Groups, convened during the ITU-R Workshop on WRC-19 Preparation.

As is apparent in the list of meetings in Section 4, most IUCAF activities are ITU-R-related. IUCAF was invited to prepare a written contribution for a special edition of the *ITU News* magazine on the 90th anniversary of the CCIR and ITU-R Study Groups (see https://www.itu.int/en/itunews/Documents/2017/2017-04/2017_ITUNews04-en.pdf. On the occasion of this anniversary, a panel discussion among the authors was convened during the ITU-R Workshop on WRC-19 Preparation, as shown in Figure 1.

9. Publications and Outreach

IUCAF has the Web address http://www.iucaf.org, where some basic information on the organization is reported. IUCAF's main outreach activities, beyond the ITU-R, are related to the spectrum-management schools it holds at intervals of four to five years (the last having been in 2014 in Santiago de Chile), whose contents are available on the Web site. In 2017, an anonymous donor stepped forward to fund the production of an IUCAF-logo fidget spinner that will be distributed at international meetings during 2018.

10. IUCAF Concerns

Most of IUCAF's recent activities have been in preparation for the 2019 March ITU-R 2nd Conference Preparatory Meeting (CPM-2) for WRC-19, as the ITU-R Working Parties finish their draft treaty text before August 2018. IUCAF can then create its customary white paper, giving administrations guidance on how best to protect radio astronomy and space research in the face of the methods proposed to satisfy the various WRC agenda items. IUCAF will also prepare its input to CPM-2 with suggested modifications of the methods and considerations regarding them.

Of particular interest to radio astronomy are these WRC-19 Agenda Items: 1.6 on fixed-satellite service spectrum for global wireless broadband in bands at (broadly speaking) 37 GHz to 43 GHz and 47 GHz to 52 GHz; 1.8 on regulatory means to facilitate entry of the strongly-interfering Iridium L-band satellite phone network into IMO's Global Maritime and Disaster Safety System; 1.12 on Intelligent Transport Systems (car-car, car-roadside and car-roadbed communications); 1.13 on spectrum for 5G wireless mobile broadband in the frequency range 24 GHz to 86 GHz; 1.14 on high-altitude platform systems for wireless broadband; 1.15 for fixed and land mobile service applications at 275 GHz to 450 GHz; and 9.1.9 on fixed service allocations at 51 GHz to 52 GHz. That so many agenda items impact radio astronomy is an indication of the complexities and general level of upheaval associated with accommodating new uses of the radio spectrum in a compatible fashion.

Radio transmitters are proliferating in vast numbers in vehicles of all sorts, in handheld and mobile devices, and on satellites, even at frequencies above 70 GHz. Moreover, transmitter bandwidths are envisaged to increase to multiple GHz. For terrestrial transmitters, radio-quiet zones, remoteness and terrain shielding of radio-astronomy sites may offer some protection, although it is the rare case that a telescope is so secluded that it is not visible from a public road. However, nothing can shield a terrestrial radio telescope from airborne and satellite-born transmitters. In the near future, multiple constellations numbering in the thousands of satellites will make the sky effectively isotropically bright over large swaths of the spectrum that are not specifically allocated for radio astronomy. Outside

the passive service bands, the only clear spectrum looking up may be that which is most congested and difficult to use from the ground because of terrestrial transmitters.

Closer to home, succession planning is still a subject of major concern as the IUCAF membership ages and tight observatory budgets, along with the distraction from research that devotion to spectrum management entails, discourage enlistment of younger radio-astronomy spectrum managers.

11. Acknowledgements

IUCAF is grateful for the organizational and financial support that has been given by ICSU, IAU, URSI, and COSPAR over many years. IUCAF also recognizes the support given by radio-astronomy observatories, universities, and national funding agencies to individual members, allowing them to participate in the important work of IUCAF.

Harvey Liszt, Chair
Charlottesville, Virginia, USA
IUCAF Web site: http://www.iucaf.org
E-mail: iucafchair@iucaf.org

Et Cetera

Tayfun Akgül
Istanbul Technical University
Dept. of Electronics and Communications Engineering
Telecommunications Division
80626 Maslak Istanbul, Turkey
Tel: +90 212 285 3605; Fax: +90 212 285 3565
E-mail: tayfunakgul@itu.edu.tr.

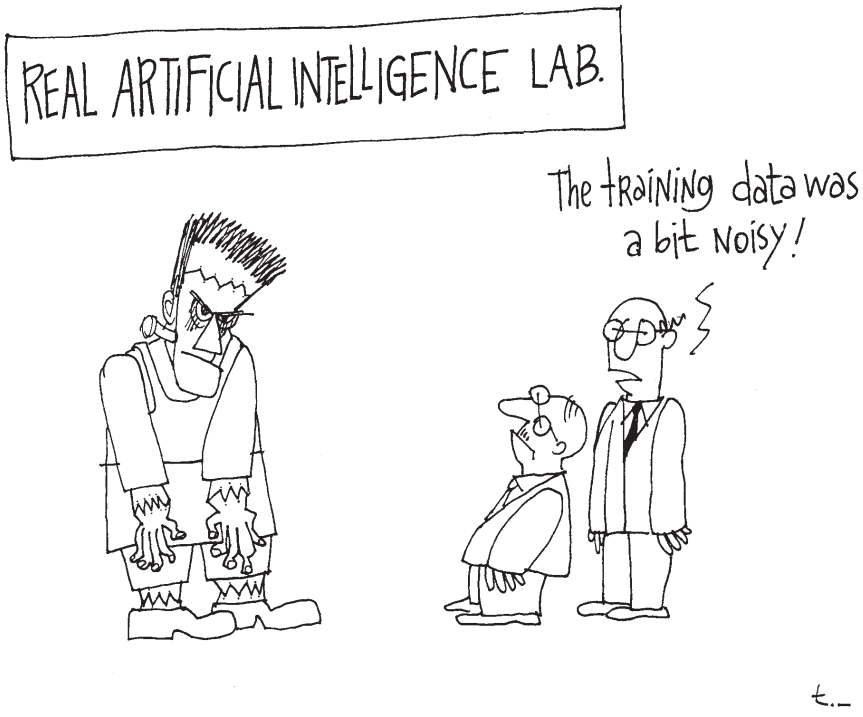
REAL ARTIFICIAL INTELLIGENCE LAB.
The training data was a bit noisy!

Randy L. Haupt
Colorado School of Mines
Brown Building 249
1510 Illinois Street, Golden, CO 80401 USA
Tel: +1 (303) 273 3721
E-mail: rhaupt@mines.edu

Amy J. Shockley
E-mail: aj4317@gmail.com

Price's Law: Haves and Have-Nots

Randy L. Haupt and Amy J. Shockley

There has been a lot of discussion recently about how the rich are getting richer and the poor are getting poorer. This topic is far from new and has spurred political unrest for centuries, including during the French Revolution. A new book [1] that is summarized in a *Time* magazine article [2] provides some statistics and theories about why this gap in social status is widening in the United States. Data from 2015 (Figure 1) display a gap in average household earnings in the United States [3], indicating a clear bias towards a relatively small group of people. In *The Great Gatsby* (which I recently read), F. Scott Fitzgerald wrote, "The rich get richer and the poor get – children!" This phenomenon is called a preferential attachment process: any process that distributes some quantity, typically money or credit, is distributed to individuals or objects according to how much they already possess [4]. Consequently, the wealthy receive more additional money than those who do not have much to begin with.

It turns out that the idea of a few getting almost everything applies to some amazingly diverse scenarios. For instance, the 800 most frequently used words in the English language appear in 80% of all English writing [5]. According to the second edition of the 20-volume *Oxford English Dictionary*, there are definitions for 171,476 English words in current use [6]. In other words (pun intended), 0.47% of all English words are used 80% of the time.

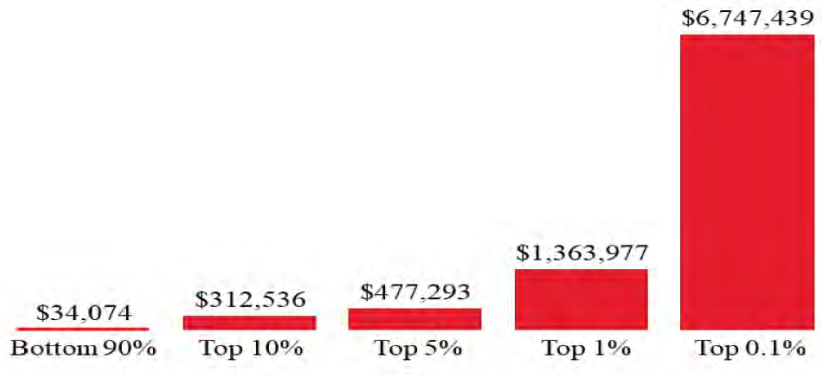

Figure 1. The average household income in the United States for 2015 [3].

Table 1. The number of papers by authors in the 2017 IEEE AP-S/USNC-URSI symposium

Number of papers	9	10	11	12	13	14	15	16
Number of authors	7	4	2	4	1	2	2	1

Several researchers in the late 1800s to mid-1900s discovered that data from the physical and social sciences often follows a power-law probability distribution, which has become known as Zipf's law [7]. Alfred Lotka applied Zipf's law to the frequency of publications by authors in any field of study [8]. The mathematical relationship is given by $Y = C/X^n$, where X is the number of publications, Y is the relative frequency of authors with X publications, and C is a field-dependent constant approximately equal to 2. A version of Lotka's law, called Price's law, states that half of the publications in any given field are produced by the square root of all contributors [9]. As an example, if 25 authors wrote 100 papers, then about five authors contributed approximately 50 of the papers.

Do these laws apply to our publications? IEEE Xplore has some data for the 2017 IEEE AP-S/USNC-URSI Symposium that are listed in Table 1. Of about 1300 papers/abstracts in this conference, 23 of the authors in Table 1 had their names on 260 of the papers/abstracts. In other words, 20% of the papers had the names of 1.8% of the authors. This data are not complete, but do seem to indicate that there is a power-law relationship between the number of authors and the number of papers in one major conference.

While recognizing that researchers publish about their topic of expertise, Price's law might show the separation between communicating an opinion and an agenda. An opinion is a view or judgment about something, whereas an agenda is the underlying intention or motive of a particular person or group. Often times, conclusions are drawn from a set of data, and while many people have an opinion on which conclusion is correct, those with an agenda are often more vocal. It is important as researchers to acknowledge the potential agenda associated with publications, and to provide an outlet for competing interpretations.

We need to be aware of these imbalances in the distribution of things to people. Should the amount of research and development money, salaries, papers, awards, and opportunities in our field be limited to a select few? Or, should it be distributed in a more egalitarian way? Is it even possible to do a fair distribution, or does Price's law prevent it? These questions are not new, and will always be with us. At least we now have an equation to describe and justify the distribution of such things.

References

1. S. Brill, *Tailspin*, New York, Alfred A. Knopf, 2018.

2. S. Brill, "My Generation Was Supposed to Level America's Playing Field. Instead, We Rigged It for Ourselves," *Time*, May 28, 2018, pp. 32-39.

3. E. Saez, "Striking it Richer: The Evolution of Top Incomes in the United States," UC Berkeley, June 30, 2016, available at https://eml.berkeley.edu/~saez/saez-UStopincomes-2015.pdf.

4. https://web.stanford.edu/class/cs224w/slides/handout-powerlaws.pdf, accessed May 5, 2018.

5. http://www.cnusd.k12.ca.us/domain/5563, accessed May 5, 2018.

6. https://en.oxforddictionaries.com/explore/how-many-words-are-there-in-the-english-language/, accessed May 5, 2018.

7. https://en.wikipedia.org/wiki/Zipf%27s_law, accessed May 5, 2018.

8. https://en.wikipedia.org/wiki/Lotka%27s_law, accessed May 5, 2018.

9. https://brainlid.org/general/2017/11/28/price-law.html, accessed May 5, 2018.

Özgür Ergül
Department of Electrical and Electronics Engineering
Middle East Technical University
TR-06800, Ankara, Turkey
E-mail: ozgur.ergul@eee.metu.edu.tr

SOLBOX-11

Muhammed Tonga, Barışcan Karaosmanoğlu, and Özgür Ergül

Department of Electrical and Electronics Engineering
Middle East Technical University
TR-06800, Ankara, Turkey
E-mails: ozergul@metu.edu.tr

1. Introduction

In computational electromagnetics, nonuniform discretizations with a large variety in the sizes of the discretization elements have always been challenging to handle. Such problems are inherently multi-scale, where different regimes coexist, as small elements are used to model tiny details while large elements are used on suitable parts comparable to the wavelength. When the variety in the element size is large, conventional implementations often suffer from inaccuracy, instability, and/or inefficiency issues due to numerical breakdowns in the context of discretization, expansion, and/or matrix solution. As a natural consequence, there is an enormous collective effort in the literature [1-9] to develop accurate, stable, and efficient numerical solvers for multi-scale problems involving nonuniform discretizations.

In the context of three-dimensional surface integral equations for perfect electric conductors, nonuniform triangulations arise when structures with small details (such as antennas, metamaterials, and frequency-selective surfaces) need to be analyzed while the problem size is large due to array configurations, large-scale platforms (on which detailed structures are mounted), and/or nearby bodies. Very small discretizations may also be required for relatively large objects without details, especially when near-zone scattering, radiation, and transmission characteristics need to be investigated. Relaxing the discretization on less critical parts (to reduce the computational load) leads to nonuniform discretizations, while many researchers prefer to keep the element size small to avoid instability at the cost of inefficiency.

In this issue of Solution Box, two sets of scattering problems in the frequency domain (SOLBOX-11), involving increasingly nonuniform discretizations and their sample solutions, are presented. The considered geometries are canonical (sphere and cube) and their nonuniform discretizations may not be required in practice, particularly when far-zone scattering is focused. Nevertheless, they are challenging enough to test alternative implementations and to assess their accuracy, stability, and efficiency. Sample solutions are obtained by using a fully hybrid implementation. As usual, we are seeking alternative solutions, which are probably more accurate, stable, and/or efficient, using other implementations. Please also consider sending your solutions for the earlier problems (SOLBOX-01 to SOLBOX-10) to present your work in this column.

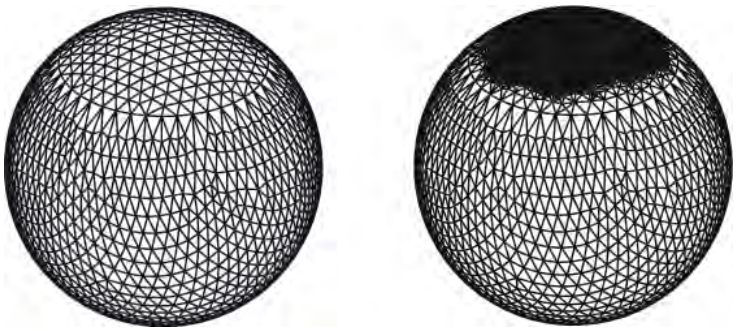

Figure 1. A sphere of diameter 0.6 m with uniform and nonuniform (1:0.16 ratio) triangulations.

2. Problems

2.1 Problem SOLBOX-11

(by *Muhammed Tonga, Barışcan Karaosmanoğlu, and Özgür Ergül*)

The problem SOLBOX-11 includes scattering problems involving two different perfectly conducting objects, i.e., a sphere and a cube, and their different (nonuniform) discretizations. The sphere has a diameter of 0.6 m, and it is investigated at 500 MHz (where the diameter corresponds to the wavelength, λ). It is located at the origin and illuminated by a plane wave (1 V/m) propagating in the *z* direction. In the ordinary (uniform) discretization of the spherical surface, the triangulation size is selected as 3 cm ($\lambda/20$), while the discretization around the north pole is increasingly refined, such as depicted in Figure 1. Three different nonuniform discretizations are considered by selecting the size ratios between the larger and smaller triangles as 1.0:0.16, 1.0:0.075, and 1:0.036. For the most nonuniform discretization (1:0.036), the size of the smaller triangles is hence approximately $\lambda/560$. From the ordinary discretization to the three nonuniform discretizations, the number of unknowns (pairs of triangles) changes from 4479 to 17,532, 70,392, and 290,211.

The setup for the cube problems is similar. The 0.6 m × 0.6 m × 0.6 m conducting cube is located at the origin and illuminated by a *z*-propagating plane wave (1 V/m) at 500 MHz. In addition to the ordinary discretization with 7.5 cm ($\lambda/8$) triangles, the mesh is progressively refined at two corners, such as depicted in Figure 2. For nonuniform discretizations, the ratios between the sizes of the larger and smaller elements are selected as 1.0:0.16, 1.0:0.075, and 1.0:0.036, leading to 10,650, 32,883, and 79,779 unknowns, respectively. The ordinary (uniform discretization) involves only 1308 unknowns.

The discretized models (triangles and node coordinates) are available upon request (e-mail: bariscankaraosmanoglu@gmail.com). It is desired to solve the scattering problems described above at a single frequency (500 MHz). Finding the current coefficients (or alternative represents of the induced current distributions) is sufficient, while the sample solutions below present far-zone scattered fields.

3. Solution to Problem SOLBOX-11

3.1 Solution Summary

Solver type (e.g., noncommercial, commercial): Noncommercial research-based code developed at CEMMETU, Ankara, Turkey

Solution core algorithm or method: Frequency-domain fully hybrid Multilevel Fast Multipole Algorithm (MLFMA)

Programming language or environment (if applicable): *MATLAB + MEX*

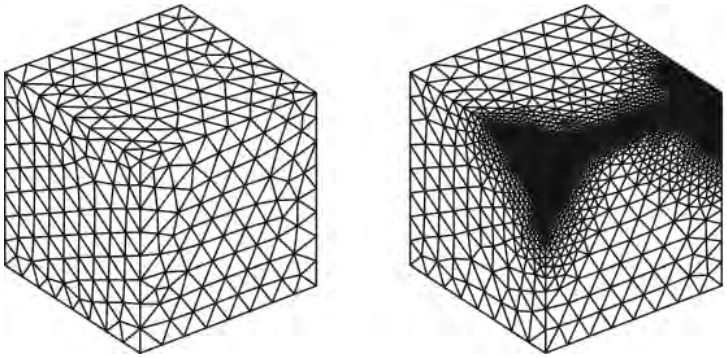

Figure 2. A cube with edges of 0.6 m with uniform and nonuniform (1:0.1 ratio) triangulations.

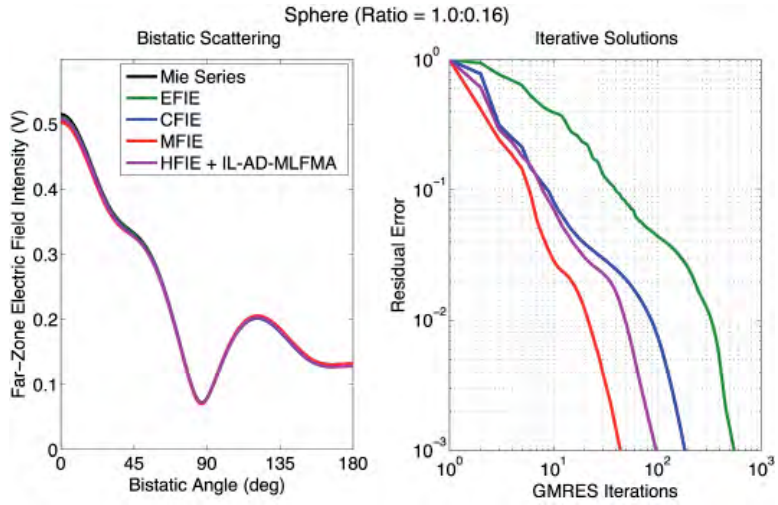

Figure 3. Different solutions of the sphere problem (SOLBOX-11) using nonuniform discretization with 1.0:0.16 ratio (17,532 unknowns).

Computer properties and used resources: 2.5 GHz Intel Xeon E5-2680v3 processors (using single core)

Total time required to produce the results shown (categories: < 1 sec, < 10 sec, < 1 min, < 10 min, < 1 hour, < 10 hours, < 1 day, < 10 days, > 10 days): < 1 minute for the ordinary discretizations (4479 and 1308 unknowns) and < 1 day for the largest problems (290,211 and 79,799 unknowns)

3.2 Short Description of the Numerical Solutions

The scattering problems listed under SOLBOX-11 were solved by using a fully hybrid implementation in the *MATLAB* environment. Hybridization was performed at all parts of the implementation as follows:

- Formulation: A hybrid formulation [10] was used by applying the combined-field integral equation (CFIE) on suitable regions with large discretization elements, while the magnetic-field integral equation (MFIE) was employed on regions with fine discretizations. The regions were selected automatically, i.e., the magnetic-field integral equation was used when a triangle was smaller than half of the largest element. The resulting hybrid-field integral equation (HFIE) was discretized by using the Rao-Wilton-Glisson (RWG) [11] functions.

- Solver: A multi-scale MLFMA structure was used to efficiently solve nonuniform discretizations. We note that an ordinary MLFMA is based on a recursive clustering with collective division of boxes into subboxes [12], which becomes significantly inefficient for nonuniform discretizations. Specifically, keeping the number of levels small to avoid protrusions of discretization elements from boxes may lead to quadratic complexity due to the reduced sparsity of near-zone matrices. To avoid such inefficiencies, incomplete-leaf (IL) tree structures [7, 9] were used.

- Expansion of interactions: In MLFMA, the standard diagonalization using plane waves fails as some boxes become very small in comparison to the operation wavelength. For sub-wavelength boxes, alternative wave-expansion schemes [3, 4, 6, 13] that are stable for short distances are therefore needed if the complexity of MLFMA is desired to be kept at linearithmic levels. While there are alternative methods [14-16], we used approximate diagonalization (AD) of the Green's function [17] that was particularly suitable for the magnetic-field integral equation, which we already used for small discretization elements.

Solutions obtained via the hybrid implementation (that we also call HFIE + IL-AD-MLFMA) were compared to those obtained by using a three-level standard MLFMA employing the conventional combined-field integral equation, the electric-field integral equation (EFIE), and the magnetic-field integral equation formulations discretized with the RWG functions. All electromagnetic interactions (near-zone and far-zone) were computed with a maximum 1% error. All solutions were performed by using the generalized minimal residual (GMRES) method, while the target residual error was selected as 0.001.

3.3 Results

Figure 3 presents different solutions of the sphere problem using nonuniform discretization with a 1.0:0.16 ratio (17,532 unknowns). On the left-hand side, the far-zone electric field intensity (V) was plotted with respect to the bistatic angle on the E-plane. In the plot, 0° and 180° corresponded to forward-scattering and back-scattering, respectively. We observed that solutions obtained with HFIE + IL-AD-MLFMA, the electric-field integral equation, the combined-field integral equation, and the magnetic-field integral equation were consistent with each other, as well as with the analytical Mie-series solution. Iterative solutions were depicted on the right-hand side, where the residual error was plotted with respect to GMRES iterations for

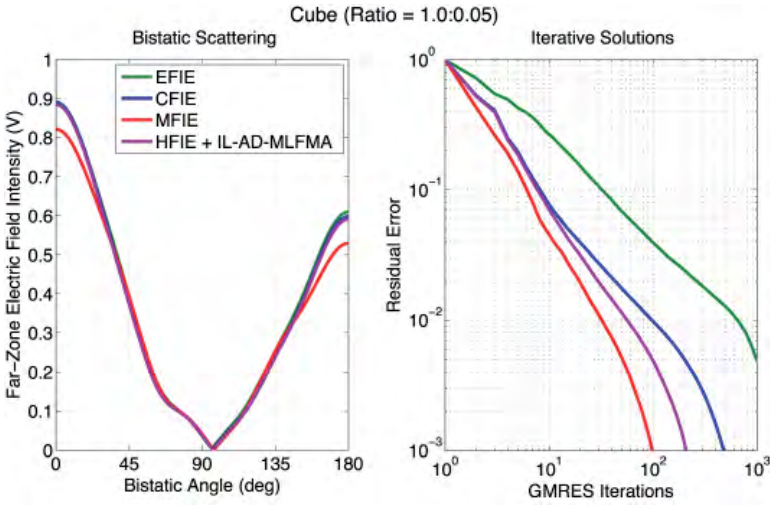

Figure 4. Solutions of the sphere problems (SOLBOX-11) using the hybrid formulation (HFIE + IL-AD-MLFMA).

different implementations. We observed that the hybrid implementation needed fewer iterations (98) than the combined-field integral equation (185) and the electric-field integral equation (547), while the magnetic-field integral equation provided the quickest convergence with 45 iterations. On the other hand, although it was not visible in this case, solutions with the magnetic-field integral equation were prone to interior-resonance problems that made this formulation less reliable. We also noted that in terms of the total time, the hybrid implementation (881 seconds) was even faster than the magnetic-field integral equation (1086 seconds), thanks to the incomplete-leaf tree structure. The problems became more challenging as the triangulation became more nonuniform (1.0:0.075 and 1.0:0.0367 discretization ratios) and the number of unknowns grew such that the magnetic-field integral equation (or the combined-field integral equation and the electric-field integral equation) solutions become infeasible and are not shown.

Figure 4 presents the solutions of all sphere problems (including the uniform discretization) using the hybrid formulation. We observed that accurate results could be obtained without a breakdown even for the extremely nonuniform discretization with 1.0:0.0367 ratio. The numbers of GMRES iterations required for solutions were 38 (uniform), 98 (1.0:0.16 ratio), 153 (1.0:0.075 ratio), and 228 (1.0:0.036 ratio). We emphasize that these iteration counts were without preconditioning, and they might be reduced with suitable preconditioners. For the largest problem with 290,211 unknowns, the total processing time was 21 hours on a single core.

Next, in Figure 5, we present different solutions of the cube problem using nonuniform discretization with 1.0:0.05 ratio (32,883 unknowns). Similar to the plots in Figure 3, the far-zone electric field intensity is shown with respect to the bistatic angle, in addition to the corresponding iteration histories. In this case, the conventional magnetic-field integral equation provided visibly inconsistent (inaccurate) results, which may have been caused by an interior resonance or the well-known inaccuracy of the magnetic-field integral equation for sharp geometries [18]. Despite containing the magnetic-field integral equation on finely

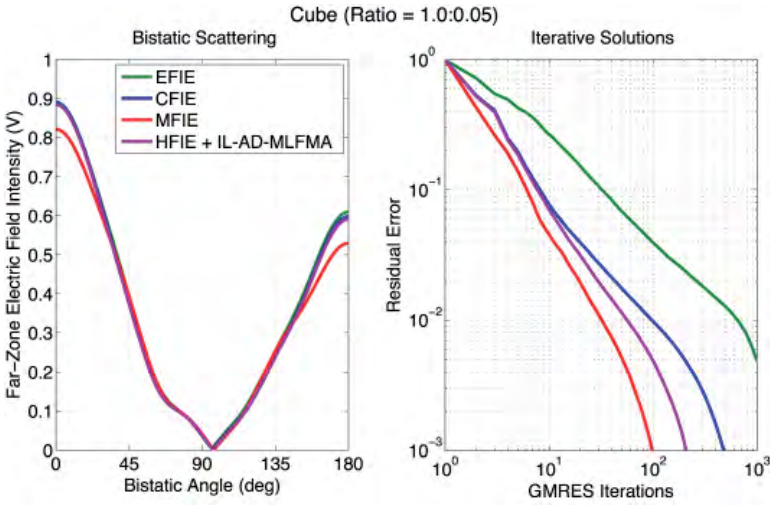

Figure 5. Different solutions of the cube problem (SOLBOX-11) using nonuniform discretization with 1.0:0.05 ratio (32,883 unknowns).

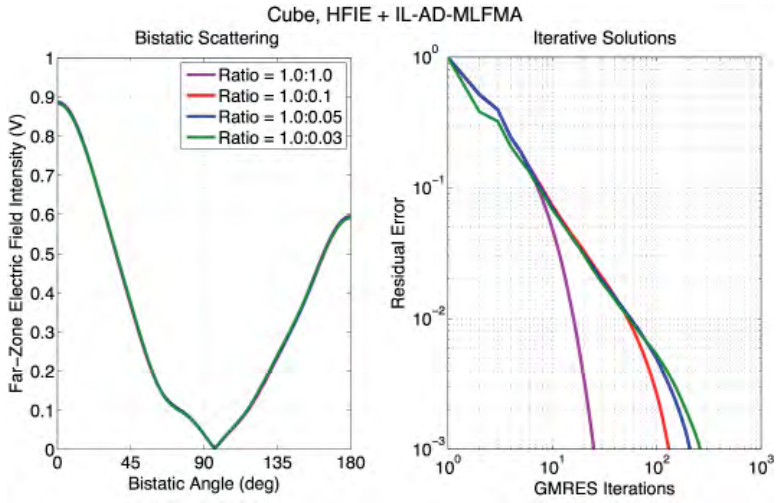

Figure 6. Solutions of the cube problems (SOLBOX-11) using the hybrid formulation (HFIE + IL-AD-MLFMA).

discretized regions (corners), the hybrid implementation was consistent with the electric-field integral equation and combined-field integral equation, verifying its accuracy. Investigating the plot of iterative solutions, we observed that the hybrid implementation required 209 iterations, which was significantly smaller than 475 for the combined-field integral equation and above 1000 for the electric-field integral equation. We noted that despite requiring 98 iterations, the accuracy of the magnetic-field integral equation may not have been acceptable.

Finally, Figure 6 presents the solutions of all cube problems using the hybrid formulation. We observed the high consistency of scattering results obtained with uniform and nonuniform discretizations. The numbers of iterations were 25 (uniform discretization), 131 (nonuniform discretization with 1.0:0.1 ratio), 209 (nonuniform discretization with 1.0:0.05 ratio), and 262 (nonuniform discretization with 1.0:0.03 ratio). For the largest problem (1.0:0.03 ratio) involving 79,779 unknown, the solution required less than six hours.

4. References

1. F. Vipiana, P. Pirinoli, and G. Vecchi, "A Multiresolution Method of Moments for Triangular Meshes," *IEEE Trans. Antennas Propagat.*, **53**, 7, July 2005, pp. 2247-2258.

2. M.-K. Li and W. C. Chew, "Multiscale Simulation of Complex Structures Using Equivalence Principle Algorithm with High-Order Field Point Sampling Scheme," *IEEE Trans. Antennas Propagat.*, **56**, 8, August 2008, pp. 2389-2397.

3. M. Vikram, H. Huang, B. Shanker, and T. Van, "A Novel Wideband FMM for Fast Integral Equation Solution of Multiscale Problems in Electromagnetics," *IEEE Trans. Antennas Propagat.*, **57**, 7, July 2009, pp. 2094-2104.

4. X.-M. Pan, J.-G. Wei, Z. Peng, and X.-Q. Sheng, "A Fast Algorithm for Multiscale Electromagnetic Problems Using Interpolative Decomposition and Multilevel Fast Multipole Algorithm," *Radio Sci.*, **47**, 1, February 2012, pp. 1-11.

5. H. Shao, J. Hu, Z. Nie, and L. Jiang, "Simulation of Multiscale Structures Using Equivalence Principle Algorithm with Grid-Robust Higher Order Vector Basis," *J. Electromagn. Waves Appl.*, **28**, 11, June 2014, pp. 1333-1346.

6. J.-G. Wei, Z. Peng, and J.-F. Lee, "Multiscale Electromagnetic Computations Using a Hierarchical Multilevel Fast Multipole Algorithm," *Radio Sci.*, **49**, 11, November 2014, pp. 1022-1040.

7. M. Takrimi, Ö. Ergül, and V. B. Ertürk, "A Novel Broadband Multilevel Fast Multipole Algorithm with Incomplete-Leaf Tree Structures for Multiscale Electromagnetic Problems," *IEEE Trans. Antennas Propagat.*, **64**, 6, June 2016, pp. 2445-2456.

8. D. M. Solis, F. Obelleiro, and J. M. Taboada, "Surface Integral Equation-Domain Decomposition Scheme for Solving Multiscale Nanoparticle Assemblies with Repetitions," *IEEE Photonics J.*, **8**, 5, October 2016.

9. M. Takrimi, Ö. Ergül, and V. B. Ertürk, "Incomplete-Leaf Multilevel Fast Multipole Algorithm For Multiscale Penetrable Objects Formulated with Volume Integral Equations," *IEEE Trans. Antennas Propagat.*, **65**, 9, September 2017, pp. 4914-4918.

10. B. Karaosmanoğlu and Ö. Ergül, "Generalized Hybrid Surface Integral Equations for Finite Periodic Perfectly Conducting Objects," *IEEE Antennas Wireless Propag. Lett.*, **16**, October 2017, pp. 1068-1071.

11. S. M. Rao, D. R. Wilton, and A. W. Glisson, "Electromagnetic Scattering by Surfaces of Arbitrary Shape," *IEEE Trans. Antennas Propagat.*, **30**, 3, May 1982, pp. 409-418.

12. Ö. Ergül and L. Gürel, *The Multilevel Fast Multipole Algorithm (MLFMA) for Solving Large-Scale Computational Electromagnetics Problems*, New York, Wiley/IEEE, 2014.

13. W. C. Chew, J.-M. Jin, E. Michielssen, and J. Song, *Fast and Efficient Algorithms in Computational Electromagnetics*, Norwood, MA, Artech House, 2001.

14. L. J. Jiang and W. C. Chew, "A Mixed-Form Fast Multipole Algorithm," *IEEE Trans. Antennas Propagat.*, **53**, 12, December 2005, pp. 4145-4156.

15. I. Bogaert, J. Peeters, and F. Olyslager, "A Nondirective Plane Wave MLFMA Stable at Low Frequencies," *IEEE Trans. Antennas Propagat.*, **56**, 12, December 2008, pp. 3752-3767.

16. Ö. Ergül and B. Karaosmanoğlu, "Low-Frequency Fast Multipole Method Based on Multiple-Precision Arithmetic," *IEEE Antennas Wireless Propag. Lett.*, **13**, May 2014, pp. 975-978.

17. Ö. Ergül and B. Karaosmanoğlu, "Broadband Multilevel Fast Multipole Algorithm Based On an Approximate Diagonalization of the Green's Function," *IEEE Trans. Antennas Propagat.*, **63**, 7, July 2015, pp. 3035-3041.

18. Ö. Ergül and L. Gürel, "Discretization Error Due to the Identity Operator in Surface Integral Equations," *Comput. Phys. Comm.*, **180**, 10, October 2009, pp. 1746-1752.

James C. Lin
University of Illinois at Chicago
851 South Morgan Street, M/C 154
Chicago, IL 60607-7053 USA
E-mail: lin@uic.edu

Peer Review Conclusion of Clear Evidence of Cancer Risk from Cell-Phone RF Radiation

On March 26 to 28, 2018, the National Institute of Environmental Health Sciences' (NIEHS) National Toxicology Program (NTP), a part of the US National Institutes of Health (NIH), convened a three-day Technical Reports Peer Review Panel meeting in Research Triangle Park, NC, to review the NTP's draft reports on their carcinogenesis studies of cell-phone radio-frequency (RF) radiation in mice and rats [1]. The invited 14-member peer-review panel included three electrical engineering professors, 10 pathologists and toxicologists (three from academia and seven from industry), and one biostatistician; none were from the cell-phone industry.

This project is the largest NTP animal cancer study ever. It was nominated by the Food and Drug Administration (FDA) in 1999. The supposedly five-year project was sole-sourced in 2004 to an industrial research firm as the project's principal investigator. The work began in 2005. However, the project had been protracted for more than a dozen years with huge budget overruns, and an estimated eventual price tag of $25 million [2, 3].

From the outset, NIEHS/NTP had decided to be tight-lipped about it, and did not release any progress reports or any information. In contrast to scientific norm, project investigators had not openly discussed any of its aspects, or made any presentations of its progress or interim findings at scientific meetings. The first report from the project was in May 2016, when NTP came out and announced occurrences of two types of rare cancers in exposed rats: malignant schwannomas of the heart and gliomas in the brain [4]. However, that announcement spoke only to partial findings from their two-year (or lifelong) exposure study of rats subjected to 900/1900 MHz RF radiation involving CDMA and GSM wireless cellular telephone operations.

On March 28, 2018, following a thorough review of the draft NTP reports, pathologists and toxicologists on the peer-review panel concluded, among other observations, that there is statistically significant and "clear evidence" that both GSM- and CDMA-modulated RF radiation had led to the development of malignant schwannoma, a rare form of tumor in the heart of male rats (of Harlan-Sprague-Dawley strain), and there was "equivocal evidence" for the same schwannoma risk among female rats. The panel also noted that there were unusual patterns of cardiomyopathy, or damage to heart tissue, in both RF-exposed male and female rats compared with concurrent control animals.

In addition, based on statistical significance the panel concluded that the pathology findings showed indications of "some evidence" for RF-dependent carcinogenic activity in the brain of male rats, specifically glioma. However, the findings for female rats were deemed as providing only "equivocal evidence" for malignant gliomas compared with concurrent controls.

The NTP uses five categories of evidence of carcinogenic activity to classify the strength of evidence

observed in their reports: "clear evidence" and "some evidence" for positive findings; "equivocal evidence" for uncertain results; "no evidence" for no observable effects; and "inadequate study" for results that cannot be evaluated because of major experimental flaws.

The so-called reverberation chamber (RC) method and technology were employed for RF exposure. The exposure regime included 10-min-on and 10-min-off for 19 h per day for two years. Rats were exposed for a total of 9 h each day to cell-phone RF radiation. Whole-body-average RF absorption rates (SAR) of 0, 1.5, 3, or 6 W/kg did not raise body temperature of exposed animals to more than 1°C. The study was successful in its aim to provide maximum uniformity of exposure. In particular, the reported local SARs in the brains and hearts of rats were only 1.05 and 2.27 times the whole-body-average SARs, respectively. Indeed, most tissues and organs inside the rats' bodies had experienced similar SARs from RF exposure.

It is well known that the NTP cell-phone RF exposure study is by far the largest study of its kind [5]. It was rather expensive and took a long time to get to this point. There may even be better ways to do the study. Nevertheless, the study points up the fact that prolonged exposures to RF radiation at levels that are similar to, or a little above, the currently existing RF exposure regulations could lead to tumor development.

Note that the current RF exposure guidelines of 1.6 or 2.0 W/kg are promulgated with a reduction factor of 50, as a safety margin for the general public, to provide protection against presumed hazardous biological effects in humans [5, 6]. The finding that RF exposure could lead to dose-dependent cancer development at levels that are the same or at three times above current exposure guidelines is significant.

This implies that the safety margin may be no more than a factor of three. In fact, one recommendation (IEEE C95.1-2005) has a set of guidelines under controlled environments that would allow local SARs of the brain and heart to be as much as 10 W/kg [7]. A SAR of 10 W/kg is considerably higher than the 1.5, 3.0, and 6.0 W/kg used in the NTP study.

The FDA should be applauded for nominating, and NIEHS/NTP should be lauded for having sponsored, the research and conducted the Cell Phone Radio Frequency Radiation (RFR) Studies. It is important for the US government to step in to conduct such a research program, and to not leave the matter entirely to the cell-phone industry. The wireless industry has had nearly free reign to develop and roll out cellular mobile phones and related RF devices as they see fit. The completion of this NTP study should not signify the end of the US government's role in supporting RF biological effects research, because we all are being exposed to increasingly more and more RF radiation every day [8, 9].

Moreover, a systematic review of 59 published studies of controlled exposure to RF radiation with health-related outcomes [10] showed that public agencies or charities funded 11 (19%), the wireless communications industry funded 12 (20%), mixed sources (including industry) funded 14 (24%), and in 22 cases (37%), the source of funding was not reported. Research funded exclusively by industry reported the largest number of outcomes, but were least likely to report a statistically significant result compared with studies funded by public agencies or charities. This finding was not altered when analysis was adjusted for the number of outcomes reported, study quality, or other factors.

As for the NTP study, the reverberation-chamber method and technology were employed for exposure of rats and mice to cell-phone RF radiation. Descriptions in the report of what was implemented are fairly clear, and measurement techniques are accurate to the extent they were applied. However, there are limitations.

It appears that the reverberation chamber was selected *a priori* for the project. It is not clear whether the reverberation chamber is the optimal technology for the project, or whether other competing technologies, such as circular waveguides or small rectangular multimodal chambers, were seriously considered for exposure of freely moving animals inside the holding cage.

The large number of reverberation chambers specifically constructed for this project is the most expensive one-time use of single-purpose equipment or facility for RF biological effects research. They likely would not be used for another project; thus the reverberation chambers would end up as "white elephants" by default, if they have not been scrapped already. (It appears that NIEHS/NTP has moved on to other types of exposure chambers to continue its biological-effects research regarding RF exposure.)

The study could have been better designed. There were obvious flaws concerning the experimental design involving reverberation chambers for RF exposure. A question arose during the panel meeting concerning the unusually small number of concurrent control animals. The NTP study used the same concurrent control animals for both GSM and CDMA exposure groups. The "designer" and the same person who had "sole-sourced" this $25-million NTP study to an industry contractor responded to the query with a not-enough-space answer: the contractor only had space for 21 reverberation chambers. Only one reverberation chamber was thus available for sham or concurrent control. This begs the question of what the rationale was for choosing to sole-source the contractor as principal investigator for the project. The availability of facilities and space to conduct the study should be top priorities in any list of criteria for awarding such a contract! Any allusion to saving money for a couple more reverberation chambers in a $25-million project, such as the use of round plastic bottles instead of rat-shaped experimental phantoms, sounds like a rather feeble excuse. The NTP project easily could have saved a

lot more money if the 21 large reverberation chambers were not produced and transported from Zurich, Switzerland over land, ocean, and river to Chicago for reassembly.

The small number of concurrent control rats renders it more challenging to reliably show that experimental findings are statistically significant, especially when multiple comparisons are involved. Was the small number of concurrent controls an integral part of the design for this large animal cancer study to start with?

This experimental-design question brings up the matter of control animals for a closer examination. In bioassay research involving animals, there are normally two types of controls: cage controls and sham controls. In cage controls, animals are housed in the vendor's open-stack vivarium, subjected only to routine house-keeping and handling protocols. They are not subjected to any of the proposed experimental treatments or manipulations. In principal, they could include data from control animals used in prior NTP studies.

In sham controls, referred to as concurrent control, animals are subjected to the same protocols, RF apparatus, and environment, except without being subjected to treatment by the experimental agent, in this case, RF exposure.

It appears that the NTP study design had planned to use "historical controls" for statistical comparisons. Historical controls may come from the animal breeder or supplier for the strain of rats used: Harlan-Sprague-Dawley. In this case, it was derived from NTP's in-house control data with this strain of rats, which were not subjected to treatment by any exogenous test agent. However, NTP's experience with this strain of rats was not long or extensive: a few two-year studies over five to 10 years. More importantly, the life history of these historical control rats was quite different from the concurrent controls involved in the RF study.

Instead of NTP facilities in Research Triangle Park, NC, the RF study took place in Chicago, where both sham-control and exposed animals were housed in custom-designed and constructed reverberation chambers. The reverberation-chamber environment is totally different from the NTP animal facilities. Aside from one-of-a-kind sealed, shielded, steel chambers with piped-in ambient sonic noise and air through specially designed inlets and outlets, animal access to food and water were delivered using ingenious and unique systems.

Furthermore, the reverberation chambers used incandescent light bulbs instead of the fluorescent lamps that were commonly used in the past. Fluorescent and incandescent lighting have different color and temperature properties. Fluorescent lamps do not produce the continuous spectrum of light that is characteristic of incandescent bulbs. It should be noted that RF radiations (100 ± 50 kHz) are emitted by fluorescent lamps when in operation, because of the starter electrodes and electronic switching ballast in them.

Clearly, given the above-mentioned issues, the historical controls from past NTP studies are not appropriate for statistical comparison in this RF exposure study. The review panel opted to base their evaluation and conclusion on the concurrent control data. Nevertheless, for reference purposes, historical control data for the Harlan Sprague-Dawley strain and from NTP are an important source of information as background material.

In addition to malignant schwannomas in heart tissue and, to some degree, gliomas in the brains of male rats, the review panel concluded that there was "some evidence" for carcinogenicity in the adrenal gland. The number of pheochromocytomas, a tumor of the adrenal gland, was significantly higher ($p < 0.05$) in male rats at 1.5 W/kg and 3 W/kg, compared with the concurrent controls. The increase in malignant tumor-like hyperplasia in the adrenal gland of female rats was also significantly higher at 6.0 W/kg, relative to the concurrent controls ($p < 0.05$).

There were also findings of "equivocal evidence" for carcinogenicity in other tissues or organs, such as adenoma of pars digitalis in the pituitary gland, and adenomas and carcinomas in the liver of both RF-exposed male and female rats.

The key exposure metric chosen was the whole-body-average SAR. Reports from the NTP study indicated that an RF field uniformity within 10% was achieved throughout the reverberation-chamber volume [1, 11]. This level of field uniformity enabled similar SAR values throughout the rats' bodies. Specifically, the local SAR in the brains and hearts of rats were a mere 1.05 and 2.27 times the whole-body-average SAR, respectively. This means that tissues and organs inside the rat's body had experienced similar SARs from GSM and CDMA RF exposures.

Since all tissues and organs were similarly exposed and had similar SARs, it is important for the NTP team to perform a statistical comparison of total primary malignancies in all tissues and organs observed in RF-exposed and concurrent control rats before issuing its final report. Given that hyperplasia often leads to neoplasm, the statistical analysis should also include findings of hyperplasia. (Hyperplasia is the enlargement of tissues or organs caused by increased rate of growth of its cells in the initial stage of cancer development.)

The World Health Organization's International Agency for Research on Cancer (IARC) had classified exposure to RF radiation including those used for cell phones as possibly carcinogenic to humans [12]. IARC had assessed available scientific papers and concluded that while evidence was incomplete and limited, especially with regard to results from animal experiments, epidemiological studies reporting increased risks for malignant gliomas and

acoustic neuromas among heavy or long-term users of cell phones are sufficiently strong to support a classification of RF exposure possibly causing cancer in humans. Note that acoustic neuromas are also known as acoustic schwannomas, a non-malignant tumor of Schwann-cells-sheathed auditory nerves on the side of the brain.

It is remarkable to note the complete absence of histopathological results from the inner ear or auditory nerve tissue in the NTP RF study. This is totally unacceptable and may speak volumes to the inadequacies and flaws of the study as it was designed.

The significance and necessity for histopathological examinations of tissue specimens surrounding the auditory nerve should have been a clear priority because of the role acoustic schwannomas played in IARC's possible carcinogenic classification of cell-phone RF radiation. In any case, it is hoped that NTP has preserved or has access to pertinent histological materials to allow them to go back and examine them with regard to acoustic schwannomas.

What is even more startling to note is that malignant schwannoma in rat hearts were the most salient findings from the NTP RF bioassay. While acoustic schwannomas in human brains and malignant schwannomas in rat hearts were independently observed from two different body tissues in humans and rats, there actually could be a link in that Schwann cells wrap around both nerve tissues in the heart and along the auditory nervous system.

Now that the NTP review panel has concluded that there is clear evidence of carcinogenicity from long-term RF exposure in rats, is it conceivable that IARC would upgrade its epidemiology-based classification of RF exposure to the next higher levels of carcinogenicity to humans?

It is noteworthy that the existing RF exposure guidelines of 1.6 or 2.0 W/kg are promulgated with a reduction factor of 50, as a safety margin for the general public. The finding that long-term RF exposure could lead to cancer development in rats at levels that are the same or no more than a factor of three above these exposure guidelines is significant.

While complacencies abound for the short-term exposure guidelines in providing safety protection, an outstanding question persists on the adequacy of these guidelines for safe long-term exposure to RF radiation at or below 1.6 or 2.0 W/kg. Perhaps the time has come to judiciously reassess, revise, and update these guidelines.

References

1. NTP Draft Reports, Public Comments, and Related Information: TR Peer Review Panel, https://ntp.niehs.nih.gov/about/org/sep/trpanel/meetings/docs/2018/march/index.html, accessed April 26, 2018.

2. J. C. Lin, "*Changing the Conversation* on Cell Phone RF Radiation Carcinogenesis," *IEEE Microwave Magazine*, **17**, 10, 2016, pp. 21-23; Comment and Response, *IEEE Microwave Magazine*, **18**, 1, 2017, p. , 138.

3. J. C. Lin, "The NTP Cell Phone Radio Frequency Radiation Health Effects Project," *IEEE Microwave Magazine*, **18**, 1, 2017, pp. 15-17.

4. M. Wyde, M. Cesta, C. Blystone, S. Elmore, P. Foster, M. Hooth, G. Kissling, D. Malarkey, R. Sills, M. Stout, N. Walker, K. Witt, M. Wolfe, and J. Bucher, "Report of Partial Findings from the National Toxicology Program Carcinogenesis Studies of Cell Phone Radiofrequency Radiation in Hsd: Sprague Dawley Rats (Whole Body Exposure)," bioRxiv, doi: http://dx.doi.org/10.1101/055699, May 26, 2016.

5. FCC, "Wireless Devices and Health Concerns," https://www.fcc.gov/consumers/guides/wireless-devices-and-health-concerns, accessed on February 21, 2016.

6. ICNIRP, "Guidelines for Limiting Exposure to Time-Varying Electric, Magnetic, and Electromagnetic Fields (Up to 300 GHz)," *Health Physics*, **74**, 1998, pp. 494-522.

7. IEEE, *IEEE Std. C95.1, Standard for Safety Levels with Respect to Human Exposure to Radio Frequency Electromagnetic Fields, 3 kHz to 300 GHz*, New York, IEEE Press, 2005.

8. J. C. Lin, "Human Exposure to Radio Frequency, Microwave and Millimeter Wave Electromagnetic Radiation," *IEEE Microwave Magazine*, **17**, 6, June 2016, pp. 32-36.

9. J. C. Lin, "Cancer Occurrences in Laboratory Rats from Exposure to RF and Microwave Radiation," *IEEE Journal of Electromagnetics, RF and Microwaves in Medicine and Biology*, **1**, 1, 2017, pp. 2-13.

10. A. Huss, M. Egger, K. Hug, K. Huwiler-Müntener, and M. Röösli, "Source of Funding and Results of Studies of Health Effects of Mobile Phone Use: Systematic Review of Experimental Studies," *Environ Health Perspect*., **115**, 2007, pp. 104.

11. M. E. Wyde, T. L. Horn, M. H. Capstick, J. M. Ladbury, G. Koepke, P. F. Wilson, G. E. Kissling, M. D. Stout, N. Kuster, R. L. Melnick, J. Gauger, J. R. Bucher, and D. L. McCormick, "Effect of Cell Phone Radiofrequency Radiation on Body Temperature in Rodents: Pilot Studies of the National Toxicology Program's Reverberation Chamber Exposure System," *Bioelectromagnetics*, **39**, 2018, pp. 190-199.

12. IARC Working Group on the Evaluation of Carcinogenic Risks to Humans, "Non-Ionizing Radiation, Part 2: Radiofrequency Electromagnetic Fields," *IARC Monographs on the Evaluation of Carcinogenic Risks to Humans*, **102 (Pt. 2)**, 2013, pp. 1-460.

Women in Radio Science

Asta Pellinen-Wannberg
Umeå University, Department of Physics and
Swedish Institute of Space Physics
S-90187 Umeå, Sweden
Tel: +46 90 786 7492
E-mail: asta.pellinen-wannberg@umu.se

Early Career Representative Column

Stefan J. Wijnholds
Netherlands Institute for Radio Astronomy
Oude Hoogeveensedijk 4
7991 PD Dwingeloo, The Netherlands
E-mail: wijnholds@astron.nl

In this joint column, it is our great pleasure to put Prof. Jamesina Simpson in the spotlight. On the occasion of the triennial General Assembly and Scientific Symposium (GASS) of URSI in August 2017, Jamesina was awarded the Santimay Basu Prize (Figure 1). This prize is awarded to a young scientist who has made an outstanding contribution to research that furthers the understanding of radiowave propagation in random media and its applications for the benefit of society. The award takes into account the excellence of the research, the merit of the candidate in achieving his or her results, and the efforts required to accomplish the research. The Santimay Basu Prize was presented to Prof. Jamesina Simpson with the citation, "For advancing three=dimensional finite-difference time-domain (FDTD) solutions of electromagnetic wave propagation within the global Earth-ionosphere waveguide applied to space weather, remote-sensing, and very-low-frequency propagation."

Jamesina (Figure 2) obtained her PhD in Electrical Engineering from Northwestern University in Evanston, Illinois, in 2007. Her dissertation was on "3-D Finite-Difference Time-Domain (FDTD) Modeling of Impulsive Electromagnetic Propagation in the Global Earth-Ionosphere Waveguide below 30 kHz." Her PhD advisor was Prof. Allen Taflove, a very inspiring and encouraging supervisor. From August 2007 to June 2012, Jamesina was a tenure-

Figure 1. The Santimay Basu Prize being presented to Prof. Jamesina Simpson (r) by Prof. Paul Cannon during the opening ceremony of the URSI GASS 2017 in Montreal, Canada.

track Assistant Professor in the Electrical and Computer Engineering (ECE) Department at the University of New Mexico. In July 2012, she joined the ECE Department at the University of Utah as an Associate Professor. Her research lab encompasses the application of FDTD to modeling electromagnetic phenomena at frequencies over 15 orders of magnitude (~1 Hz to ~600 THz). In particular, Jamesina's group has pioneered the most advanced three-dimensional Maxwell's equations FDTD models of global electromagnetic wave propagation within the Earth-ionosphere waveguide. These models have been applied to a variety of applications, such as remote sensing of oil fields, geolocation, hypothesized electromagnetic earthquake precursors, remote sensing of localized ionospheric anomalies, Schumann resonances, and space-weather effects on the operation of electric power grids.

Figure 2. Jamesina Simpson.

Besides being an excellent researcher, she is also an excellent educator, as for example indicated by the IEEE Antennas and Propagation Society Donald G. Dudley, Jr., Undergraduate Teaching Award presented to her in 2012. In this column, she reflects on her own years in college and the supervision she received from Prof. Taflove. She identifies three factors (cultivating a growth mindset, building grit and enhancing creativity) that (would) have helped her overcome challenging times, and how this has become part of her professional and personal life.

Reflections on Personal Development

Jamesina J. Simpson

Alfred Binet, the inventor of the IQ test, wrote the following summary in his book, *Modern Ideas about Children* [1]:

> A few modern philosophers…assert that an individual's intelligence is a fixed quantity, a quantity which cannot be increased. We must protest and react against this brutal pessimism….With practice, training, and above all, method, we manage to increase our attention, our memory, our judgment and literally to become more intelligent than we were before.

In the United States, it is common to consider an IQ score the limit of a person's unchangeable intelligence. Binet considered our IQ level more of a starting point rather than an end point. As an educator, this is a refreshing thought! Essentially, the sky is the limit for any student who enters my office or class. I can help them to achieve more than they may have ever thought possible.

Some people remark how "lucky" my PhD advisor, Prof. Allen Taflove, is at graduating women PhD students who go on to become professors (still rather rare in electromagnetics (EM) today). I argue that it is not luck at all. I believe it is because Prof. Taflove holds a growth-personality mindset (more on this below), and because he gives students unending encouragement and support. These attributes at least certainly helped me to achieve more than I ever thought possible while in his lab.

At the time that I started studying EM at Northwestern University as an undergrad, I had zero knowledge of Maxwell's equations, the foundation of my current research area today (computational EM). Further, at the time I was only in the School of Engineering because I was supposedly "good in math" and I didn't know what else to pursue (veterinary science, my previous interest, was out because I had nearly fainted while observing a surgical operation on a dog). I had never considered graduate school, and unfortunately I had just earned a 2.7 GPA during my first quarter following a difficult transition to college life.

Looking back, I feel there were three key factors that helped me to get back on track after that challenging quarter. These factors have also helped me in my career. Had I been able to understand these three factors earlier, I believe I would have overcome difficult times more often and more easily (such as whenever a paper or proposal is inevitably rejected!):

Figure 3. Learning to play the violin.

1. Cultivating a growth mindset
2. Building grit
3. Enhancing creativity

Cultivating a Growth Mindset

I grew up learning to play the violin through the Suzuki method (Figure 3). Although I knew I wouldn't pursue music professionally, I continued to play into college. Years later, I would finally realize all the benefits I had gained from it. For example, when I recently started to teach my children to play violin, I learned that the Suzuki method is more: I realized it is as much about playing the violin as it is a philosophy for life.

Through the Suzuki method, I learned how to help my daughter overcome challenges rather than just give up. When she balks at learning a new passage in a song because it's "too hard!" I help her to break up the passage into much shorter segments (even of just three notes). After mastering all of the shorter segments, she can piece them all together and surprise herself by suddenly playing the entire passage.

In fact, the more I learned about the Suzuki method, the more I realized that I am cultivating in my child what author Dr. Carol Dweck calls a "growth mindset" [2]. When an obstacle is overwhelming, we can try to break it up into more manageable portions in order to make progress and still work towards our goals. As another example, to be able to reliably perform in a concert without making mistakes we should practice our performance piece exactly as we will play it in a concert at least three times a day for several weeks, so that much of the performance becomes automatic. The list goes on. In other words, there is always something we can do to help make hard things easier.

In her book, *Mindset: The New Psychology of Success* [2], Dr. Carol Dweck summarizes two general mindsets that people tend to have. If you have a fixed mindset, you believe that your qualities are carved in stone, and that you have to prove yourself over and over. On the other hand, if you have a growth mindset, you believe that you can cultivate your abilities through hard work.

I believe that by exercising and strengthening my growth mindset over the years through Suzuki training and through other means this has helped me immensely in my studies and in my career. When I earned a C in my advanced math class in that freshman year, instead of thinking "I'm not good at math," I remember thinking that I needed to find a better way to learn that material. Later, in graduate school, I ended up earning A's in much more advanced math classes. In my career, when my teaching scores were not as high as I had hoped, I worked hard at learning, tweaking, and improving my teaching style each time around. My teaching scores inched up, and I have since earned teaching awards and have been listed in the top 15% of teachers college-wide at the University of Utah. It's rewarding to look back at how far I've come since being scared to death of my first teaching assignment!

Building Grit

Although I grew up playing classical music on the violin from a young age, only recently did I learn more about what made Mozart successful [2, p. 56]:

> Mozart labored for more than ten years until he produced any work that we admire today. Before then, his compositions were not that original or interesting. Actually, they were often patched-together chunks taken from other composers.

Indeed, Mozart worked so hard that "by the time he was twenty-eight years old, his hands were deformed because of all of the hours he had spent practicing. That's the missing element in the popular portrait of Mozart" [3].

In other words, Mozart had high levels of two key ingredients: a high level of perseverance (e.g., the ability to overcome setbacks to conquer an important challenge), as well as strong passion (e.g., the ability to become obsessed with a certain idea or project for a long period of time). High levels of these two ingredients resulted in Mozart having a high score on the "grit scale," developed by author Angela Duckworth. It turns out that having a high level of grit is

a better predictor of success than just about anything else (pure talent, IQ score, SAT score, etc.) [4].

I believe I started to build perseverance when I had to practice my violin every day for years on end, starting at a young age. I probably further gained perseverance when I started running track and cross country in high school, and later trained for a marathon four years ago. Knowing how to work hard in one area makes it easier to work hard in another area.

In my career, passion and perseverance have helped me to develop one of the world's most advanced electrodynamics models of EM wave propagation in the global Earth-ionosphere waveguide. My students and I are currently advancing and utilizing these models to study space-weather hazards to electric power grids (preventing blackouts), locate airplanes that have crashed into the ocean, and help develop a ground-based global positioning system, to name a few applications.

Enhancing Creativity

As a student, I was always in awe of my PhD advisor. He always came up with more and more ideas. At the time, I understood that to come up with new ideas you at least must have a broad and thorough knowledge of prior art so you can find ways to improve and build on past accomplishments. However, I was not aware that our ability to create new ideas can be strengthened using various strategies and techniques.

In the book *The Creative Habit*, Twyla Tharp [3] argues that creativity is not a magical act of inspiration. It's the result of hard work and dedication. In some cases, following a "ritual of preparation" may help spark ideas. For example, Beethoven would start each day with a morning walk, during which he would scribble into a small sketchbook the first rough notes of whatever musical idea entered his head.

We should not think that Beethoven was developing ideas out of thin air, however. We might improve our ability to be creative after a ritual of preparation by "scratching" for ideas. "Scratching is what you do when you can't wait for the thunderbolt to hit you" [3]. You can scratch for ideas by reading, having conversations with coworkers or even strangers, examining previous work by others, and by immersing yourself in nature. For example, Beethoven was an avid bird lover, and would get musical motifs from listening to birds. Similarly, in the engineering world, butterfly wings have inspired metamaterial structures for manipulating light.

I never thought of myself as an especially creative person, but I'm starting to complete the exercises in Tharp's book to help give myself ideas on how I might improve my ability to create. I also know I should make time for scratching for ideas even during the busiest of times (which can be challenging while raising two small children).

Conclusion

I've never taken an IQ test, and I don't feel the need to find out what it is. I find it much more uplifting to know more about the growth mindset, grit, and strategies to become more creative. Not only can I continually work to improve, adapt, and tweak my own capabilities, but I can help students, my own children, and other people understand that they, too, can succeed in challenging majors, careers, or whatever other endeavors they may embark upon. This is, to me, what makes my life and career rewarding: having meaningful work in which I may help individuals in my life, while also developing and creating new engineering ideas to potentially help society at large.

References

1. A. Binet, *Modern Ideas About Children*, Menlo Park, CA, Susan Heisler, 1975.

2. C. S. Dweck, *Mindset: The New Psychology of Success*, New York, Random House, 2006.

3. T. Tharp, Twyla, *The Creative Habit: Learn It and Use It For Life*, New York, Simon and Schuster, 2003.

4. A. Duckworth, *Grit*, New York, Simon and Schuster, 2016.

INTERNATIONAL SYMPOSIUM ON ELECTROMAGNETIC THEORY (EMTS 2019)

May 27-31, 2019, San Diego, CA, USA

First Call For Papers

The International Symposium on Electromagnetic Theory (EMTS 2019) will be held May 27-31, 2019, in San Diego, CA, USA. It is organized by Commission B (Fields and Waves) of the International Union of Radio Science (URSI), and is financially cosponsored by the United States National Committee for URSI (USNC-URSI) and the IEEE Antennas and Propagation Society (IEEE AP-S). EMTS 2019 is the 23rd event in the triennial series of international EMT symposia, which has a long history since 1953. Its scope covers all areas of electromagnetic theory and its applications. It is the major scientific event of Commission B, along with the URSI General Assembly and Scientific Symposium, Atlantic Radio Science Conference (AT-RASC), and Asia Pacific Radio Science Conference (AP-RASC). The venue is the hotel Westin San Diego, which is minutes from downtown activities including the San Diego Zoo, Balboa Park and its numerous museums, and the Gaslamp district for dining and nightlife. San Diego is the eighth largest city in USA, and is often referred to as "America's Finest City." Known for its great hotels, beautiful weather, pristine beaches, friendly people, and a plethora of entertainment, San Diego is a favorite destination for visitors across the globe. The San Diego airport is conveniently close to our symposium venue, so transportation to the conference will be quick and easy.

Welcome to San Diego in May 2019! The conference will offer plenary talks by distinguished speakers, regular oral and poster sessions, and a one-day school for young scientists (May 27), focusing on a topic in electromagnetics. A number of Young Scientist Awards will be offered, covering the registration fee and accommodation during the conference. In addition, business meetings, receptions, and a conference banquet will be organized. EMTS 2019 will focus on electromagnetic fields and their applications. Contributions on any aspect of the scope of Commission B are solicited. Some suggested topics are listed below. Special-session topics will be listed later on the Web site. All submissions (two to four pages in IEEE two-column format) will be reviewed by the Commission B Technical Advisory Board. Accepted and presented papers may be submitted to IEEE Xplore.

Important dates

- Paper submission site opens: July 15, 2018
- Deadline for paper submission: **October 22, 2018**
- Notification of acceptance: January 10, 2019
- Early-bird and author registration ends: March 30, 2019

Contact: Technical Program: Kazuya Kobayashi <kazuya@tamacc.chuo-u.ac.jp>
Local Organizing Committee: Sembiam Rengarajan <srengarajan@csun.edu>

Suggested Topics

1. Electromagnetic theory
- Analytical and semi-analytical methods
- Mathematical modeling
- Canonical problems
- Scattering and diffraction
- Inverse scattering and imaging

2. Computational methods
- Integral equation methods
- Partial differential equation methods
- High-frequency and hybrid methods
- Fast solvers and high-order methods
- Time-domain techniques
- Computational algorithms

3. Materials and wave-material interaction
- Metamaterials and metasurfaces
- Plasmonics and nanoelectromagnetics
- Electromagnetic bandgaps and other periodic structures
- Optical devices
- EMC and EMI
- Bioelectromagnetics

4. Antennas and propagation
- Antenna theory
- Antenna measurements
- Multi-band and wideband antennas
- Antenna arrays and MIMOs
- Wireless communication systems
- Guided waves and structures
- Random media and rough surfaces
- Millimeter wave/5G propagation
- Millimeter-wave antennas
- MIMO for 5G communication

5. Other topics
- History of electromagnetics
- Education in electromagnetics

www.emts2019.org

Report on the 8th VERSIM

General Information

The 8th biennial Workshop on VLF/ELF Remote Sensing of Ionospheres and Magnetospheres (VERSIM) was held on March 19-23, 2018, in Apatity (Murmansk region, Russia). The conference was hosted by the Polar Geophysical Institute (PGI). The meeting Web site was at http://pgi.ru/conf/versim2018.

Participants

The workshop was attended by 42 participants with the following countries of affiliation: Russia, 19 (including 6 from PGI); Finland, 5; Japan, 5; Hungary, 5; Czech Republic, 3; USA, 3; France, 1; UK, 1.

Abstracts and Sessions

In total, 64 abstracts were accepted. Of those, 10 were canceled after acceptance for various reasons. 50 oral and four poster reports were finally presented. Each oral talk was given a 20-minute time slot, including invited reports. Posters were also briefly (five minutes each) presented during a single time slot. The following session themes were identified, being held in sequence:

- D-region phenomena and propagation in the Earth-ionosphere cavity;
- Wave propagation in E and F regions;
- ELF and VLF waves related to lightning discharges;
- New instruments and results of specific measurements;
- Magnetospheric ELF/VLF phenomena;
- Radiation-belt dynamics (not only related to ELF/VLF waves);
- Laboratory modeling of cyclotron wave-particle interactions.

The radiation-belt session was included in the program following the successful experience of the 7th VERSIM workshop.

Scientific Highlights

In the order of their presentation, a number of specific highlights were identified from the given talks which included:

- Measurements of VLF wave propagation at long and short distances and advanced numerical modeling allow one to improve characterization of D-region disturbances and location of wave exit areas from the magnetosphere.
- ELF/VLF activity produced by thunderstorm discharges is related to the discharge type.
- Theoretical modeling of VLF wave propagation and absorption explains U-shape spectra observed by DEMETER mission.
- Advanced data-analysis methods, such as the neural network approach, make it possible to dig new findings out of large databases.
- New observations of VLF auroral hiss reveal correlations with geomagnetic storm activity.
- Similarity between properties of quasi-periodic VLF emissions and ELF equatorial noise was revealed.
- Transformer saturation due to geomagnetically induced currents may be diagnosed by VLF measurements.
- Novel conjugate ground-spacecraft observations of various types of VLF emissions
- Advanced use of whistlers and man-made signals observed onboard a spacecraft for diagnosing the magnetospheric plasma density.
- Radiation-belt codes rely upon empirical models of wave activity, and existing models still do not yield satisfactory operation of the codes when compared with real data.
- Laboratory experiments on resonant wave-particle interactions have reached remarkable success in confirming basic physical features.

URSI Financial Support

The URSI Board of Officers provided sponsorship for the workshop in an amount of EUR 1700. This financial support was used for partially supporting four young scientists and PhD students, and two invited scientists, as detailed in the separate financial report.

Next Workshop

The next workshop will be held in 2020, according to the biennial scheme. During the business meeting on March 23, 2018, the participants encouraged Prof. Yoshiharu Omura to organize the VERSIM-2020 workshop in Japan, in accordance with his proposal.

Educational and General Outreach Activities

Both local, regional, and federal media paid attention to the meeting. An article was published in an Apatity newspaper 2x2 (online version is at http://gazeta2x2.ru/?p=78651). An interview about the conference and its science topics was broadcasted over the Murmansk region on March 27 (http://murman.tv/news_radio/60781-dobroe-utro-zapolyare-ot-27-marta.html, from 26m55s to 34m55s). The same commentary was broadcasted over federal Mayak radio (http://murman.tv/news_radio/60837-specialnyy-reportazh-na-mayake-ot-27-marta.html).

An overview of the workshop will be placed and kept at the Web page (http://pgi.ru/conf/versim2018), including the final program, the electronic abstract collection, the group photo, and links to press releases.

Student Competition

According to IAGA recommendations and usual VERSIM practice, we have organized a competition between the young scientists eligible as candidates for the IAGA Young Scientist Award, "in order to identify outstanding and promising persons whose research, presentation and overall performance at the topical meeting meet high international standards and represent big potential for the future of IAGA." Six eligible candidates attended the meeting. Their talks were identified to the audience before being presented, and the science committee members collected their impressions. After the conference, there was a discussion among the science committee followed by a vote. All reports were rated as very good or excellent. The winner, Dr. Evgenii Shirokov (IAP RAS, Nizhny Novgorod, Russia) was declared during the VERSIM business meeting held on Friday, March 23, 2018, from 14:20 to 15:20 MSK.

Excursions

A choice of excursions was offered to the participants:

- Ecostrovskaya recreation facility (nature viewing, husky ride, pilaf, hot wine);
- Kirovsk Museum Center (http://en.mvc-apatit.ru/)
  - historical & geological excursion;
  - multi-media tower tour from the bowels of the Earth to the atmosphere;
- Snow village and ice sculptures gallery (https://vk.com/snowderevnya);
- Art-park "Mystery Forest" (nature viewing, https://vk.com/tainaforest).

Only two guests decided to restrict themselves to only slope skiing, while many others used the opportunity to attend several excursions, one after another.

János Lichtenberger
E-mail: lityi@sas.elte.hu

Andrei Demekhov
E-mail: andrei@ipfran.ru

35th National Radio Science Conference

The 2018 35th National Radio Science Conference (NRSC 2018) was held in Cairo, Egypt, March 20-22, 2018. The conference was jointly organized by the National Radio Science Committee of the Egyptian Academy of Science and Scientific Research & Technology and the Misr International University (MIU), Cairo, Egypt. The following are some of the NRSC2018 conference highlights.

The opening session of NRSC2018 was held in the main Hall of the Tolip Golden Plaza Hotel, Cairo. The VIP guests included Prof. Amro Farouk, Vice President of Egypt's Academy of Scientific Research & Technology (ASRT); Mr. Mohamed El-Rashidy, President of the Board of Trustees of MIU, the conference's honorary chair; and Prof. AbdelRazik Sebak from the University of Concordia, Canada. A photo of the main desk during the formal opening is shown in Figure 1.

Figure 2 shows some of the main speakers at the opening session. Prof. Hesham El-Badawy, General Secretary of NRSC, introduced the event (Figure 2a). Prof. El-Khamy, Chair of NRSC2017, gave a briefing on the efforts that had made done during the past year to enable the conference to be in its distinguished form for the 35th time (Figure 2b). Mr. Mohamed El-Rashidy, President of the Board of Trustees of MIU, gave a briefing on the efforts and facilities that were supplied by MIU to support the NRSC2018 (Figure 2c).

The Vice President of ASRT praised the efforts of the National Radio Science Committee, NRSC, especially in maintaining the NRSC for 35 consecutive times in different universities and research institutes in Egypt. After his talk, Prof. Amro Farouk was presented with an honor by the conference honorary chair, Mr. El-Rashidy, and the NRSC president, Prof. El-Khamy, as shown in Figure 3.

Figure 1. The formal opening ceremony of NRSC 2018: (r-l) Prof. El-Sayed Saad, conference Vice Chair; Prof. Hassan ElGhitany, conference Co-Chair and Dean of Engineering at MIU; Prof. Said El-Khamy, conference Chair and President of Egypt's NRSC; Prof. Amr Farouk, Vice President of ASRT; Mr. Mohamed El-Rashidy, President of the Board of Trustees of Misr International University (MIU).

Following the tradition of the NRSC conference series, four pioneers of radio science in Egypt were honored and their contributions to radio theory and practice were acknowledged. They were Prof. Hassan Elkamchouchi (Alexandria University), Prof. Salwa El-Ramly (Ain Shams University), Prof. El-Sayed Saad (Helwan University), and Prof. Dr. Hany Fikry (Ain Shams University). Figures 4a-4c show three of the radio science pioneers receiving their honors.

Figure 5 is a memorial photo of Egypt's National Radio Science Committee (NRSC) members with the local organizing committee from MIU and some of the VIP guests.

The conference attracted researchers, students, and academic staff from different universities and research

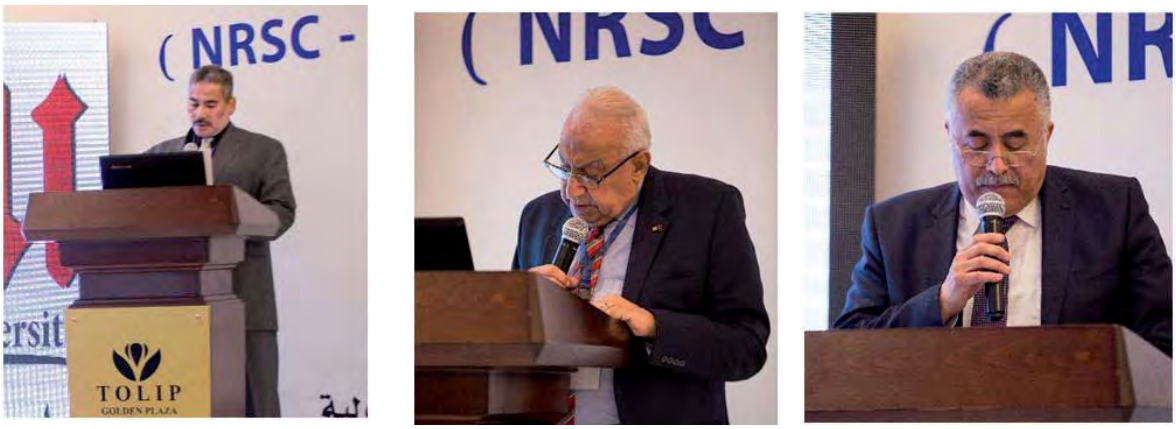

Figure 2. Opening ceremony speeches: (a) Prof. Hesham El-Badawy, General Secretary of NRSC; (b) Prof. Said El-Khamy; (c) Mr. Mohamed El-Rashidy.

Figure 3. Honoring the ASRT Vice President: (r-l) Prof. El-Khamy, Prof. Amr Farouk, and Mr. El-Rashidy.

institutes in Egypt. The authors came to participate and attend this highly prestigious scientific gathering. NRSC2018 was attended by more than 200 scientists and specialists from different universities and research institutions from various Egyptian regions. The contributors to NRSC2018 not only included Egyptian researchers, but NRSC2018 also had some papers that were coauthored by people from international universities.

To the pleasant surprise of the conference organizers, a good turnout of contributions was achieved, where a total of 153 technical research papers were submitted. The selection of the papers was a challenging and difficult task. The program committee members put in a significant effort in order to provide useful feedback to the authors, with an acceptance ratio of 40.5% of the submitted papers. Following a rigorous refereeing process whereby each submitted paper was blindly evaluated by three independent reviewers, only 62 papers were included in the conference program.

According to the NRSC conference processing criteria, all submitted papers were checked for plagiarism with the IEEE similarity checker. They were checked again after modifications based on the reviewers' comments, before including them in the final accepted list. The final 62 accepted papers were distributed among four URSI

Figure 5. The NRSC members with the local organizing committee of NRSC2018 and some of the VIP guests. Prof. AbdelRazik Sebak is in the middle of the upper row.

Figure 4. Honoring Egyptian radio-science pioneers: (a) Prof. Salwa El-Ramly, (b) Prof. Hany Fikry, (c) Prof. El-Sayed Saad.

Commissions as follows: Commission B, 14 papers; Commission C, 26 papers; Commission D, 14 papers; and Commission K, 8 papers. For the second time in the NRSC conference series, all accepted papers (62 papers) were presented and no abstention was recorded.

The conference proceedings will be available on IEEE Xplore.

Following the tradition of the NRSC conference series, three invited talks by distinguished keynote speakers were presented. These were as follows:

Figure 6. Keynote speakers: (a) Prof. Abdel-Razik Sebak, (b) Prof. Salah A. Obayya, (c) Prof. Medhat Mokhtar.

- The first keynote speaker was Prof. AbdelRazik Sebak (IEEE Fellow, Electrical and Computer Engineering, Concordia University, Montreal, Canada), shown in Figure 6a. The title of his talk was "FSS Techniques for Antennas Performance Enhancement and RCS Reduction."

- The second keynote speaker was Prof. Salah A. Obayya (IET Fellow, Electrical and Computer Engineering, Zewail University, Egypt), shown in Figure 6b. His talk was entitled "Computational Photonics: Essentials, Recent Developments, and Future Perspectives."

- The third keynote speaker was Prof. Medhat Mokhtar (Past Chair of the National Authority of Remote Sensing and Space Science), shown in Figure 6c. His talk was entitled "Egyptian Space Agency: The Gateway to National Prosperity."

Figure 7. Dr. Amro Safwat, ITAC-ITIDA manager, during his talk in the Industry Activity session.

This year, a new activity was started in the NRSC conference series: having an industrial activity session to discuss the link between radio-science research and industry. This year, the industrial session invited Dr. Amro Safwat, Manger of the Information Technology Industry-Academia Collaboration (ITAC) program of the Information Technology Industry Development Agency (ITIDA). He highlighted some success stories of funding joint industry-academia projects, as well as other activities of ITAC. Figure 7 Shows Dr. Amro Safwat giving his talk.

To encourage the students and young radio scientists, 22 graduation-project posters were selected for presentation at the conference. The poster sessions were very crowded by the conference participants, session chairs, NRSC committee members, and other students from MIU, BUE, AASTMT, Alexandria University, and other educational institutions. A snapshot from the poster session is shown in Figure 8.

Following the NRSC tradition, five papers received awards: two best paper awards, in addition to three best student paper awards. As usual, URSI contributed 500 Euros towards the best student paper awards. It was worth noting

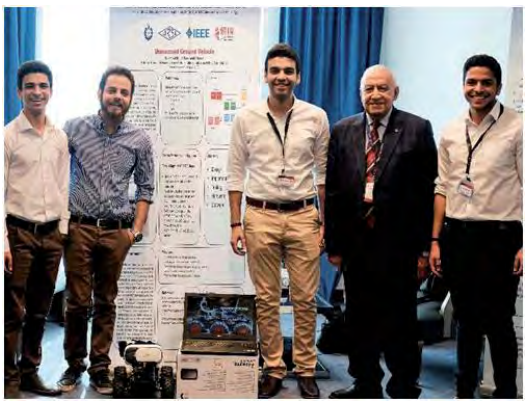

Figure 8. A snapshot from the poster sessions.

Figure 9. Prof. El-Sayed M. Saad, Chair of the Awards Committee, Prof. Said El-Khamy, and Prof. Hesham El-Badawy handing the awards to (a) Amr Ghoname, (b) Mina Saleh, (c) Doaa Azzam, and (d) Marwa El-Sherif.

that all of the papers that received awards were coauthored and presented by graduate students or young scientists. Figures 9a-9d show the awardees receiving their awards. The winning papers were as follows:

Best Paper Awards:

1. "Omnidirectional Optical MEMS Scanner Based on Two Degree-of-Freedom Translation of Acylindrical Micromirrors," by Amr Ghoname, Ashraf Mahmoud, Yasser Sabry, and Diaa Khalil, Faculty of Engineering, Ain Sham Cairo, Egypt.

2. "Low Cost Portable Blood Urea Nitrogen Analyzer Using Odroid System," by Mina Saleh, Ahmed Agamieh, Ahmed Seddik, and Yehya H. Ghallab, Helwan University, Cairo, Egypt.

Best Student Paper Awards:

1. "Phase-Only Pattern Synthesis for Sunflower and Conformal Arrays with Shaped Radiation Patterns," by Doaa Azzam, Hend A. Malhat, and Saber H. Zainud-Deen, Faculty of Electronic Engineering, Menoufia University, Menouf, Egypt.

2. "Fully Generalised Spatial Modulation," by Mohamed Elsayed, Hany S. Hussein, and Usama Sayed, Faculty of Engineering, Souhag University, Souhag, Egypt.

3. "Chaos-Based Image Hiding Scheme Between Silent Intervals of High Quality Audio Signals Using Feature Extraction and Image Bits Spreading," by Marwa H. El-Sherif, Said E. El-Khamy, and Noha O. Korany, Faculty of Engineering, Alexandria University.

For the second time at the NRSC conferences, student graduation projects were evaluated, and 11 of them received recognition awards. Figure 10 is a memorial photo of all winning student teams with their advisors, along with members of the Awards Committee.

Said El-Khamy, President of Egypt's NRSC Committee, NRSC2018 Chair
E-mail: said.elkhamy@gmail.com
Hesham El-Badawy, Secretary General of Egypt's NRSC
E-mail: heshamelbadawy@gmail.com

Figure 10. A memorial photo of all winning student poster teams with their advisors and members of the Awards Committee.

European School of Antennas 2018

ESoA Board

ANTENNAS FOR SPACE APPLICATIONS
ESTEC - Noordwijk, March 12-16
Coordinator: L. Salghetti

MICROWAVE IMAGING AND DIAGNOSTICS
UMED-UNITN,
Madonna di Campiglio, March 19-23
Coordinators:, A. Massa, T. Isernia

RADAR 2020
KIT- Karlsruhe, May 7-11
Coordinator: W. Wiesbeck

CHARACTERISTIC MODES: THEORY AND APPLICATIONS
UPV-Valencia May 14-18
Coordinators, M. Ferrando, P Hazdra,

ADVANCED MATHEMATICS FOR ANTENNA ANALYSIS
UNIZAG - Dubrovnik, May 21-25
Coordinators: Z. Sipus, S. Maci

TERAHERTZ TECHNOLOGY AND APPLICATIONS
UPC - Barcelona, May 28-June 1
Coordinators: L. Jofre, A. Raisanen, N. Llombart

COMPACT ANTENNAS FOR SENSOR SYSTEMS
UPC - Barcelona, June 4-8
Coordinators: L. Jofre, A. Skrivervik

ADVANCED MATERIALS FOR ANTENNAS
LBORO-NCSRD Athens, June 18-22
Coor: Y. Vardaxoglou, A. Alexandridis

MILLIMETER WAVE ANTENNAS
UR1 - Rennes, July 2-6
Coordinators: A. Sharaiha, O. Lafond

ARRAYS AND REFLECTARRAYS
UCL – Louvain La Neuve, Sept. 3 -7
Coordinator: C. Craeye

ADVANCED COMPUTATIONAL EM
POLITO, Torino, Sept. 10 - 14
Coordinators: F. Andriulli, G. Vecchi

ANTENNA SYSTEM INTEGRATION AND PACKAGING
KUL, Leuven- September 17-21
Coord. G. Vandenbosh, U. Johansen, in cooperation with the MSCA H2020 Project SILIKA

SHORT RANGE RADIO PROPAGATION
UNIBO - Bologna, September 24-28
Coordinators: T. Kuerner, C. Oestges, F. Fuschini

ENERGY HARVESTING AND WIRELESS POWER TRANSFER FOR RFID AND WIRELESS SENSOR NETWORKS
HWU, Edinburgh- October 8-12
Coord. G. Goussetis, A. Georgiadis

Joined EuMA-ESoA Course

5G PHASED ARRAYS
TuDelft, NL, 25-29 June 2018
Coordinator: Alexander Yarovoy

ESoA Coordinator Prof. Stefano Maci
Dept. of Information Engineering and Mathematics
University of Siena, 53100 - Siena (Italy)
E-mail: macis@ing.unisi.it

www.esoa-web.org

http://www.facebook.com/europeanschoolofantennas

URSI Conference Calendar

March 2018

Gi4DM 2018
Kyrenia, Turkish Republic of Northern Cyprus, 14-18 March 2018
Contact: K2 Conference and Event Management Kosuyolu Mh. Ali Nazime Sk. No: 45 Kosuyolu 34718 Kadikoy / Istanbul Phone: +90 (216) 428 95 51 - Fax: +90 (216) 428 95 91 E-mail: gi4dm@k2-events.com, http://www.gi4dm2018.org

8th VERSIM Workshop
Apatity, Russia, 19-23 March 2018
Contact: Dr. Andrei Demekhov andrei@appl.sci-nnov.ru
http://www.iugg.org/IAGA/iaga_ursi/versim/

Geolocation and navigation in space and time
The URSI-France 2018 Workshop
Paris, France, 28-29 March 2018
Contact: http://ursi-france.org/

May 2018

Baltic URSI Symposium (part of Microwave Week 2018)
Poznan, Poland, 14-16 May 2018
Contact: Prof. Dr. Andrzej Napieralski, Baltic URSI Symposium 2018 Chairman & Dr Przemysław Sękalski, http://mrw2018.org/ursi2018/national-ursi-2018-topics/

AT-RASC 2018
Second URSI Atlantic Radio Science Conference
Gran Canaria, Spain, 28 May – 1 June 2018
Contact: Prof. Peter Van Daele, URSI Secretariat, Ghent University – INTEC, Technologiepark-Zwijnaarde 15, B-9052 Gent, Belgium, Fax: +32 9-264 4288, E-mail address: E-mail: peter.vandaele@ugent.be, http://www.at-rasc.com

July 2018

COSPAR 2018
42nd Scientific Assembly of the Committee on Space Research (COSPAR) and Associated Events
Pasadena, CA, USA, 14 - 22 July 2018
Contact: COSPAR Secretariat (cospar@cosparhq.cnes.fr)
http://www.cospar-assembly.org

August 2018

Metamaterials 2018
12th International Congress on Artificial Materials for Novel Wave Phenomena
Espoo, Finland, 27-30 August 2018
Contact: http://congress2018.metamorphose-vi.org

September 2018

ICEAA 2018 - IEEE APWC 2018 - FEM 2018
Cartagena de Indias, Colombia
Contact: iceaa18@iceaa.polito.it, http://www.iceaa-offshore.org

October 2018

COMPENG
2018 IEEE Workshop on Complexity in Engineering
Florence, Italy, 10-12 October 2018
Contact: compeng2018@ino.cnr.it , http://compeng2018.ieeesezioneitalia.it/

RADIO 2018
IEEE Radio and Antenna Days of the Indian Ocean 2018
Mauritius,15-18 October 2018
Contact: http://www.radiosociety.org/radio2018/

ISAP 2018
2018 International Symposium on Antennas and Propagation
Busan, Korea, 23-26 October 2018
Contact: http://isap2018.org/

November 2018

APMC
Asia-Pacific Microwave Conference 2018
Kyoto, Japan, 6-9 November 2018
Contact: http://www.apmc2018.org/

LAPC 2018
Loughborough Antennas and Propagation Conference
Loughborough, United Kingdom, 12-13 November 2018
Contact: Poppy Seamarks, Tel: +44 (0)1438 767 304, Fax: +44 (0)1438 765 659, Email: lapc@theiet.org
https://events.theiet.org/lapc/

January 2019

USNC-URSI NRSM 2019
USNC-URSI National Radio Science Meeting
Boulder, CO, USA, 9-12 January 2019
Contact: Dr. Sembiam R. Rengarajan, Department of ECE, California State University, Northridge, CA 91330-8346, USA, Fax: 818-677-7062, E-mail: srengarajan@csun.edu; Logistics: Christina Patarino, E-mail: christina.patarino@colorado.edu, Fax: 303-492-5959, https://nrsmboulder.org/

March 2019

C&RS "Smarter World"
18th Research Colloquium on Radio Science and Communications for a Smarter World
Dublin, Ireland, 8-9 March 2019
Contact: Dr. C. Brennan (Organising Cttee Chair)
http://www.ursi2016.org/content/meetings/mc/Ireland-2017-CRS Smarter World CFP.pdf

AP-RASC 2019
2019 URSI Asia-Pacific Radio Science Conference
New Delhi, India, 9-15 March 2019
Contact: Prof. Amitava Sen Gupta, E-mail: sengupto53@yahoo.com, http://aprasc2019.com

May 2019

EMTS 2019
2019 URSI Commission B International Symposium on Electromagnetic Theory
San Diego, CA, USA, 27-31 May 2019
Contact: Prof. Sembiam R. Rengarajan, California State University, Northridge, CA, USA, Fax +1 818 677 7062, E-mail: srengarajan@csun.edu, http://www.emts2019.org

November 2019

COSPAR 2019
4th Symposium of the Committee on Space Research (COSPAR): Small Satellites for Sustainable Science and Development
Herzliya, Israel, 4-8 November 2019
Contact : COSPAR Secretariat, 2 place Maurice Quentin, 75039 Paris Cedex 01, France, Tel: +33 1 44 76 75 10, Fax: +33 1 44 76 74 37, E-mail: cospar@cosparhq.cnes.fr
http://www.cospar2019.org

August 2020

COSPAR 2020
43rd Scientific Assembly of the Committee on Space Research (COSPAR) and Associated Events
Sydney, Australia, 15-23 August 2020
Contact : COSPAR Secretariat, 2 place Maurice Quentin, 75039 Paris Cedex 01, France, Tel: +33 1 44 76 75 10, Fax: +33 1 44 76 74 37, E-mail: cospar@cosparhq.cnes.fr
http://www.cospar2020.org

URSI GASS 2020
Rome, Italy, 29 August - 5 September 2020
Contact: URSI Secretariat, c/o INTEC, Tech Lane Ghent Science Park - Campus A, Technologiepark-Zwijnaarde 15, B-9052 Gent, Belgium, E-mail gass@ursi.org

May 2021

AT-RASC 2021
Third URSI Atlantic Radio Science Conference
Gran Canaria, Spain, 23-28 May 2021
Contact: Prof. Peter Van Daele, URSI Secretariat, Ghent University – INTEC, Technologiepark-Zwijnaarde 15, B-9052 Gent, Belgium, Fax: +32 9-264 4288, E-mail: peter.vandaele@ugent.be, http://www.at-rasc.com

A detailed list of meetings is available on the URSI website at http://www.ursi.org/events.php

URSI cannot be held responsible for any errors contained in this list of meetings

ISAPE 2018

The 12th International Symposium on Antennas, Propagation and EM Theory

December 3 - 6, 2018, Hangzhou, China

http://www.rpsoc.cn/isape2018/

ISAPE, a serial symposium on antennas, propagation, and EM theory, always offers an active forum for exchanging creative ideas and experiences on the latest developments and designs in the areas of antennas, propagation, and electromagnetic theory for professors, researchers, engineers, and excellent students all over the world. The 12th International Symposium on Antennas, Propagation and EM Theory, ISAPE 2018, will be held in Hangzhou, China. All prospective papers in the areas of antennas, propagation, electromagnetic theory, computational electromagnetics, and EMC are welcome. All accepted papers will be indexed by the INSPEC database and EI Compendex. **Paper submission deadline: October 10, 2018**

SUGGESTED TOPICS

A. Antennas & Related Topics
A1. Microstrip & Printed Antennas
A2. Active & Integrated Antennas
A3. Array Antennas, Phased Arrays and Feeding Circuits
A4. Small Antennas
A5. Adaptive & Smart Antennas
A6. Multi-Band/Wideband Antennas
A7. Wire & Slot Antennas
A8. Aperture Antennas & Feeds
A9. Millimeter Wave & Sub-Millimeter Wave Antennas
A10. Optical Technology in Antennas
A11. Antennas in Mobile Communication
A12. Antenna Measurements
A13. FSS, Polarizers & Radomes
A14. Reconfigurable Antennas & Arrays
A15. Reflector/Lens Antennas & Feeds
A16. Others

B. Propagation & Related Topics
B1. Mobile & Indoor Propagations
B2. Mobile Channel Characterization & Modeling
B3. Millimeter & Optical Wave Propagation
B4. Earth-Space & Terrestrial Propagation
B5. Radio Meteorology
B6. Remote Sensing
B7. SAR Polarimetry & Interferometry
B8. Tunnel Propagation
B9. Propagation in Ionized and Non-Ionized Media
B10. Radio Astronomy
B11. Ionospheric Modification
B12. Tropospheric, Stratospheric and Ionospheric Sounding
B13. Incoherent Scatter Radar & Observations
B14. Others

C. EM Theory & Related Topics
C1. Bioelectromagetics
C2. EM Fields in Complex Media
C3. Geo-Electromagnetics
C4. Theoretical Electromagnetics & Analytical Methods
C5. Transient EM fields
C6. High-Frequency Techniques
C7. Nonlinear electromagnetics
C8. Random Media & Rough Surfaces
C9. Waveguiding Structures
C10. Time-Domain Techniques
C11. Inverse Problems & Imaging
C12. Scattering, Diffraction, & RCS
C13. Metamaterials & Electromagnetic Bandgap Structures
C14. Measurement Techniques
C15. Nano-Electromagnetics
C16. Seismo-Electromagnetics
C17. Others

D. Computational Electromagnetics
D1. Integral Equation Methods
D2. Differential Equation Methods
D3. Hybrid Techniques
D4. Optimization Techniques for CEM
D5. Asymptotic & High-Frequency Techniques
D6. Low-Frequency Electromagnetics
D7. Computational Bioelectromagnetics
D8. Pre- & Post-Processing
D9. Nondestructive Techniques
D10. NEC Modeling & Analysis
D11. FEKO Modeling & Analysis
D12. CST Modeling & Analysis
D13. MEFiSTo Modeling & Analysis
D14. Object-Oriented Computational Electromagnetics
D15. Transmission-Line Theory
D16. Others

E. Electromagnetic Compatibility & Related Topics
E1. Probe & Sensor
E2. Absorbing Materials
E3. Test Chambers
E4. EMC Test & Measurement
E5. Coupling & Crosstalk
E6. EMC Standards
E7. EM Environment
E8. Automotive EMC
E9. EM Bioeffects
E10. EMC in Communications
E11. EMC in Power Engineering
E12. Lightning, ESD & EMP
E13. EMC in Computer & PCBs
E14. Shielding, Filtering & Grounding
E15. EMC in Microelectronics
E16. Immunity & Susceptibility
E17. Spectrum Management
E18. EMI Prediction Analysis & Reduction Technique
E19. EMC Education
E20. Others

F. Others
F1. High-Power Microwave Applications
F2. UWB & Impulse Applications
F3. Ubiquitous Network Systems
F4. Satellite Communication Systems
F5. Radio Technologies for Intelligent Transport Systems
F6. Subsurface Sensing
F7. MEMS-NEMS & MMIC
F8. Passive & Active Circuits
F9. Power Amplifiers, Linearization, & Active Components
F10. Millimeter Wave & Sub-Millimeter Wave Components, Circuits & Systems
F11. Signal Processing for Communications
F12. Advanced Process, Packaging & Integration Technologies
F13. 3D RF Technology
F14. Electromagnetic Materials
F15. Electromagnetic Environment Effects (E3)
F16. Earthquake Precursors & Monitoring
F17. THz Technology

Sponsor: Chinese Institute of Electronics (CIE). **Cosponsors:** CIE Radio Propagation Society, CIE Antenna Society
Local Organizer: Hangzhou Dianzi University. **Working Language:** English.
Paper Submission: See the conference Web site:

http://www.rpsoc.cn/isape2018/

Information for Authors

Content

The *Radio Science Bulletin* is published four times per year by the Radio Science Press on behalf of URSI, the International Union of Radio Science. The content of the *Bulletin* falls into three categories: peer-reviewed scientific papers, correspondence items (short technical notes, letters to the editor, reports on meetings, and reviews), and general and administrative information issued by the URSI Secretariat. Scientific papers may be invited (such as papers in the *Reviews of Radio Science* series, from the Commissions of URSI) or contributed. Papers may include original contributions, but should preferably also be of a sufficiently tutorial or review nature to be of interest to a wide range of radio scientists. The *Radio Science Bulletin* is indexed and abstracted by INSPEC.

Scientific papers are subjected to peer review. The content should be original and should not duplicate information or material that has been previously published (if use is made of previously published material, this must be identified to the Editor at the time of submission). Submission of a manuscript constitutes an implicit statement by the author(s) that it has not been submitted, accepted for publication, published, or copyrighted elsewhere, unless stated differently by the author(s) at time of submission. Accepted material will not be returned unless requested by the author(s) at time of submission.

Submissions

Material submitted for publication in the scientific section of the *Bulletin* should be addressed to the Editor, whereas administrative material is handled directly with the Secretariat. Submission in electronic format according to the instructions below is preferred. There are typically no page charges for contributions following the guidelines. No free reprints are provided.

Style and Format

There are no set limits on the length of papers, but they typically range from three to 15 published pages including figures. The official languages of URSI are French and English: contributions in either language are acceptable. No specific style for the manuscript is required as the final layout of the material is done by the URSI Secretariat. Manuscripts should generally be prepared in one column for printing on one side of the paper, with as little use of automatic formatting features of word processors as possible. A complete style guide for the *Reviews of Radio Science* can be downloaded from http://www.ips.gov.au/IPSHosted/NCRS/reviews/. The style instructions in this can be followed for all other *Bulletin* contributions, as well. The name, affiliation, address, telephone and fax numbers, and e-mail address for all authors must be included with

All papers accepted for publication are subject to editing to provide uniformity of style and clarity of language. The publication schedule does not usually permit providing galleys to the author.

Figure captions should be on a separate page in proper style; see the above guide or any issue for examples. All lettering on figures must be of sufficient size to be at least 9 pt in size after reduction to column width. Each illustration should be identified on the back or at the bottom of the sheet with the figure number and name of author(s). If possible, the figures should also be provided in electronic format. TIF is preferred, although other formats are possible as well: please contact the Editor. Electronic versions of figures *must* be of sufficient resolution to permit good quality in print. As a rough guideline, when sized to column width, line art should have a minimum resolution of 300 dpi; color photographs should have a minimum resolution of 150 dpi with a color depth of 24 bits. 72 dpi images intended for the Web are generally *not* acceptable. Contact the Editor for further information.

Electronic Submission

A version of Microsoft *Word* is the preferred format for submissions. Submissions in versions of T_EX can be accepted in some circumstances: please contact the Editor before submitting. *A paper copy of all electronic submissions must be mailed to the Editor, including originals of all figures.* Please do *not* include figures in the same file as the text of a contribution. Electronic files can be send to the Editor in three ways: (1) By sending a floppy diskette or CD-R; (2) By attachment to an e-mail message to the Editor (the maximum size for attachments *after* MIME encoding is about 7 MB); (3) By e-mailing the Editor instructions for downloading the material from an ftp site.

Review Process

The review process usually requires about three months. Authors may be asked to modify the manuscript if it is not accepted in its original form. The elapsed time between receipt of a manuscript and publication is usually less than twelve months.

Copyright

Submission of a contribution to the *Radio Science Bulletin* will be interpreted as assignment and release of copyright and any and all other rights to the Radio Science Press, acting as agent and trustee for URSI. Submission for publication implicitly indicates the author(s) agreement with such assignment, and certification that publication will not violate any other copyrights or other rights associated with the submitted material.

Become An Individual Member of URSI

The URSI Board of Officers is pleased to announce the establishment of Individual Fellowship (FURSI), Individual Membership (MURSI), and Individual Associate Membership (AMURSI). By joining URSI, Individual Associate Members, Individual Members, and Fellows secure recognition with their peers, are better connected to URSI Headquarters, and are better connected to their National Committees. Each can then better provide support to the other. Other benefits include discounted registration fees at URSI conferences (beginning with the 2018 URSI AT RASC) and at some conferences cosponsored by URSI (beginning with some conferences run by IEEE AP-S), a certificate of membership, and e-mail notification of the availability of the electronic edition of the URSI *Radio Science Bulletin*.

Fellowship is by invitation only. Membership and Associate Membership can be applied for through the online forms available at **www.ursi.org/membership.php**, or at **www.ursi.org**